Comparative Study of Flow Analysis Algorithms Using 1.23 AGeV Au+Au Data Measured with HADES

Master Thesis

Mathilde Himmelreich

Goethe-Universität Frankfurt
Institut für Kernphysik Frankfurt

September 24, 2017

Reviewer: Prof. Dr. Christoph Blume
Second Reviewer: Dr. Heidi Schuldes

Abstract

Anisotropic collective flow of protons resulting from non-central heavy ion collisions is a unique hadronic observable providing information about the early stage of the nuclear collision. The analysis of collective flow in the energy regime between $1-2\,\mathrm{AGeV}$ enables the study of the phase diagram of hadronic matter at a high baryochemical potential μ_b, as well as the analysis of the equation of state at densities up to the threefold of the ground state density ρ_0.

The algorithms of the standard event plane method and the scalar product method are used to analyse directed and elliptic flow of protons in a centrality range of 0–40 % most central events.

Prior to the analysis of experimental data, the respective influence of the reconstruction procedure on the algorithms is examined using Monte Carlo simulations based on the Ultra relativistic Quantum Molecular Dynamics (UrQMD) model.

Subsequently, experimental data measured in April 2012 with the High Acceptance DiElectron Spectrometer (HADES) is analysed using both methods. About $7.3\cdot10^9$ Au+Au events at a kinetic beam energy of 1.23 AGeV, equivalent to a centre of mass energy of $\sqrt{s_{NN}} = 2.42\,\mathrm{GeV}$ were recorded. A multi-differential analysis is feasible as the HADES detector provides a good transverse momentum and rapidity coverage.

Both algorithms result in identical values for directed and elliptic flow across all centrality classes within the observable phase space of protons. The calculated integrated value of v_2 at mid rapidity is in good agreement with world data.

Zusammenfassung

Anisotroper und kollektiver Protonenfluss, erzeugt in nicht-zentralen Schwerionenkollisionen, ist eine einzigartige hadronische Observable, die Informationen über die Frühphase von Kernkollisionen zur Verfügung stellt. Die Analyse von kollektivem Fluss in dem Energiebereich von $1-2\,\mathrm{AGeV}$ ermöglicht die Studie des Phasendiagramms hadronischer Materie bei hohem baryochemischen Potential, als auch die Analyse der Zustandsgleichung von Materie bei Kernmateriedichten von dem dreifachen der Grundzustandsdichte ρ_0.

Verwendet werden die Algorithmen der gängigen Ereignisebenen- und der Skalarproduktmethode zur Analyse von gerichtetem und elliptischem Protonenfluss in einem Bereich der $0-40\,\%$ zentralsten Ereignissen. Vor der Analyse von experimentellen Daten wird der jeweilige Einfluss der Rekonstruktionsverfahren auf die Algorithmen unter Verwendung einer Monte Carlo Simulation, die auf dem „Ultra Relativistic Quantum Molecular Dynamics“ (UrQMD) Modell basiert, untersucht.

Anschließend erfolgt die Analyse von experimentellen Daten, gemessen im April 2012 mit dem High Acceptance DiElectron Spectrometer (HADES), ebenfalls mit beiden Methoden. Aufgenommen wurden mehr als $7.3\cdot10^9$ Gold+Gold Ereignisse bei einer kinetischen Strahlenergie von 1.23 AGeV, die einer Kollisionsenergie im Schwerpunktsystem von $\sqrt{s_{NN}} = 2.42\,\mathrm{GeV}$ entspricht. Da der HADES-Detektor sehr weite Bereiche des transversalen Impulses und der Rapidität abdeckt, ist eine multidifferenzielle Analyse möglich.

Beide Algorithmen resultieren in identischen Werten für gerichteten und elliptischen Fluss über alle Zentralitätsbereiche hinweg und über den gesamten beobachtbaren Phasenraum der Protonen. Der berechnete integrierte Wert für v_2 bei Schwerpunktsrapidität stimmt mit den Ergebnissen anderer Experimente gut überein.

Contents

1. Introduction

1.1. Motivation

According to the widely acknowledged Λ-CDM[1] model, the beginning of the universe is assumed to be point-like and a subsequent expansion led to the present universe [1, 2, 3].

Currently, this cosmological model is favoured by the majority of astronomers as it is in accordance with four significant observables: the *density fluctuations* on different length scales, which are assumed to be based on quantum fluctuations at a very early stage of the universe [4], the almost isotropic *Cosmic Microwave Background* (CMB) originating from the first recombination of hydrogen [5], the frequency distribution of the elements in the universe due to the *Big Bang Nucleosynthesis* (BBN) [6] and the expansion of the universe, observable by the redshift z [2] [7]. The accelerated expansion of the universe is part of current research activities [8, 9] and led to the introduction of *dark energy*.

The *hot big bang theory* [3], based on the Λ-CDM model combining both general relativity and standard thermodynamics, describes the cosmological evolution including stages of thermal equilibrium, transisition phases and decoupling points, see figure 1.1.

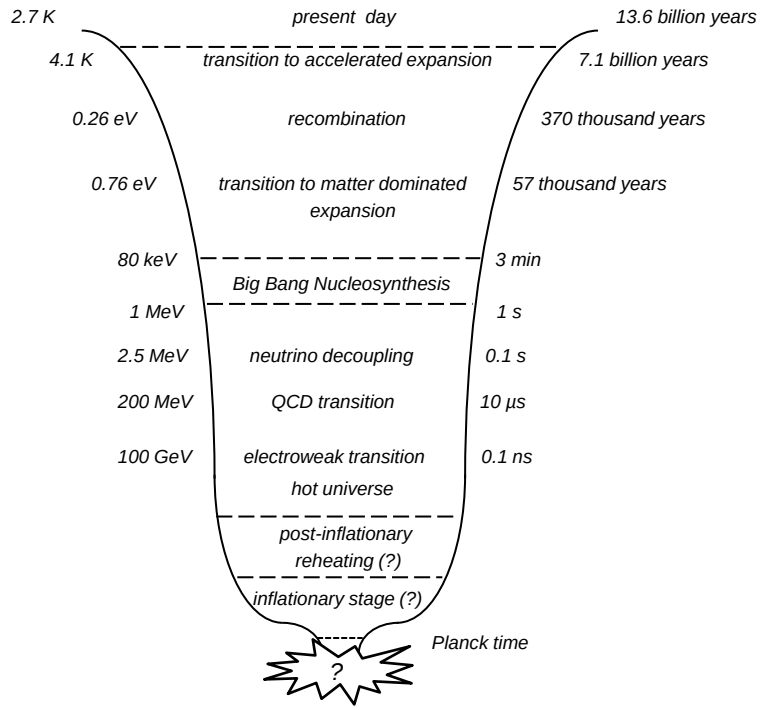

Figure 1.1: Evolution of the universe beyond Planck time ($t_{Pl} = \sqrt{G} = 5.39 \times 10^{-44}\,\mathrm{s}$ in the system of natural units) [3]. The expansion results in a decreasing temperature, another reference besides time, with $1\,\mathrm{K} = 1 \cdot 10^{-4}\,\mathrm{eV}$.

The current state of the universe was influenced by these transition stages and decoupling points, determined by particle and nuclear properties and elementary forces: for instance, the temperature of transition from quark-gluon matter to hadronic matter[3] is determined by the

[1] Λ: cosmological constant, the value of the energy density of the vacuum of space. CDM: Cold Dark Matter.

[2] A photon emitted at some moment of time in the past with a physical wavelength at the moment of emission of λ_e (H_α for instance), is observed today as photon of a longer physical wavelength λ_0. $z = \lambda_e/\lambda_0 - 1$

[3] A smooth cross-over from quark-gluon matter to hadronic matter.

energy scale of strong interactions and is about 200 MeV. *Chiral symmetry breaking* is supposed to occur at almost the same time, meaning that a small excess of matter (one uncompensated quark per 10 billion of quark-antiquark pairs) was generated due to baryon number violating processes in the course of the cosmological evolution [3].

Also the decoupling point of neutrinos from thermal equilibrium with protons, neutrons and electrons is of interest, as the neutrino number density in the early universe is an important parameter of the BBN theory. Furthermore, relic neutrinos affect the CMB angular power spectrum and cosmological perturbations, as such as density fluctuations [10, 11]. Hence, the examination of elementary particle properties in high-energy experiments can resolve problems in cosmology and in particle physics, like the matter-antimatter asymmetry as well as the nature of *dark energy* and *dark matter* or the nature of the *Equation of State* (EoS), which have not found their compelling solutions yet [3, 12].

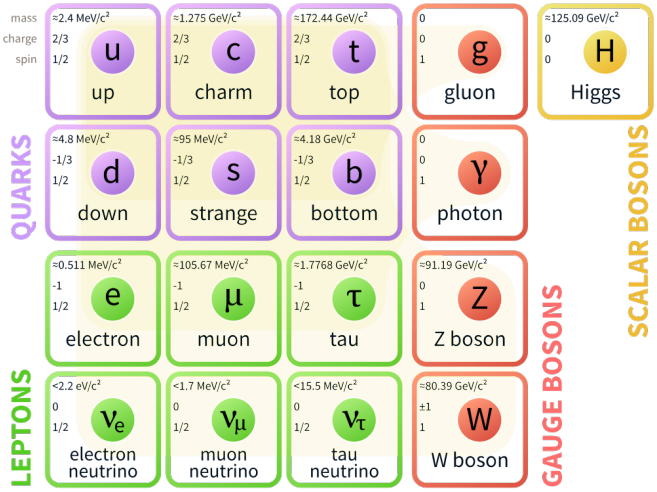

Figure 1.2: The Standard Model of particle physics [13].

The *standard model of particle physics* (SM), see figure 1.2, comprises two particle species: fermions of spin $S = \frac{1}{2}$ and bosons of integer spin.

There are three generations of fermions, separated into two groups: quarks q (violet boxes) and leptons l (green boxes) with the corresponding antiparticles antiquarks $\bar{q}$ and antileptons $\bar{l}$. The quarks, carrying an electric charge of multiples of a third, are building all known hadrons: mesons ($q\bar{q}$), baryons (qqq) and antibaryons ($\bar{q}\bar{q}\bar{q}$). Hence, all observable hadrons are carrying integer electrical charge. Each charged lepton (e^{-1}, μ^{-1}, τ^{-1}) has a corresponding electrically neutral neutrino (ν_e, ν_τ, ν_τ).

There are four known fundamental forces: electromagnetic, weak, strong and gravitational[1] force; their exchange particles are the gauge bosons (red boxes). The unified electroweak force, developed in the 1960s by Sheldon Glashow, Steven Weinberg and Abdus Salam, who were awarded with the Nobel Prize in 1979, describes the electromagnetic and the weak force as different aspects of the same fundamental force. The electromagnetic force, affecting all quarks and charged leptons, has an infinite range, as the exchange particle, the photon (γ), is massless and is itself not subject to the transmitted force. The potential due to the electromagnetic force diminishes with increasing distance between the two charged particles. The weak force, acting on all elementary particles, has a range of less than $\sim 10^{-15}$ m, since the transmitting Z^0 and

[1]Not described by the SM. The postulated exchange boson of $S = 2$, the *graviton*, has not been verfied yet.

$W^{\pm}$ gauge bosons are not massless: $m_{W,Z} > 80\,\text{GeV}$. The strong force is mediated by gluons (g) and couples to all colour charged particles, including all quarks and the gluons themselves. The three types of colours (red, green and blue) are bound to colour neutral hadrons as such as baryons (rgb or $\bar{r}\bar{g}\bar{b}$) and mesons ($r\bar{r}$, $g\bar{g}$ or $b\bar{b}$)[1]. Since gluons are interacting among themselves the strong force is limited to a range in the order of $\sim 10^{-15}\,\text{m}$, the radius of a proton. In attempting to separate two quarks ($q_1\bar{q}_1$), a high amount of energy has to be supplied to the system. At some point, the amount of energy is high enough to generate two other quarks, building two new pairs ($q_1\bar{q}_2$ and $q_2\bar{q}_1$). Hence, colour charged particles can not be isolated and are always confined in colour neutral hadrons. This is called *confinement*. The term *asymptotic freedom* means that quarks resemble free particles and interact only weakly within the volume of hadrons.

Mass of all particles is generated by the Higgs field, postulated by Peter Higgs in 1964 [15], and the quantum mechanic excitation of the field results in the massive Higgs boson (yellow box) recently detected at CERN[2] [16]. Peter Higgs and François Englert were awarded with the Nobel Prize in 2013 for the discovery of the Higgs mechanism.

The fourth fundamental force, gravitation, dominant force at large scales[3] [3, 18], is not part of the Standard Model and a sufficient unification theory has not been found yet.

Nuclear matter has different phases, like water has the three aggregate conditions liquid, solid and gaseous. The corresponding phase diagram is shown in figure 1.3, with the absolute temperature T on the vertical axis and the baryochemical potential μ_B on the horizontal axis.

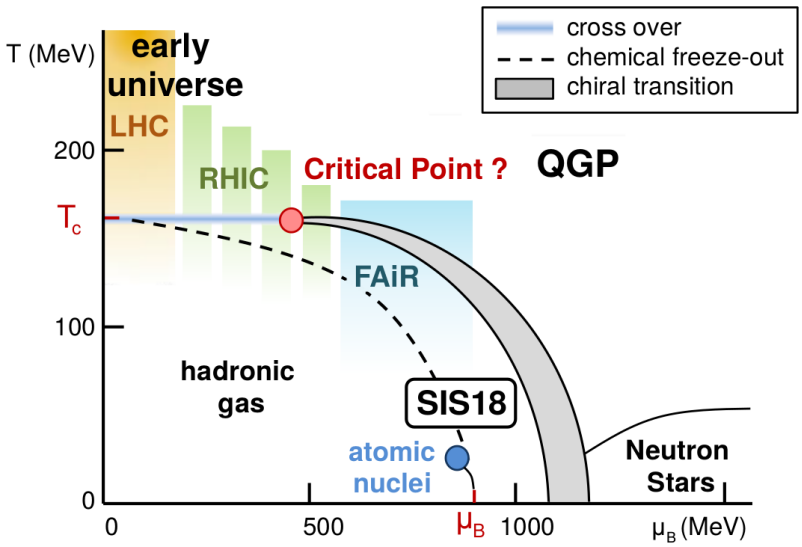

Figure 1.3: Phase diagram of hadronic matter with selected high energy accelerator facilities: LHC[4], the Beam Energy Scan (BES) at RHIC[5] and SIS18. Experimental data of this work (Au+Au at 1.23 AGeV) are generated using the SIS18 (*SchwerIonenSynchrotron* with a maximum magnetic rigidity of 18 Tm), located at the *GSI Helmholtzzentrum für Schwerionenforschung GmbH*.

[1] The possibly discovered pentaquark P_c^+ type in 2015 at CERN is assumed to be colour neutral as well [14].
[2] Conseil Européen pour la Recherche Nucléaire
[3] Galaxy clusters like the *Laniakea Supercluster*, hosting the milky way, are bound by gravitation [17].
[4] Relativistic Heavy-Ion Collider, operating over a range of $\sqrt{s} = 7.7 - 200\,\text{GeV}$
[5] Large Hadron Collider at CERN

The baryochemic potential μ_B corresponds to the required amount of energy to add a baryon to a baryonic system in thermal equilibrium.

Atomic nuclei have a finite net baryon density, meaning a low temperature and an excess of baryons relating to anti-baryons at a ground state density of $\rho_0 = 0.16\,\mathrm{fm}^{-3}$. If the temperature is increased at a given low baryochemic potential, the matter changes in a gas of still confined hadrons before it undergoes a smooth cross-over to the deconfined *Quark Gluon Plasma* (QGP). This state of high temperature QGP at zero net baryon density is assumed to have been existed in the *early universe*. If the baryochemical potential is increased at a low temperature, nuclear matter is assumed to undergo two phase transitions: a phase transition from hadronic gas to QGP, expected to be of first order, and a chiral phase transistion. According to current knowledge it is not certain whether both transistions exist and occur simultaneously at all hadron densitities.

Several experiments at different high-energy accelerator facilities, ALICE[1], CMS[2] and ATLAS[3] at CERN LHC, a number of experiments at CERN SPS[4], beam energy scans of STAR[5] and PHENIX[6] at RHIC and HADES[7] at SIS18 probed the chemical freeze-out border using heavy-ion collisions to create extreme states of matter [19, 20]. The assumption of a first order deconfinement transistion is based on theoretical calculations, perturbative Quantum Chromo Dynamics (QCD). Beyond this transistion line compact and dense objects as such as *neutron stars* are located at low temperatures. If there is a phase transition of first order besides the verified smooth cross-over region, a *critical point* is assumed to exist, separating these transistions.

Besides the previously mentioned high-energy experiments, additional projects are in developement or are already under construction (BES II at RHIC, NICA[8], J-PARC[9] and Compressed Baryonic Matter (CBM) at FAIR[10]) to examine the phase diagram of nuclear matter, especially the area of the assumed phase transition and the expected critical point.

[1] A Large Ion Collider Experiment
[2] Compact Muon Solenoid
[3] A Toroidal LHC ApparatuS
[4] Super Proton Synchrotron
[5] Solenoidal Tracker At RHIC
[6] Pioneering High Energy Nuclear Interaction eXperiment
[7] High Acceptance DiElectron Spectrometer
[8] Nuclotron-based Ion Collider fAcility
[9] Japan Proton Accelerator Research Complex
[10] Facility for Antiproton and Ion Research

1.2. Heavy-Ion collisions

Heavy-ion collisions (HICs) are designed to study matter under extreme conditions: hot phases as assumed for the early stage of the universe or dense phases as assumed to exist in compact stellar objects as such as neutron stars. An access to the particular phases of nuclear matter is possible using different energies[1] and varying the collision system (ions).

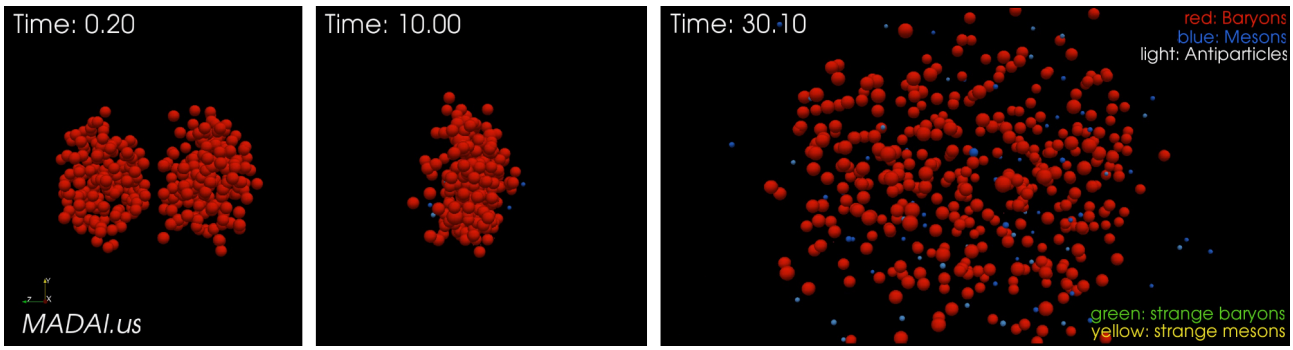

Figure 1.4: Illustration of the time evolution of a heavy-ion collision at 2 AGeV [21]. Initial state: the nucleons of the two nuclei (first picture) are shown in red. Mesons, created in the high density phase (second picture), are represented as smaller blue spheres as the radius scales with the square root of the particle mass. After about 30 fm/c inelastic and elastic scattering of the particles ends as the system expands and cools down (third picture). The simulation is based on the Ultrarelativistic Quantum Molecular Dynamics (UrQMD) model [22, 23].

Ions of heavy elements consist of many nucleons, protons and neutrons. A heavy-ion collision can be described simplified as the collisions of nucleons of two colliding nuclei, Au+Au for instance. At the first stage of a HIC, a nucleon interacts in first chance collisions with many nucleons of the other nucleus and deposits energy in the collision region. Due to this energy loss the nucleon slows down, called *nuclear stopping*. This energy is transformed into thermal and compressional energy of the system and is available for particle production. At SIS18 energies, this second high density stage has a lifetime of about 10^{-22} s and is called *fireball*, as the reaction zone is heated up to $T = 80 - 100$ GeV at a net baryon density of up to $\rho \approx 3 \cdot \rho_0$. While expanding and cooling down, the matter undergoes two transistions: first, the *chemical freeze-out* takes places, meaning inelastic scattering of the particles ends and the number of the produced particles remains constant[2]. Second, the following *kinetic freeze-out* describes the end of elastic scattering of the particles, meaning the momenta of the particles remain constant. Figure 1.4 shows the three described stages of a HIC.

The total number of interacting particles (*participants*) and the outcome of an event depends on the collision geometry. The more central the collision, the more nucleons are involved. The centrality of a collision is specified by the impact parameter b, the distance between the centres of the two colliding nuclei. A detailed description of the estimation of the centrality can be found in paragraph (3.1). Non-participating nucleons are called *spectators*.

[1] STAR's BES program at RHIC for instance

[2] Weak decays and suppressed decays due to the OZI rule may occur also later on.

1.3. Collective flow

The term *collective flow* includes *radial flow* and *anisotropic flow*. Radial flow is dominant in central HIC, as the pressure gradient of the reaction volume is radially symmetric, speeding up all particles and pushing them radially outward. The radial expansion affects the transverse spectra of outgoing particles, whereas the anisotropic expansion affects the spatial orientation of the particle momenta. Only anistropic flow will be discussed in detail, as this thesis compares analysis methods for anisotropic flow.

In short, anisotropic flow is defined as the azimuthal asymmetry in the particle distribution with respect to the *reaction plane* (RP), spanned by the the impact parameter b and the beam axis in z-direction. The most common explanation of anisotropic flow is the rescattering of the constituents [24].

The developement of flow is influenced by many physical processes in each of the previously discussed stages of the HIC, depending on the collision energy, the rapidity y and the transverse momentum p_t. Also the dimension and shape of the reaction volume, depending on the centrality of the collision and the species of the colliding nuclei, has to be taken into account. Figure 1.5 shows two heavy ions just after the collision.

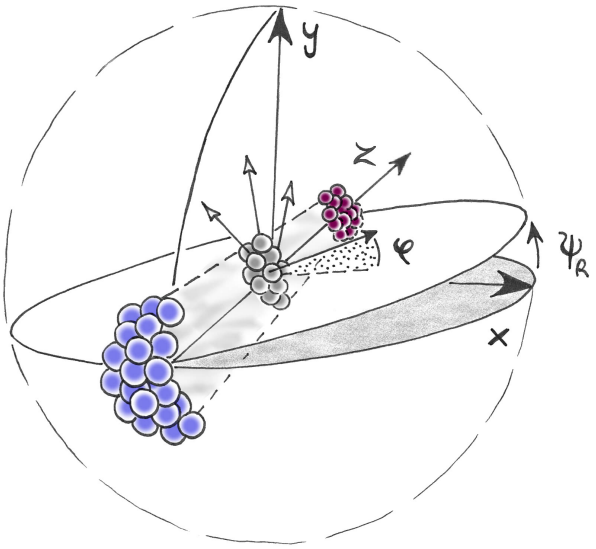

Figure 1.5: In centre-of-mass (CoM) frame of a heavy-ion-collision: the *reaction plane* is spanned by the impact parameter b and the beam axis in z-direction. The angle between the RP and the x-axis is referred to as Ψ_R. *Target spectators*, coloured in blue, and *projectile spectators*, shown in red, escape from the reaction centre within the RP and continue moving in opposite directions along the z-axis. The grey coloured *participants* are subject to anisotropic flow and the azimuthal component of their direction of movement is described by φ.

Anisotropic flow can only develop in the first fm/c (about 10^{-23} s) as the spatial assymetry rapidly decreases in time [25]. Thus, flow must be sensitive to the particle interactions during the early stages of the HIC. Therefore it provides direct information about this phase, in which at high energies the QGP is assumed to be dominant in this early stage.

The anisotropic particle distribution can be characterised by the Fourier expansion of the momentum distribution relative to the reaction plane angle Ψ_R:

$$E\frac{d^3N}{d^3\boldsymbol{p}} = \frac{1}{2\pi}\frac{d^2N}{p_t\,dp_t\,dy}\left(1+2\sum_{n=1}^{\infty}v_n\cos\left[n\left(\varphi-\Psi_R\right)\right]\right) \tag{1.1}$$

with the particle energy E, the particle momentum $\boldsymbol{p}$ and the azimuthal angle φ of the particle. The sine terms are not present in the expansion due to symmetry with respect to Ψ_R. The Fourier coefficients v_n, also referred to as *harmonic*, are functions of y and p_t and can be calculated by

$$v_n\left(p_t,y\right) = \left\langle\cos\left[n\left(\varphi-\Psi_R\right)\right]\right\rangle. \tag{1.2}$$

$\langle\ldots\rangle$ denotes an average over all particles and over all events. For central collisions the coefficients v_n are zero as the spherical reaction volumes lead to uniform particle distributions. For peripheral events the coefficients are non-zero. The first harmonic v_1 is called *directed flow*, representing an overall shift of the particle distribution. The second harmonic v_2, *elliptic flow*, describes the emission of particles from an elliptic shaped reaction volume, illustrated on the left side of figure 1.6.

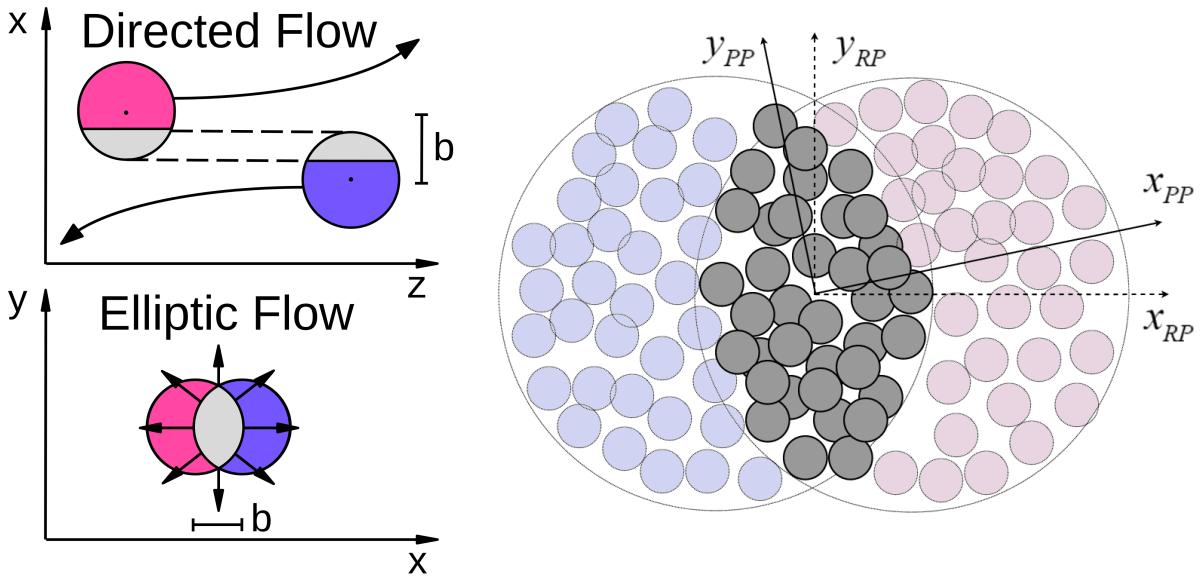

Figure 1.6: Left side: diagrams of directed (v_1) and elliptic (v_2) flow. The interacting parts of the two colliding nuclei, shown as blue and red spheres, are greyed out. Right side: definitions of the reaction plane and the participant coordinate system [26]. The overlap zone of the colliding nuclei can be shifted and tilted with respect to the reaction plane frame (x_{RP}, y_{RP}). The possible deviation of the participant plane frame (x_{PP}, y_{PP}) relative to the reaction plane frame varies from event to event.

The impact parameter b, defining the RP, can not be directly measured in a HIC. The RP can be estimated from the particle azimuthal distribution for each event; this estimation is called the event plane (EP). As the EP is very likely to differ from the RP, an uncertainty is introduced in the analysis of different size for each event.

Moreover, the effective position of the individual participating nucleons can deviate from the geometrical ellipsoid with respect to the RP frame at fixed impact parameter. The orientation

of the major axis as well as the eccentricity of the *participant zone* (see right side of figure 1.6) fluctuates around the major axis and the eccentricity of the geometric overlap region defined with respect to the RP frame (x_{RP}, y_{RP}) on an event by event basis. The eccentricity fluctuation can be described by a two-dimensional Gaussian with the same width in both directions [24]. An estimation of the size of the flow fluctuations, usually referred to as *flow fluctuations*, is feasible using MC Glauber calculations [27]. The flow values calculated relative to the PP are always higher compared to those calculated relative to the RP [28]. The difference of the calculated flow coefficients with respect to the corresponding frame ($v_{n,PP}$ and $v_{n,RP}$) can be depicted as the projection of the particle momentum vector onto each of the planes, see figure 1.7.

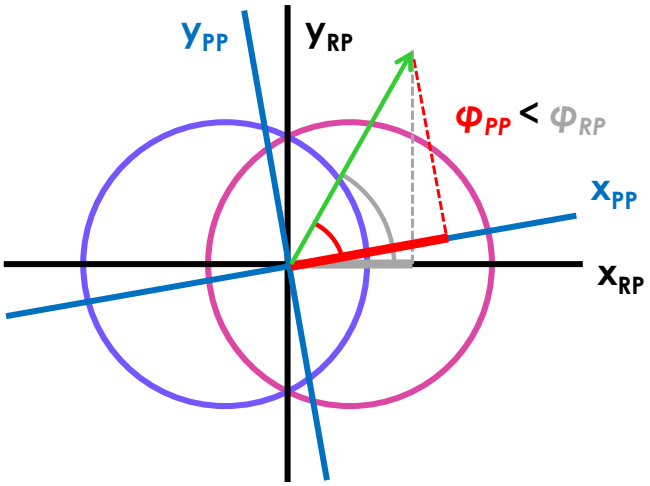

Figure 1.7: Scheme of two colliding nuclei in direction of the z-axis: the participant plane frame is inclined towards the reaction plane frame. The cosine ($v_n = \langle \cos[n\,(\varphi - \Psi)] \rangle$) can be interpreted as a projection of the particle momentum vector (green arrow) with the angle φ onto the respective plane Ψ [28]. φ is the azimuthal component of the movement direction of the particle.

In addition to flow fluctuations, another interfering contribution has to be considered: *non-flow*, a few-particle correlation. The correlation is not associated with the RP, unlike *collective flow*, a correlation including all particles of an event. The rapidity of the involved particles in non-flow is expected be very alike, as non-flow effects include the Hanbury-Brown-Twiss (HBT) effect, momentum conservation, the correlation of particles, which are decay products of the same mother particle, and also jets at high energy experiments [24].

Directed flow

Directed flow is zero at midrapidity because $\langle\cos(\varphi)\rangle$ is an odd function. The slope $\mathrm{d}v_1(y)/\mathrm{d}y$ at midrapidity is often used to quantify the strength of directed flow (at SPS energies for instance [24]). Directed flow results from the pressure inside the reaction volume and has its maximum at semi-central events, as the pressure gradient is insufficient at very peripheral collisions and central events are creating the radial flow. As the created dense matter deflects remaining incoming nuclear matter during the passing time of the colliding nuclei, the magnitude of the deflection is a probe for the compressibility of the system at early times [28].

Elliptic flow

Elliptic flow can only develop in a HIC if an anisotropic reaction volume is present and if the mean free path of the particles is of smaller size than the reaction volume (multiple scattering is present) [28]. In the absence of rescattering elliptic flow should be zero and in the low density limit it is directly proportional to the particle density in the transverse plane [29]. The initial spatial anisotropy that causes the anisotropic transverse momentum distribution of the participants can be described by the spatial eccentricity, which is defined as

$$\varepsilon_x = \frac{\langle y^2 - x^2 \rangle}{\langle y^2 + x^2 \rangle} \tag{1.3}$$

in the reaction plane coordinate system, where x is taken in the impact parameter direction. The shape of the reaction volume and the scattering mean free path are dependent on the centrality, see figure 1.8.

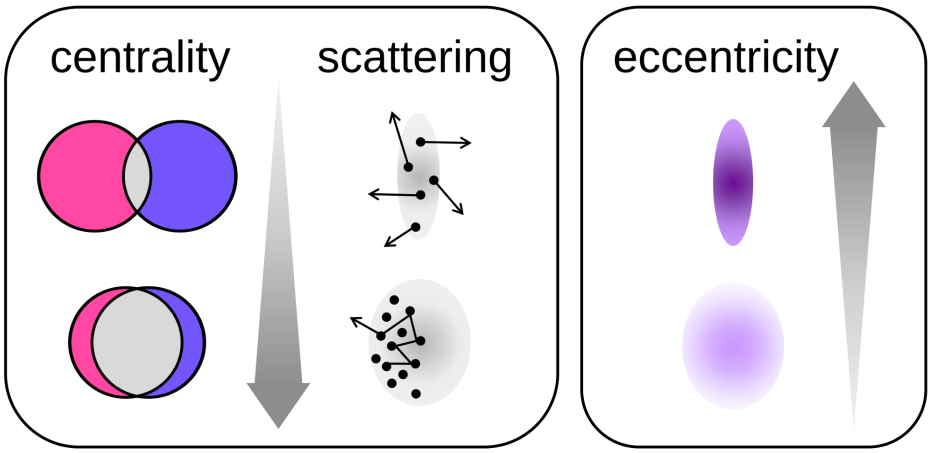

Figure 1.8: Development of scattering and eccentricity compared to increasing centrality. For most central events, $\mathcal{C} = 0\,\%$, the reaction volume is a sphere as the semi-minor and semi-major axis are of same size ($\varepsilon_x = 0$). Multiple scattering has its maximum at most central events.

The spatial eccentricity decreases, whereas the multiple scattering is growing for increasing centrality [30]. Due to these opposite effects v_2 has its maximum value at mid-central collisions.

The space-time evolution of the system can be described by a hydrodynamical model if the mean free path of the particles is significantly smaller than the size of the reaction volume. This model is determined by the initial conditions of the system, as such as the initial time, particle velocities and energy density ε, the decoupling conditions and the *Equation of State* (EoS).

The EoS describes the relation between ε and the thermodynamic variable p (pressure) of the system. Directed and elliptic flow of protons is assumed to be a measure of the EoS since it is sensitive to the initial pressure in the reaction volume [24, 31]. As the real initial conditions and the EoS of the sytem are not known, various initial conditions or free parameters as such as the coeffcient of compressibility κ are set as input to a number of different EoS in order to compare these results to experimental data [32, 33, 34].

Depending on the value of κ the EoS is called *soft* or *stiff*. The EoS is soft if the pressure change causes an energy density change of comparable magnitude. An EoS is stiff if a given change of the pressure causes a great change of the energy density. In the studies of [33] the IQMD[1] transport model[2] is used with two different values of κ, 200 MeV and 380 MeV, leading to a soft and to a stiff EoS. The results of both calculations are compared to experimental data – directed flow of single charged particles for Au+Au collisions at an energy of 90 MeV per nucleon in a centrality range ($M4$) defined by the impact parameter ($1.9\,\text{fm} < b < 6.1\,\text{fm}$), see figure 1.9. Since the blue data points are following the line representing calculations using a soft EoS, the conclusion can be drawn that results of HICs are leading to a soft EoS, supported by the findings of other experiments [35].

However, astrophysical observations are in contradiction with a soft EoS. The mass-radius relationship and maximum possible mass of neutron stars depends on the nature of the EoS. The observed $(2.01 \pm 0.4)\,M_\odot$ neutron star[3] can not be explained by a soft EoS within the present common models [37, 38, 39]. Therefore, no applicable EoS has been found yet and is still subject of recent studies.

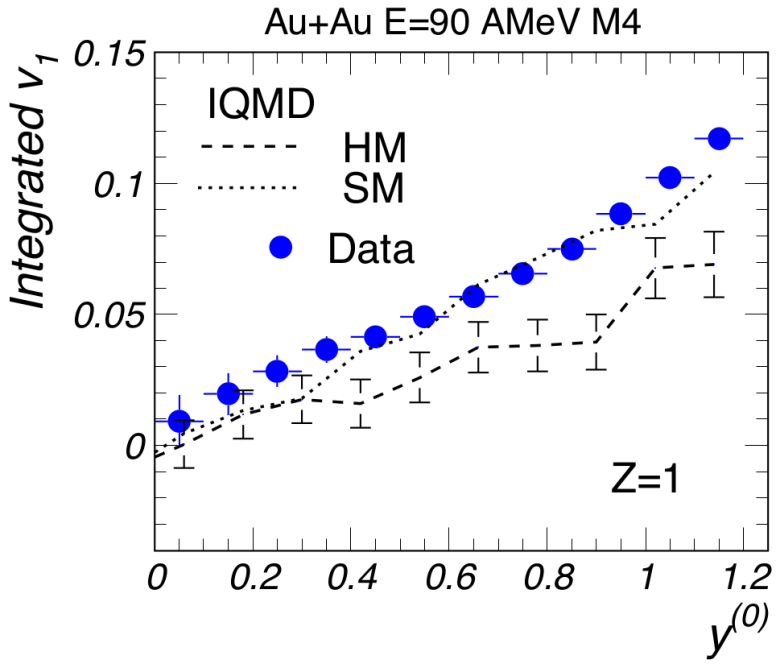

Figure 1.9: Experimental data measured at FoPi and IQMD transport model calculations using a hard EoS with $\kappa = 380$ MeV (HM[5]) and a soft EoS $\kappa = 200$ MeV (SM[6]) [33].

[1]Isospin Quantum Molecular Dynamics
[2]Hadronic systems can be described by hydrodynamical models as well as by transport models.
[3]PSR J0348+0432 [36]
[5]H-MDI; Hard-Momentum Dependent Interactions
[6]S-MDI; Soft-Momentum Dependent Interactions

In addition to its centrality dependence, v_2 is affected by the CoM energy $\sqrt{s_{NN}}$. Several experiments, FOPI[1] at GSI, E895 at the Brookhaven AGS[2], STAR, PHENIX and PHOBOS at RHIC for instance, studied v_2 as a function of kinetic beam energy E over the mass number A, see figure 1.10.

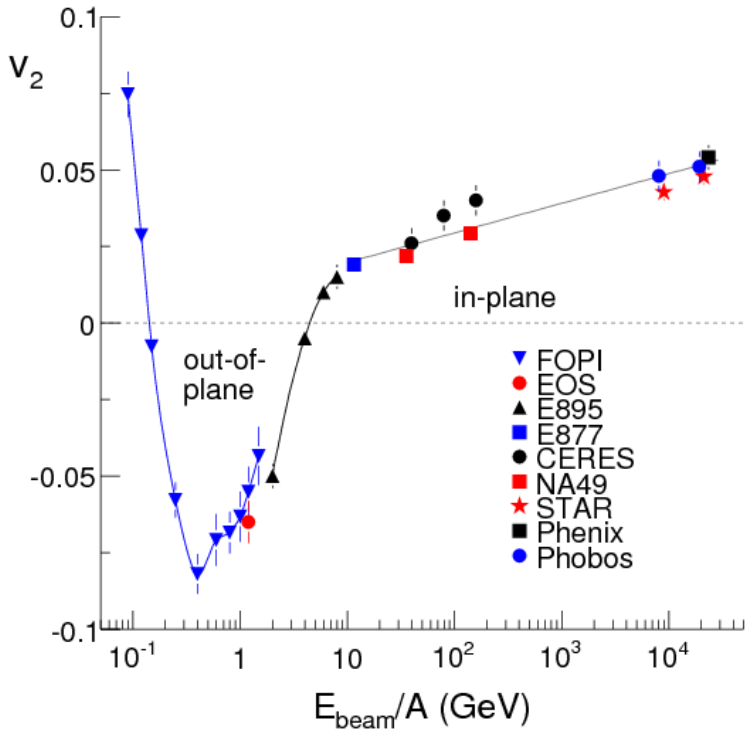

Figure 1.10: Beam energy dependence of elliptic flow measurements at midrapidity for 20–30 % most central events covering five orders of magnitude [40, 41, 42, 43, 44, 45, 46, 47, 48]. The experiments examined different particles: the RHIC and E877 data are for all species of charged hadrons, NA49 for charged pions, E865 for protons and FOPI used hadrons with $Z = 1$ for flow analysis. Picture taken from [49].

Elliptic flow changes sign two times. First, at $E_{CoM} < 100\,\text{MeV}$ the two colliding nuclei are attracted to each other since the interaction is dominated by the attractive nuclear field. The formed system is rotating and emits particles in the rotating plane [50]; positive elliptic flow occurs, referred to as *in-plane* in figure 1.10.

At higher energies the multiple scattering of the participants starts to dominate, inducing a positive pressure gradient. However, participants are prevented to escape the ellipsoidal reaction volume along the minor axis (in-plane) due to the presence of the shadowing spectators. Hence, the participants escape along the major y-axis perpendicular to the RP and flow of negative sign occurs: the so-called *squeeze-out*.

At energies above several AGeV the colliding nuclei and the spectators are contracted due to the Lorentz contraction and the passing time increases. Hence, the shielding effect of the spectators vanishes and participants are emitted in-plane as the pressure gradient is more pronounced along the minor x-axis than along the major y-axis due to the geometry.

[1] FOur PI (4π)
[2] Alternating Gradient Synchrotron

1.4. Thesis outline

This chapter has introduced the motivation of studying matter under extreme conditions in view of the evolution of the universe. Furthermore, the Standard Model of elementary particles, heavy-ion collisions and collective flow phenomena have been briefly discussed. The detector setup of HADES will be described in the second chapter as well as the principles of track and momentum reconstruction. The third chapter begins with the proton identification followed by an introduction of the two analysis methods: the *Event Plane Method* (EPM) and the *Scalar Plane Method* (SPM), which are compared by the estimation v_1 and v_2 in this thesis. Then, before experimental data is analysed using the two methods, both are verified by MC simulations. The thesis concludes with a discussion of the analysis and an outlook in the fourth chapter.

2. The HADES Detector System

2.1. Physics motivation

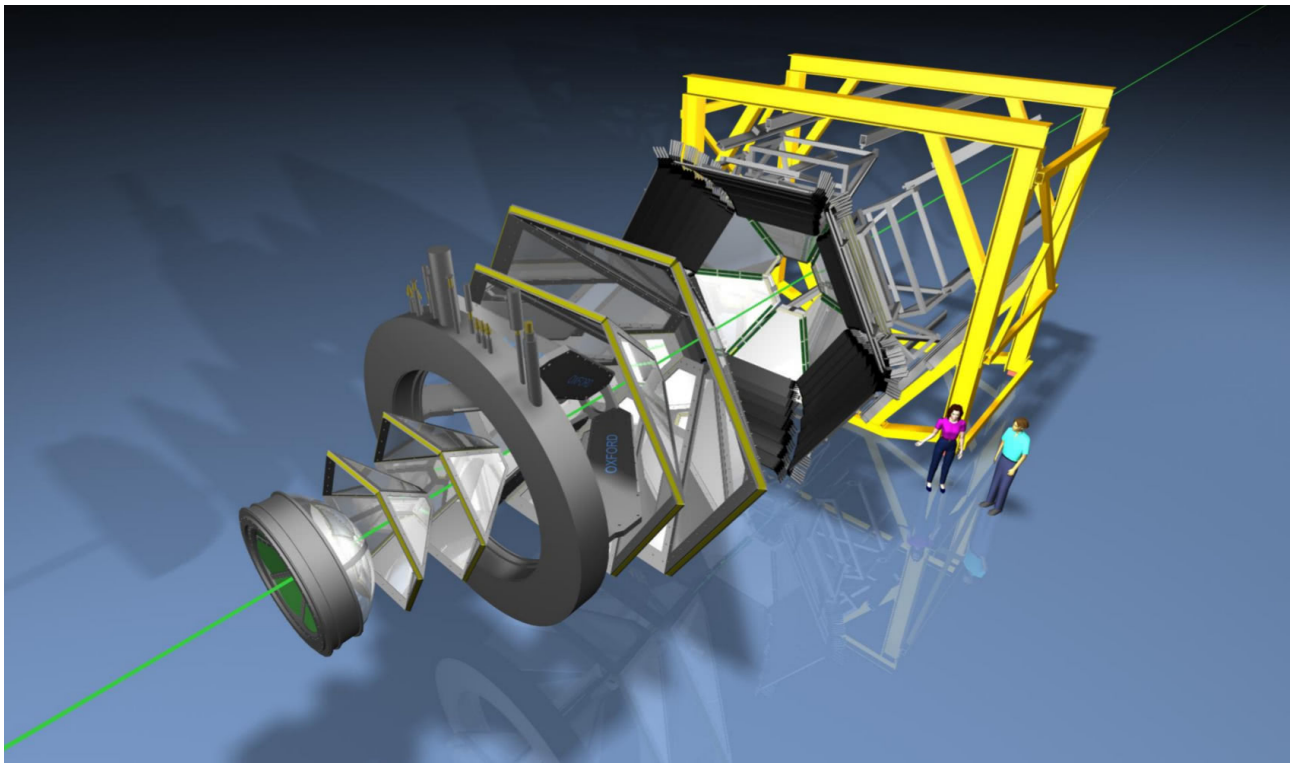

Figure 2.1: Stretched view of HADES – *High Acceptance DiElectron Spectrometer*: Six identical sectors of each detector system are arranged around the beam axis. In direction of beam line: The gaseous Ring Imaging Cherenkov detector (RICH), inner Mini-Drift Chambers (MDC I and II), IronLess Superconducting Electromagnet (ILSE), outer Mini-Drift Chambers (MDC III and IV), time-of-flight measuring devices (TOF and RPC) and the electromagnetic shower detector (PreShower). Not shown are the mono-crystalline diamond START and VETO detectors, the segmented gold target and the Forward hodoscope Wall (FW). The ion beam is visualised by a green line from the lower left to the upper right [51].

The HADES setup, see figure 2.1, in operation since October 2002 at the *GSI Helmholtzzentrum für Schwerionenforschung GmbH*, has been designed to analyse the dileptonic decay of the light vector mesons ρ, ω and ϕ produced in relativistic heavy-ion collisions [52] [53]. This electromagnetic decay channel is a probe for two reasons: The resulting e^+e^- pairs enable access to information of the conditions in the hot and dense medium created in a HIC (see section 1.2), as the lifetime of the light mesons are of comparable dimension as the duration of the compression phase. Furthermore, the e^+e^- pairs are not subject to the strong interaction, so they do not interact with nuclear matter and the gained information is not adulterated.

As the production rate of vector mesons is rare[2] and in addition the branching ratio into dielectrons is small ($\sim 10^{-3}$), high beam intensities of about 10^6 Hz are neccessary. HADES fast and highly granular detectors and an appropriate Data AcQuisition (DAQ) cope with these high beam intensities [54] [55] [56].

[2] 10^{-6}/collision in central Au-Au collisions in the 1–2 AGeV regime of the synchrotron SIS18

2.2. Spectrometer components

In this section the components of the HADES detector that were installed during the Au+Au beam time in 2012 are discussed. This involves the Ring Imaging CHerenkov detector (RICH), the START and VETO detectors, the *Magnet Spectrometer*, see section 2.2.3, comprising of the Mini-Drift Chambers (MDC) and the IronLess Superconducting Electromagnet (ILSE), the *Multiplicity Electron Trigger Array*, see section 2.2.4, consisting of the Time-Of-Flight detector (TOF), the Resistive Plate Chamber (RPC) and the PreShower detector. In a distance of 7 m behind the gold target the Forward hodoscope Wall (FW) was installed in 2010. As this work is concerned with the flow analysis of protons, the devices designed especially for leptonic identification, the RICH detector and the PreShower detector, will not be introduced; in [52] a detailed description can be found.

Numerous measurements are enabled by these individual detectors: Reconstruction of particle trajectories, multiplicity determination, specific energy loss and time-of-flight measurements, furthermore momentum and event-plane reconstruction. The HADES setup has a high polar ($18° \leq \theta \leq 85°$) and nearly full azimuthal coverage ($\phi_{acc} \approx 85\%$)[1]. In addition the FW covers a polar angle range from 0.3° to 7.3°.

2.2.1. The gold target

The gold target, see figure 2.2, is segmented into 15 disks to reduce the gamma-conversion probability[2]. Each disk with a diameter of 20 mm and a thickness of 25 μm is glued on a kapton strip with a thickness of 7 μm. A stair-like formed carbon fibre tube houses the backing strips with its attached gold disks with a distance of 4 mm from one another. Kapton foil, a classic polyimid, and carbon fibre are well suited as backing material and support structure as they are composed of carbon, nitrogen and oxygen with low atomic numbers so their contribution to gamma-conversion is small [57].

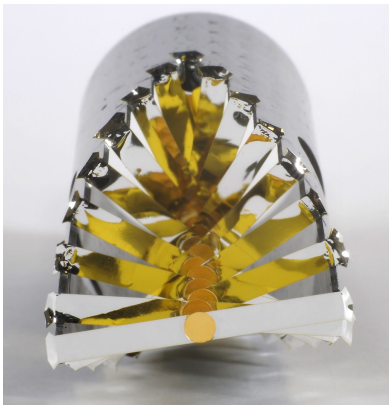

Figure 2.2: Segmented gold target with carbon fibre support structure [58].

[1] The azimuthal coverage is reduced through the support structure.
[2] $\gamma + N \rightarrow e^+e^- + N$, with $\sigma_{\gamma-\text{conv}} \propto Z^2$ and $Z_{\text{Au}} = 79$

2.2.2. The START- and VETO-detector

The mono-crystalline CVD (*Chemical Vapour Deposition*) diamond START detector positioned closely in front of the target is used as event trigger and for time-of-flight measurements in combination with the detector systems TOF, RPC and FW. Each side of the 60 μm thick detector consists of 16 193 μm wide diamond stripes and 86 μm sized gaps, one side running in horizontal direction, the other one vertically, as can be seen in figure 2.3. Due to of this fine grating the ion beam location can be determined precisely in x-y direction. The absence of chemical impurities and structural defects of the mono-crystalline diamond leads to a high charge collecting efficiency of about 95%. Also a precise time resolution of 50 ps is feasible as the drift speeds of both electrons and holes are high in the CVD diamond. Besides its radiation hardness and its resulting application as luminosity and beam-quality monitor, the lifetime can be extended by moving it through the beam line; 7 out of 9 areas were illuminated during the beam time in April 2012, as sketched in figure 2.4. To inhibit a constantly increasing leakage current appearing at high beam intensities ($\sim 10^6$ beam particles per second), which leads to a rapid discharge in the end, a 50 nm Cr layer followed by a 150 nm Au layer are deposited in a metallization procedure [59].

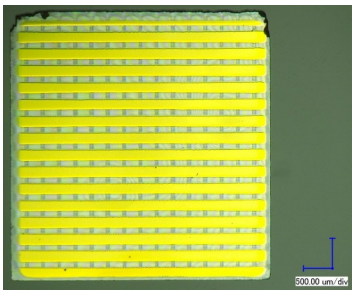

Figure 2.3: Diamond START detector, 16 stripes on each side. Strip width 193 μm, gap width 86 μm [59].

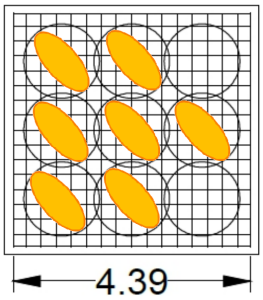

Figure 2.4: Drawing of the illumination areas on the moveable START detector in the beam-line (size in mm) [60].

Behind the target the diamond VETO detector is installed and is used in anti-coincidence to suppress pile-up or peripheral reactions and to reduce the dead time of the DAQ. The 500 μm thick diamond with an edge length of 4.7 mm is segmented into eight equal-sized, differently shaped areas, see figure 2.5, each connected to one amplifier, as can be seen in figure 2.6.

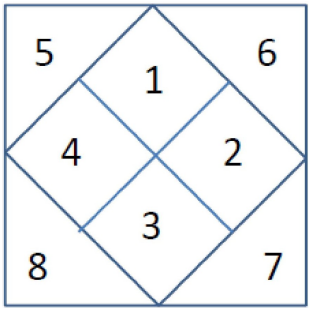

Figure 2.5: Drawing of the segmentation of the diamond VETO detector [59].

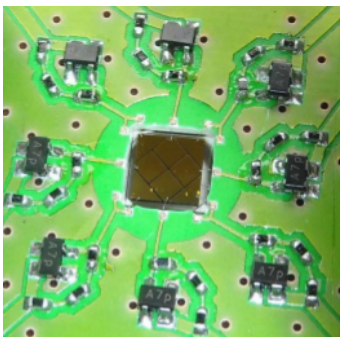

Figure 2.6: The diamond VETO detector ($4.7\times4.7\,\mathrm{mm}^2$) in the centre surrounded by eight amplifiers [61].

2.2.3. The magnetic spectrometer

The tracking system consists of four planes of the Mini-Drift Chambers (MDC I to IV) and the IronLess Superconducting Electromagnet (ILSE) and is designed for tracking and momentum measurement of charged particles.

MDCs – Mini-Drift Chambers

In total 24 mini-drift chambers with trapezoidal outer shapes are composing the four planes of the MDC. With respect to the beam direction MDC I and II are installed in front of the magnet, MDC III and IV are placed afterwards, see figure 2.7. Each plane comprises six identical chambers with increasing active surface to ensure constant granularity (MDC I: 0.35 m^2 to MDC IV: 3.2 m^2). Every sector of each plane is composed of six layers of signal wires, orientated in different stereo angles related to the bases of the trapezoid: $+40°$, $-20°$, $+0°$, $-0°$, $+20°$ and $-40°$, see figure 2.8. The full polar coverage is merely intermitted by the support structure, also housing the six coils of ILSE; the range of the azimuthal coverage is 18° to 85°. A very precise particle localisation (60-100 μm in polar and 120 -200 μm in azimuthal direction) is possible due to 1100 mini-drift cells per chamber. A mini-drift cell is a cuboid-shaped spatial volume as one can divide the gas-filled interior of a drift chamber by its parallel running wires into smaller sensitive units. Four cathode wires represent the longer edges of the elongated cuboid, its upper and lower faces are halved by field wires, in the middle of the front and the back are cathode wires and in the centre a sense wire is located.

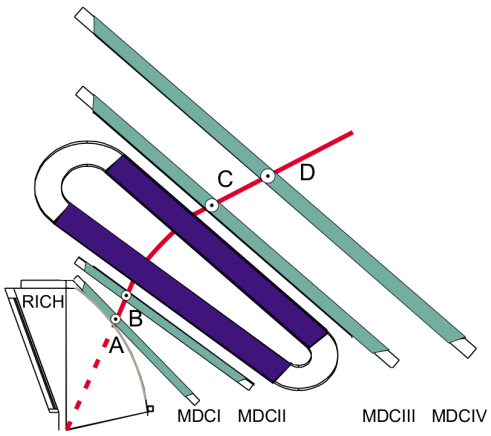

Figure 2.7: Schematic layout of the magnetic spectrometer. A fictional particle track is shown, passing each MDC (I to IV). The deflexion is caused by the magnetic field of one depicted coil of ILSE [62].

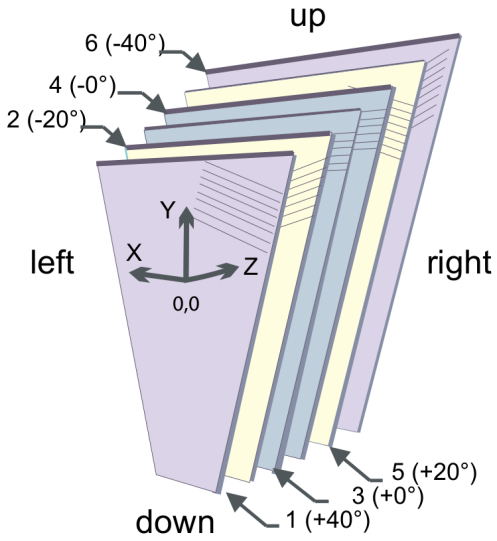

Figure 2.8: Scheme of one drift chamber. Indicated is the relative orientation of the signal wires of each layer relating to the parallel edges of the trapezoid, here labelled as *up* and *down* [62].

Charged particles traversing the detector volume are ionising the gas along their trajectory. In the presence of the electric field between the sense and the field wires the electrons and ions start to drift. Shortly before the electrons reach the sense wires they are accelerated due to the increasing field strength and ionise more gas molecules. A cascade of secondary electrons is created and produces a measurable electric signal. Besides reconstruction of a

particle trajectory the MDCs provide another measured quantity which is used for PID: the specific energy-loss.

As counting gas, two mixtures are used: the innermost MDC I is filled with Ar/CO_2 (70:30), the other chambers with Ar/isobutane (84:16). The sense wires of MDC I consists of a CuBi alloy with a slightly higher mass occupancy compared to the otherwise used aluminum wires. The admixture of quenching gas (isobutane and CO_2) to the counting gas argon is necessary to absorb ultraviolet radiation produced by the photoelectric effect inside the detector volume. This undesired reaction is as probable as the gas ionisation and the emerging high energetic photons would ionise more gas molecules. The real signal would be disturbed, at worst a complete discharge would take place. CO_2 and isobutane convert the high level radiation into rotation and inner vibration.

ILSE – IronLess Superconducting Electromagnet

The superconducting magnet ILSE consists of six identical coils, arranged around the beam axis in between MDC II and MDC III, see figure 2.9. To keep the azimuthal coverage of the MDCs as high as possible the NbTi-coils are designed to be narrow, stabilised via two rings on each side of the coil cases, see sketch 2.10.

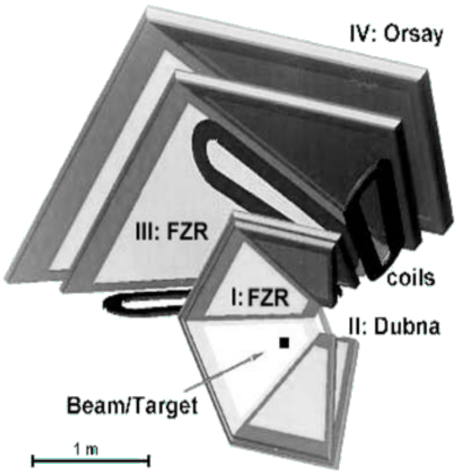

Figure 2.9: Detail of the front view sketch of the tracking system. Listed are the production locations: *Forschungs-Zentrum Rossendorf*/Germany (MDC I and III), Dubna/Russia (MDC II) and Orsay/France (MDV IV) [52].

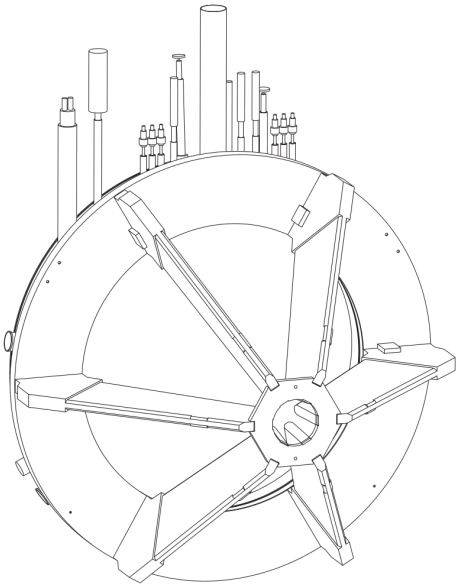

Figure 2.10: Sketch of the IronLess Superconducting Electromagnet (ILSE), back view. Six cases containing the solenoid coils are vertically mounted around the beam axis in an angular distance of 60° [56].

As the magnetic field would disrupt the trajectories of the electrons, which are produced by an ionising particle crossing a MDC, and would therefore distort their measurement, the magnetic field is limited to the gap between MDC II and MDC III. Provided with a current up to 3464 A the field strength varies between 3.7 T on the surface of the coils and decreases to 0.8 T half way between two coils. The superconducting magnet is cooled down to 4.6 K using liquid He to fall below the critical temperature of NbTi of 10 K. The magnetic field deflects

charged particles according to their momentum. As the curvature of the track depends on the momentum one can identify precisely the momentum via track reconstruction before and after passing the magnetic field. In 2.3.2 a more detailed description can be found. In conjunction with the MDCs a mass resolution of about 1% in the range of vector mesons is achievable [63] [64].

2.2.4. Multiplicity Electron Trigger Array

The *Multiplicity Electron Trigger Array* (META) consists of three detectors and is positioned behind MDC IV in direction of the beam-line, see figure 2.11. Besides its use for particle identification and time-of-flight measurement the first level trigger (LVL1, see section 2.2.6) is obtained via a multiplicity measurement by the TOF detector and the RPC, described in the following. The appendant PreShower detector for lepton identification will not be discussed as this work is focussed on research on hadrons.

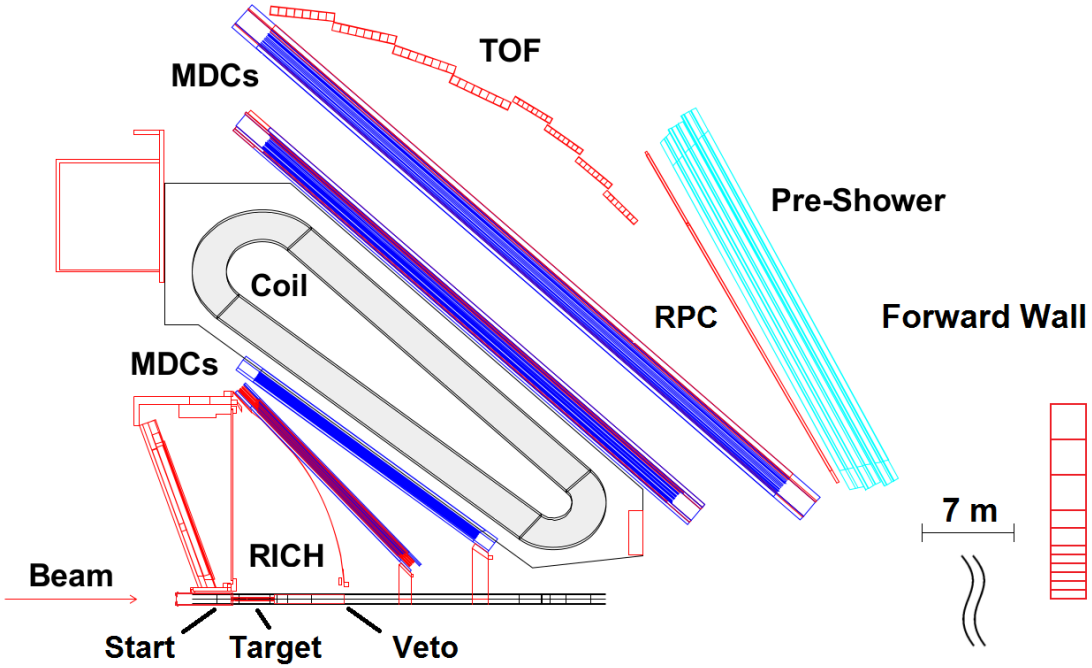

Figure 2.11: Drawing of one sector of the HADES setup. The TOF, RPC and PreShower building up the META detector are pictured behind the fourth MDC layer. A narrow polar angle range ($44° - 45°$) is covered both by TOF and RPC. The FW, installed in 2010, is located 7m downstream from the target (distance not to scale) [65].

The TOF detector

Overall 384 scintillating bars are arranged in 6 sectors and cover a polar angle range from 44° to 85°. Each sector consists of 8 rows of stripes, as can be seen in figure 2.12, and each stripe is made up of 8 scintillating bars. To reduce double hits the granularity is adjusted by increasing the cross section of the scintillators: the 4 inner stripes are composed of 8 rods of 20×20 mm, the rods of the outer ones measure 30×30 mm. Therefore the probability of two particles hitting the same bar at the same time is less then 10% [66]. The scintillating material BC-408 (BICRON®), chosen for its high light yield, small light attenuation and its short decay time offers a time resolution for time-of-flight measurements in Au-Au collisions at 1.23 AGeV

of about 190 ps in coincidence with the start signal of the START detector, see section 2.2.2 [67]. Using the start signal of the START detector and the stop signal of one of the META detectors and using the known distance between them, a time-of-flight measurement is feasible. Depending on the dimension of the scintillator a spatial resolution of $\sigma_x \in (25 - 27)$ mm is achievable.

An additional use of the TOF detector is the particle identification via the determination of the specific energy loss dE/dx [68]. When charged particles traverse the polyvinyltoluene-based plastic scintillators they deposit a fraction of their kinetic energy by exciting atoms and molecules of the material. This energy loss is specific for different species of particles and can be calculated by the Bethe-Bloch formula, see equation (3.5). Excited states de-excite under photon radiation. As both ends of the scintillator are connected to a photomultiplier (PMT), two time and two amplitude signals can be obtained. Using these information one can calculate the time-of-flight, the hit position (x-direction of the bar) and the light yield corresponding to the deposited energy.

Figure 2.12: One sector of the TOF detector before installation [69].

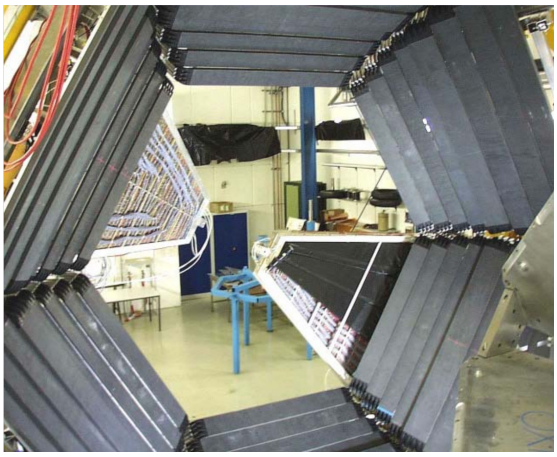

Figure 2.13: The TOF detector, view from the target region [66].

RPC – Resistive Plate Chamber

The six RPC sectors are arranged analogously to the TOF wall symmetrically around the beam axis. With a surface area of 8 m^2 they cover a polar angular range from 18° to 45°. Each sector comprises two layers of cells, subdivided into three columns. Using double layers, displaced halfway relative to each other, yields an efficiency of particle hit detection of 97%, a very accurate timing and localisation of particles crossing the detector (time resolution $\leq$ 73 ps, spatial resolution $\leq$ 8 mm). Altogether 1122 differently sized cells, 187 per sector, 31, respectively 32, per column, build up the RPC, see figure 2.14. As shown in figure 2.15 each cell consists of three stacked aluminum electrodes of 1.85 mm thickness intermediated by two isolating glass plates (2 mm) in a shielding aluminium box (2 mm). These stacked panels are fixed via plastic screws and are surrounded by an insulating kapton foil against the outer aluminium walls. The shielding box eliminates crosstalk ($\leq$ 1%) and is filled with an 90:10 admixture of Freon ($C_2H_2F_4$) and SF_6 as counting gas [70]. Incoming charged particles ionise the gas. The produced electrons are accelerated towards the anode due to the electric field caused by the high voltage (5 kV) supplied to the electrodes. An avalanche of secondary electrons is created and read out on both sides of a cell by the Front-End Electronics (FEE) [71].

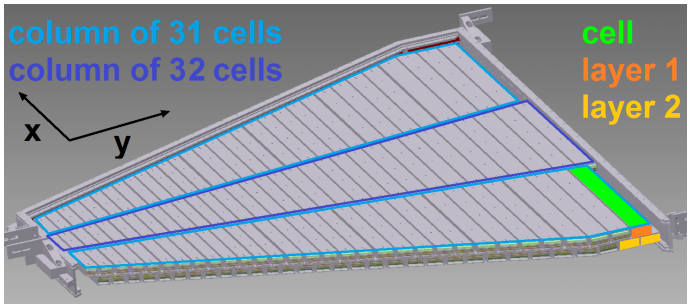

Figure 2.14: Drawing of a RPC sector consisting of 187 cells. For orientation a coordinate system is shown [72].

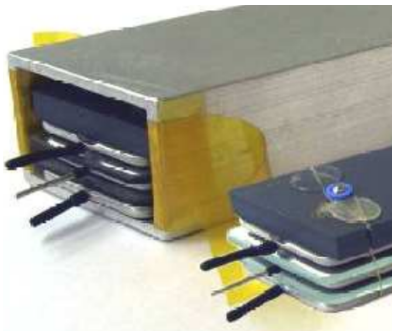

Figure 2.15: RPC cell panels in and outside the aluminium box, coated inside with kapton foil [73].

2.2.5. Forward Wall

In 2007 the Forward hodoscope Wall (FW) for EventPlane (EP) reconstruction was installed. The active area of $1.8 \times 1.8\,\mathrm{m}^2$ covers a polar angular range from 0.3° to 7.3° and is made out of 288 cubic scintillators with a thickness of 2.54 cm connected to photomultipliers. As scintillating material the same plastic is used as in the TOF wall, BC408. Corresponding to an increasing particle flux near the beam axis the dimension of the cells is scaled: 12 by 12 rows of $4 \times 4\,\mathrm{cm}^2$ sized squares are surrounding a beam hole of $8 \times 8\,\mathrm{cm}^2$, followed by 2 rows of $8 \times 8\,\mathrm{cm}^2$ and three rows of $16 \times 16\,\mathrm{cm}^2$ sized scintillators, see figure 2.16.

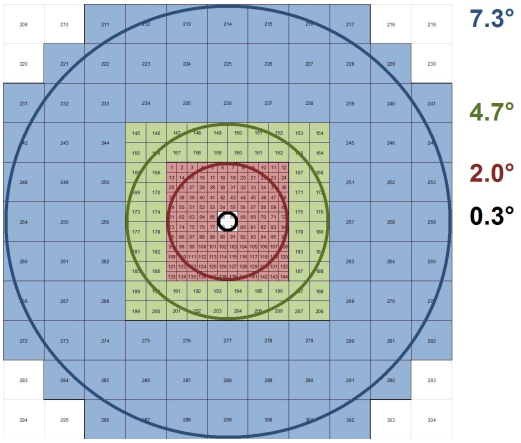

Figure 2.16: Layout of the Forward hodoscope Wall. The indicated rings around the beam axis correspond to the noted polar angles. At each corner three positions are not filled with detectors. (Differently sized cells are differently coloured: Red: $4 \times 4\,\mathrm{cm}^2$, green: $8 \times 8\,\mathrm{cm}^2$, blue: $16 \times 16\,\mathrm{cm}^2$) [74].

The Reaction Plane (RP) and the centrality of Au+Au collisions in 2012 can be determined by localising and counting the impacts of particles on the wall. As the FW is located 7 m downstream of the target, a helium filled balloon is positioned in between the HADES setup and the hodoscope to reduce multiple scattering of the spectators. Arriving particles are identified via time-of-flight measurement by communication with the START detector and their specific energy loss $\mathrm{d}E/\mathrm{d}x$. Due to the high granularity of the scintillators the probability of a double hit is moderate [75].

2.2.6. DAQ and trigger

The HADES Data AcQuisition (DAQ) system, network and Central-Trigger System (CTS) were upgraded in 2011 to ensure a fast and reliable read-out of about 80 000 individual detector cells. Higher particle multiplicities in heavy-ion collisions, as during the Au+Au beam time in 2012 at beam energies of 1.23 AGeV, required the enhancement. With a sampling rate of 8 kHz and a data rate written to storage of 200 MByte/s during the Au+Au beam time the predicted sampling rate of 70 kHz was surpassed more than 10 times. In 557 hours of data acquisition a total amount of 140 TByte was recorded, equivalent to 7.3 billion events. To reduce the dead time of the DAQ and to avoid large quantities of inconclusive data, a central-trigger system is used in HADES. Only events of a minimal multiplicity, hence of a requested collision centrality, are selected by the first level trigger (LVL1). As the decision time of LVL1 is about 100 ns, it is faster than the average time between two reactions. The decision criterion for so-called PT3-trigger was a multiplicity of more than 20 hits in the TOF wall. Moreover, the PT2-trigger selected reactions with a minimum of four tracks.

To sketch how an electrical signal is processed the MDC detector is used as an example: All signals were first amplified and discriminated by dedicated *Application Specific Integrated Circuits* (ASICs) and afterwards the time and amplitude were digitised in *Time-to-Digital Converters* (TDCs) with a time binning of 500 ps via the *Time-over-Threshold* (ToT)-measurement. ASICs and TDCs are components of the so-called *Front-End Electronics* (FEEs). These processed data are passed to the *Field Programmable Gate Array* (FPGAs) by the read-out controllers which are linked to hubs using optical fibre and are forwarded via *Gigabit Ethernet* to the event builders. A complete description of the MDC read-out can be found in [76].

The event builders prepare the data for long term storage and analysis. To enable the combination of all detector systems a special network protocol, the TrbNet has been developed, see figure 2.17.

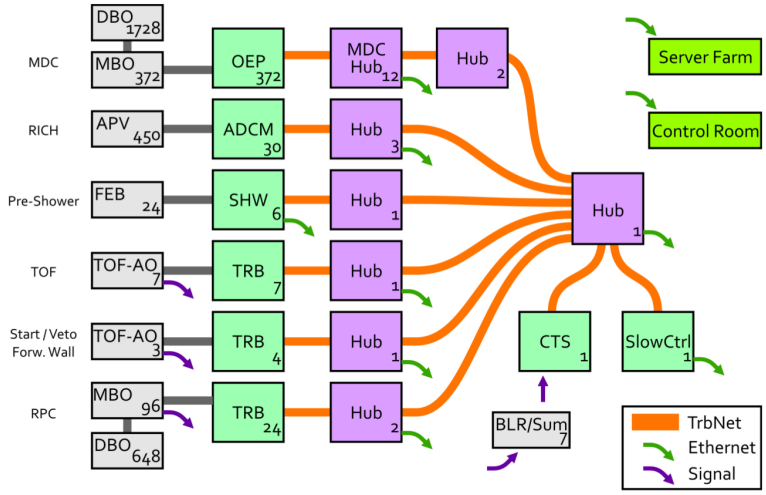

Figure 2.17: Sketch of the DAQ system. Data from the FEE is digitised and forwarded via an optical network running a dedicated protocol (TrbNet). Several FEEs combine signals that are afterwards streamed to the server farm using Gigabit Ethernet. The Central-Trigger System (CTS) controls all operations [65].

2.3. Particle reconstruction

2.3.1. Track reconstruction

Particle trajectories are reconstructed using the magnetic spectrometer. In a first step, the intersection points of the particle track with the MDC planes have to be determined. If a particle traverses a gas-filled mini-drift cell of a MDC layer an electrical signal is induced: the cell or rather the sense wire "fired". The fired wires of all layers of two MDCs (I+II and III+IV) are projected on a virtual plane located in between two MDCs, see figure 2.18. Crossing points of fired wires are intersection point candidates, called wire cluster. The left figure of 2.19 shows three true local maxima and several random crossing points.

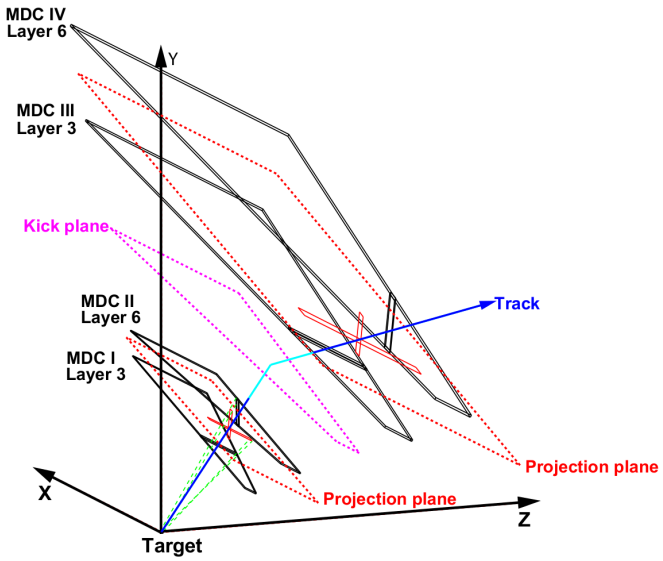

Figure 2.18: Principle of the track reconstruction: a track candidate is shown with four MDCs of one sector. Each MDC is represented by one of six layers. The inner and outer projection planes are depicted in red and the kick plane in magenta. The light blue segment of the track indicates the presence of the magnetic field bending the particle trajectory [52].

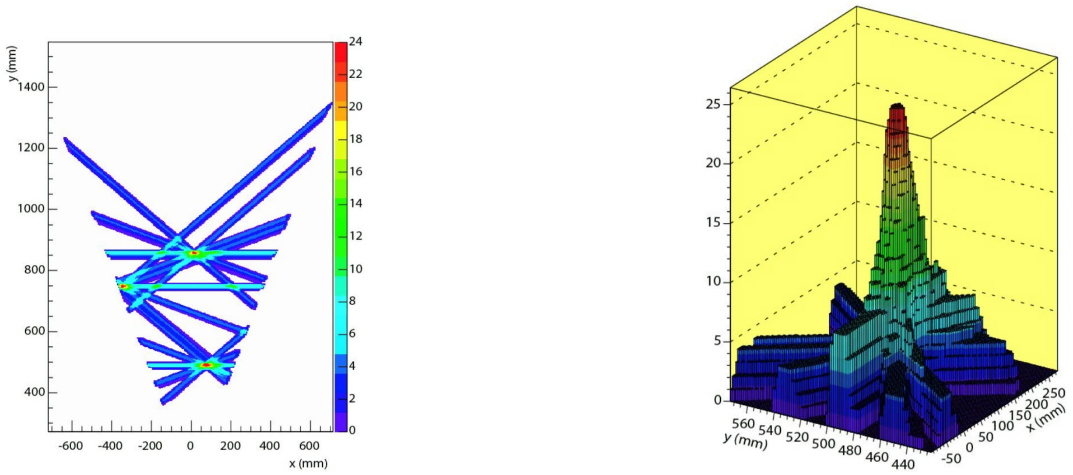

Figure 2.19: Cluster finding procedure. Left side: fired sense wires projected on a virtual plane. Right side: two dimensional representation of a wire cluster [77].

By setting a threshold to the number of fired wires, random crossing points are discarded. This threshold is adjusted dynamically to the total amount of fired wires.

The track reconstruction is structured as follows: the wire clusters of the inner MDCs and the reconstructed event vertex are used in a χ-minimisation procedure to obtain a continous particle trajectory. Extrapolating this trajectory, an intersection point of the line with the kick plane can be calculated. The kick plane is a virtual surface corresponding to the deflection points of charged particles due to the magnetic field, depicted in magenta in figure 2.18. Then, the wire clusters of the outer MDCs and the reconstructed intersection point are used in a further χ-minimisation procedure to obtain the outer segment of the particle trajectory. The appropriate combination of the inner and outer trajectory segments is called track candidate. Extrapolating the track candidate, an intersection point of the trajectory with the META-detector can be calculated. If this calculated point matches to a measured hit within a spatial condition[1] a particle track is obtained. The result of the minimisation procedure is a χ^2 value (χ^2_{inner} and χ^2_{outer}) and is a criterion for the track candidate selection [52].

2.3.2. Momentum reconstruction

The main principle of the momentum reconstruction of particles with charge q and velocity $\boldsymbol{v}$ is their deflection passing a magnetic field of strength $\boldsymbol{B}$ due to the Lorentz force $\boldsymbol{F}_L = q \cdot (\boldsymbol{v} \times \boldsymbol{B})$. Assuming a two-dimensional curvature of the particle track (with constant polar angle ϕ) an approximation of the deflection is feasible using the transverse kick $\Delta \boldsymbol{p}_{kick}$:

$$\Delta \boldsymbol{p}_{kick} = \boldsymbol{p}_{out} - \boldsymbol{p}_{in} \tag{2.1}$$

with the momentum vectors $\boldsymbol{p}_{in}$ and $\boldsymbol{p}_{out}$ for the particle before and after passing the magnetic field. As $|\boldsymbol{p}_{in}| = |\boldsymbol{p}_{out}| = |\boldsymbol{p}|$, equation (2.1) can be reformulated using the deflection angle $\Delta\theta$:

$$|\Delta \boldsymbol{p}_{kick}| = 2\,|\boldsymbol{p}| \sin\left(\tfrac{\Delta\theta}{2}\right) \tag{2.2}$$

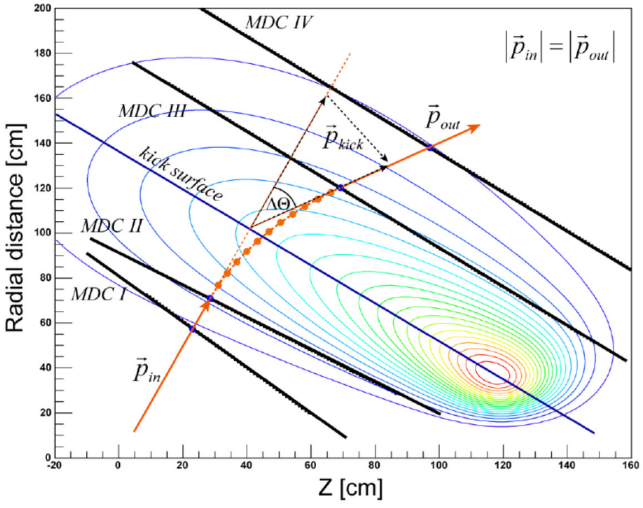

Figure 2.20: Principle of the momentum reconstruction. The particle, passing the MDCs I to IV, is deflected ($\Delta\Theta$) at the kick surface due to the transferred momentum $\Delta \boldsymbol{p}_{kick}$. Ten supporting points (coloured in orange) used by iterative reconstruction methods are also shown. The contour plot is a field map of the magnetic field between two coils [78].

[1] $\mathrm{d}x/\sigma_x$, with the error of the measurement σ_x. $\mathrm{d}y$ is defined by the dimensions of the rod of the RPC or the 4 mm sized cell of the TOF.

There are two consecutive procedures to reconstruct the momentum: the *spline method* and the *Runge-Kutta method*. A first interpolation of the particle track between the inner and outer reconstructed track segments is realised by the spline method assuming that a cubic spline can describe the particle trajectory over a short distance. Supporting points, orange coloured in figure 2.20, are generated by continuous interpolation functions over small intervals on the condition that higher order derivations are continuous in the interval and at the borders.

Then, the final momentum of the track candidates is calculated using the results of the spline method as start parameters for the Runge-Kutta procedure. Commencing at the starting point the equations of motion are numerically solved and then extrapolated to the next track point. This is followed by a check of the recursively reconstructed trajectory against the measured hit points, repeated up to eleven times, to find the optimum trajectory. χ^2_{RK}, the quality characteristic of the track, is used to select track candidates.

Multiple scattering and mean energy loss are not taken into account by this procedure, but due to the low material budget[1] the average error is below 0.5% of the radiation length [52].

[1]The total thickness per chamber is about $5 \cdot 10^{-4}$ in units of radiation length.

3. Analysis

In the beginning of this chapter, the used event and particle characterisation and selection are described, followed by a brief introduction of a re-weighting procedure to correct track losses. After explaining the estimation of the Event Plane (EP) used by the standard Event Plane Method (EPM) the Scalar Product Method (SPM) is introduced. In order to obtain an accurate measurement of anisotropic flow, a number of analysis methods are applied simultaneously to data [30]. Subsequently the results of both methods are compared, first using Monte Carlo (MC) simulations and afterwards experimental data. For MC simulations the Ultrarelativistic Quantum Molecular Dynamics (UrQMD) [23] [22] event generator in combination with the full detector simulator HGEANT[1] [79] are used. All analysis macros are based on the modular scientific software framework ROOT, developed at CERN[2]. Data of the Au+Au collisions at 1.23 AGeV recorded with HADES in April 2012 are used for the comparative analysis of the methods.

3.1. Event selection and proton identification

A selection procedure, using defined quality criteria, is applied to the recorded events to filter Au+Au collisions from background or *pile-up events*. Initially, only events corresponding to the Physical Trigger 3 (PT3) with a minimum number of 20 hits in the TOF detector are selected (`GoodTrigger`). Additionally a reconstructed hit of a beam particle by the START-detector is required (`GoodStart`) to enable a time-of-flight measurement. Undesired reactions of the beam particles with the detector or the support structure have to be rejected; the reconstructed event vertex has to be inside the target. The spatial constraint is related to the target position: $-65\,\mathrm{mm} < z < 0\,\mathrm{mm}$ along the beam axis. Moreover, the vertex reconstruction using the inner track segments (`GoodVertexCluster`) and the vertex reconstruction using track candidates, see section 2.3.1, (`GoodVertexCandidate`)) has to be successful, $\chi^2 > 0$. Events are excluded where a VETO-signal is measured after or before the START-signal (`NoVeto`) $\pm 15\,\mathrm{ns}$ and whose event vertices are not located within a given spatial volume.

Three categories of adverse events have to be removed: first, events with more than one hit in the START-detector within a time interval of -5 to $15\,\mathrm{ns}$, relative to the registered hit, are rejected (`NoStartPileUp`). Second, events with a hit in VETO-detector but without a proper START signal (15 to 350 ns) are excluded. Last, events with more TOF and RPC hits than a given threshold in a time interval of 80 to 350 ns around each START hit are excluded.

In sum, using the PT3 triggered events as reference value, about 42 % of the events are excluded from the analysed data [78]. Since all MDCs in the six sectors worked with best efficiency on day 108 (April 17 2012), all analysis of this work is performed exclusively with this data.

[1] HADES GEometry ANd Tracking package
[2] Conseil Européen pour la Recherche Nucléaire

Event characterisation

Almost all physical observables are affected by the centrality $\mathcal{C}$ of a heavy-ion collision, defined by the impact parameter b. Since a direct measurement of $\mathcal{C}$ (or b) is not feasible, other accessible observables are used for its determination in combination with pseudo-observables like N_{part} from a Glauber Model simulation [80]. To calculate the multiplicity distribution, the amount of participants from simulations is used in a simple model of particle production. Considering the wounded nucleon model, a monotonous dependence of produced charged particles N_{ch} with the number of participating nucleons N_{part} can be assumed.

N_{part} and N_{ch} are correlated with the overlapping volume of two colliding nuclei. Since N_{part} can not be measured, N_{ch} is used to describe the degree of overlap. With assuming a minimum distance of the centre of the two nuclei ($\mathcal{C} = 0\,\%$ and $b = 0\,\mathrm{fm}$) the maximum of particle production is reached. The measured charged particle multiplicities (by TOF and RPC) are compared to calculated distributions of N_{ch} by folding the N_{part}-distribution event-wise with a Gaussian distribution. The mean and the sigma of the distribution

$$N_{mean} = \mu \cdot N_{part}, \qquad \sigma = k \cdot \sqrt{\mu \cdot N_{part}} \tag{3.1}$$

can be fitted with the parameters μ and k by a minimisation procedure. This method is tested, realised and described in detail in [81], table 1 summarizes the results.

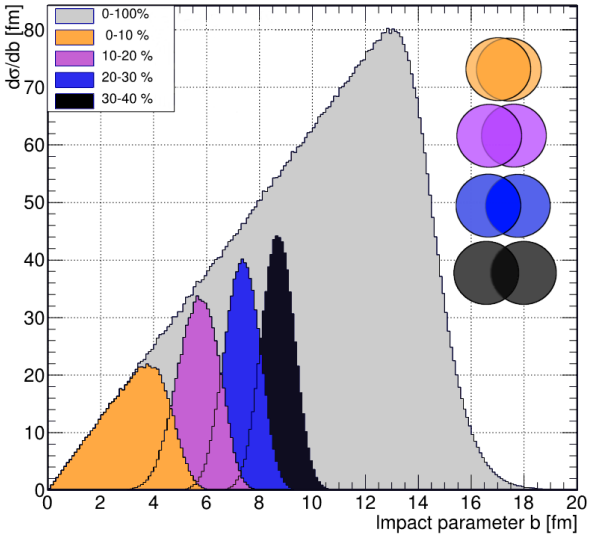

Figure 3.1: Impact parameter distribution from a Glauber Monte Carlo calculation of the total cross section for Au+Au collisions with 6.8 barn. Coloured areas represent the four centrality classes used in the analysis.

Centrality [%]	$\langle N_{part} \rangle$	b [fm] range	${N_{hits}}^{TOF+RPC}$
0 – 10	303	0.00 – 4.60	$160 \leq N < 250$
10 – 20	215	4.60 – 6.50	$121 \leq N < 160$
20 – 30	150	6.50 – 7.95	$88 \leq N < 121$
30 – 40	103	7.95 – 9.18	$60 \leq N < 88$

Table 1: Definition of the centrality classes using the mean number of participating nucleons $\langle N_{part} \rangle$, the corresponding b range and the number of hits in the TOF and RPC detectors.

Proton identification

Subsequently to the event selection, several constraints are applied to discard inaccurate particle candidates before protons can be identified.

A successful momentum reconstruction by the Runge-Kutta algorithm is required. Also the measured β of the track has to be greater than zero and the determined time-of-flight shall not exceed 60 ns. Additionally, χ^2_{RK} of the track reconstruction procedure has to be smaller than 400 and $\chi^2_{inner} > 0$. After all, the extrapolation of the reconstructed particle track must have an appropriate hit in the META-detectors: the maximum permissible deviation is 4 mm in y and 3σ in x-direction.

If a track segment or a META-hit is shared by two or more candidates, the track with the smallest χ^2_{RK} of the Runge-Kutta momentum reconstruction is taken.

Moreover, tracks which have been reconstructed at the edges of each MDC are discarded from the analysis as the results of MC simulation differ from experimental data and can not be taken as a reference in other uses as such as in the verification of the detector acceptance.

The start time t_0 of the event is reconstructed using the selected tracks. Hence, the respective β of the particles can be adjusted and inadequate tracks are removed [52].

Several quantities are used for particle identification: velocity β, momentum p, polarity q and specific energy loss $\mathrm{d}E/\mathrm{d}x$. The reconstructed track length s from the Runge-Kutta procedure and the time-of-flight measurement, determining the time interval Δt between the START-signal (t_0) and the arrival time in the META-detector (t_1), are used for the calculation of the particle velocity β.

$$\beta = \frac{v}{c} = \frac{s}{c \cdot \Delta t} \tag{3.2}$$

The momentum and the polarity of a charged particle can be estimated using the reconstructed curvature of the particle trajectory, caused by the magnetic field. Positively charged protons are bended towards the beam line due to the orientation of the magnetic field. As the degree of deflection decreases with the particle velocity, the momentum reconstruction is feasible. With these two quantities the particle mass m can be obtained by

$$\frac{m}{q} = \frac{p}{q} \cdot \frac{1}{c \cdot \beta \cdot \gamma} \tag{3.3}$$

with the Lorentz-factor $\gamma = (1-\beta)^{-1/2}$. The correlation between the velocity and the momentum is given for each particle species by

$$\beta = \frac{p}{m} \cdot \left(1 + \left(\frac{p}{m}\right)^2\right)^{-1/2} . \tag{3.4}$$

The measured values of the reconstructed tracks after the event and track selection are distributed around this mean, drawn as a line in each panel of figure 3.2. Velocities higher than one ($\beta > 1$) can be explained by the resolution of the time measurement. In the first step of the proton identification only particles that are located within an area of $4.5\,\sigma$ around this mean are selected. The second selection criterion uses the specific energy loss and the description is given on pages 28 to 30.

Due to the slightly different resolution of the time-of-flight detectors, TOF and RPC, the measured values are shown separately.

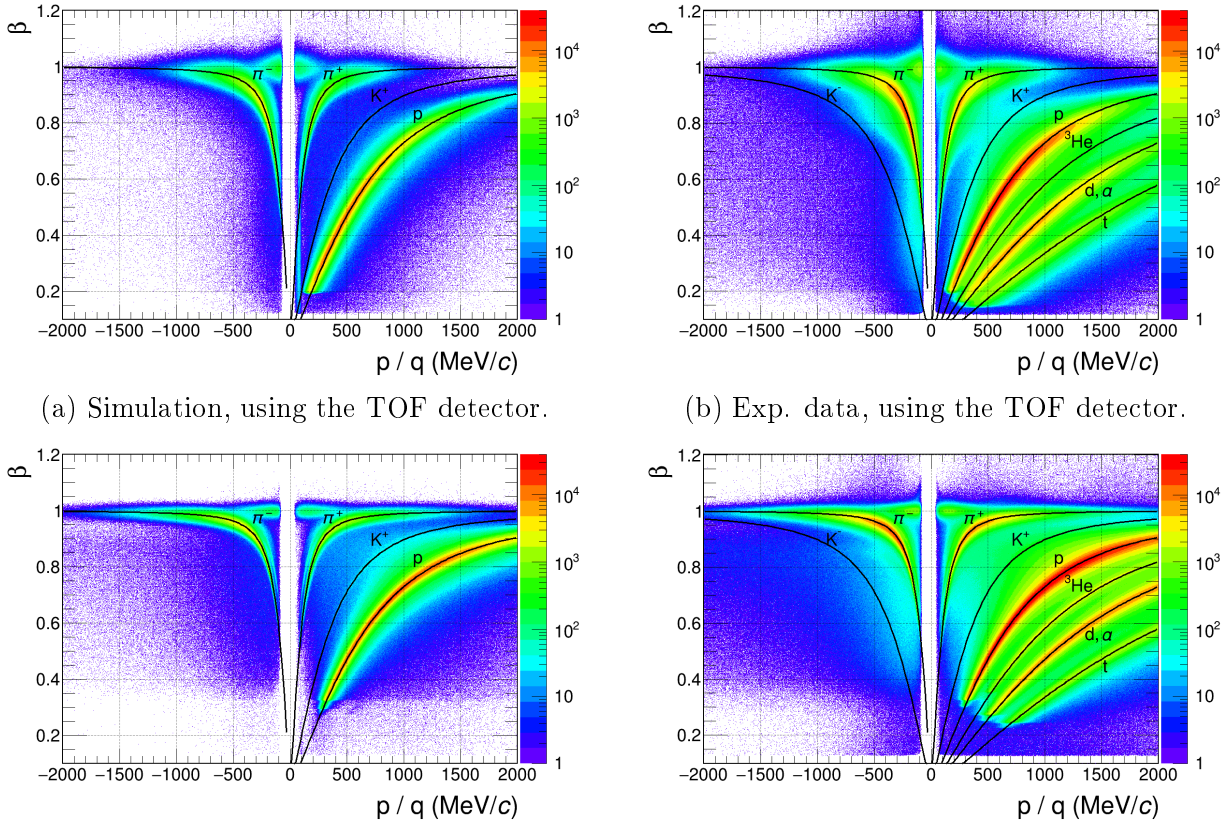

(a) Simulation, using the TOF detector.

(b) Exp. data, using the TOF detector.

(c) Simulation, using the RPC detector.

(d) Exp. data, using the TOF detector.

Figure 3.2: After event and track selection: correlation between β and p/q of all selected tracks from simulation (left column) and experimental data (right column) measured in the TOF- (upper row) and the RPC-detector (lower row).

The average energy loss of a particle $-\langle \mathrm{d}E/\mathrm{d}x \rangle$ traversing a medium depends on its velocity β and charge z and is given by the Bethe-Bloch formula [82]:

$$-\left\langle \frac{\mathrm{d}E}{\mathrm{d}x} \right\rangle = K \cdot \frac{z^2}{\beta^2} \cdot \frac{Z}{A} \cdot \left[\frac{1}{2} \cdot \ln\left(\frac{2\, m_e c^2\, \beta^2 \gamma^2\, T_{max}}{I^2} \right) - \beta^2 - \frac{\delta\,(\beta\gamma)}{2} \right] \tag{3.5}$$

with:

K	-	$4\pi\, r_e^2 m_e c^2 N_A$
z, β	-	particle charge and velocity over speed of light
Z, A	-	atomic number and mass of the traversed material
I	-	mean excitation energy of the material ($I = I_0 \cdot Z$) with $I_0 = 18.8\,\mathrm{eV}$ and $Z = 18$ for Argon and $I_0 = 13.7\,\mathrm{eV}$ and $Z = 22$ for CO_2 [83]
N_A	-	Avogadro constant: $6.022140857(74) \cdot 10^{23}$ 1/mol [84]
m_e, r_e	-	electron rest mass and radius
$\delta\,(\beta\gamma)$	-	density correction term
T_{max}	-	maximum kinetic energy a free proton can absorb in an elastic scattering process

The reconstructed particles are distributed around the expected values, drawn lines in figure 3.2 according to the Bethe-Bloch formula. Besides the hard cut of $4.5\,\sigma$ in the β-momentum distribution, only particles are selected if they are located within a $3\,\sigma$ area around this expected curve.

Both cuts are assigned to the particle candidates. The best matching candidate (in terms of deviation from the expected values from the measured momentum by tracking) is identified as a proton [85]. The energy loss of the particles is measured with the four layers of the MDC and the momentum with the time-of-flight detectors TOF and RPC[1].

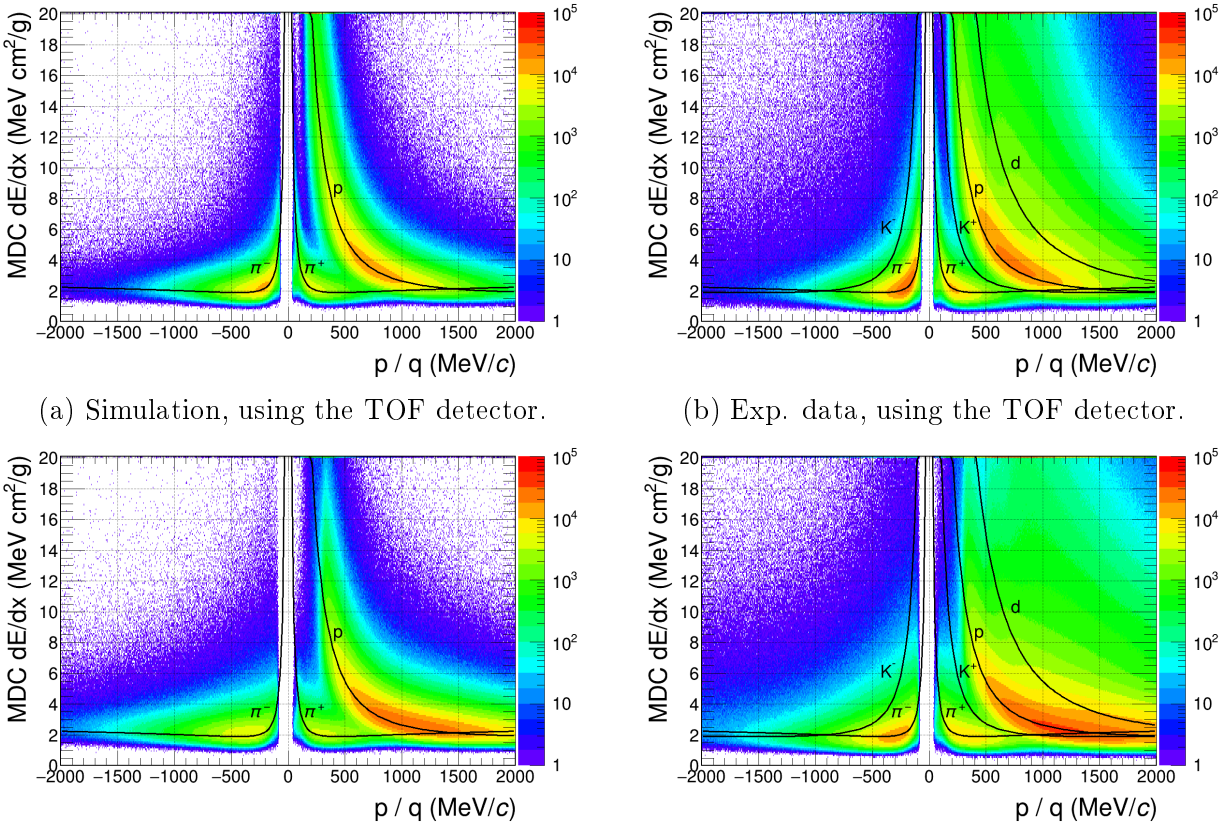

(a) Simulation, using the TOF detector.

(b) Exp. data, using the TOF detector.

(c) Simulation, using the RPC detector.

(d) Exp. data, using the RPC detector.

Figure 3.3: After event and track selection: correlation between the specific energy loss, measured with the MDCs, and the momentum, measured with the TOF- (upper row) and the RPC-detector (lower row). Simulated data is shown in the left column and experimental data in the right column.

After applying the particle identification to select proton tracks, following distributions are obtained for simulations (left side) and experimental data (right side). The reconstructed mass spectra of simulated and experimental data are displayed in the last row of figure 3.4. Blue highlighted is the mass distribution of identified protons around their nominal mass of $\approx 938.27\,\mathrm{MeV}/c^2$ [84]. Since the measured mass is divided by the particle charge, the mass distributions of negative particles (e^-, π^- and K^-) are shown on the left side of the figures.

[1] A representation of the specific energy-loss measured with the TOF detector is waived. A specific deviation can be found in the particle distribution: since slow particles are stopped in the detector material, a "stopping" peak appears at low momenta.

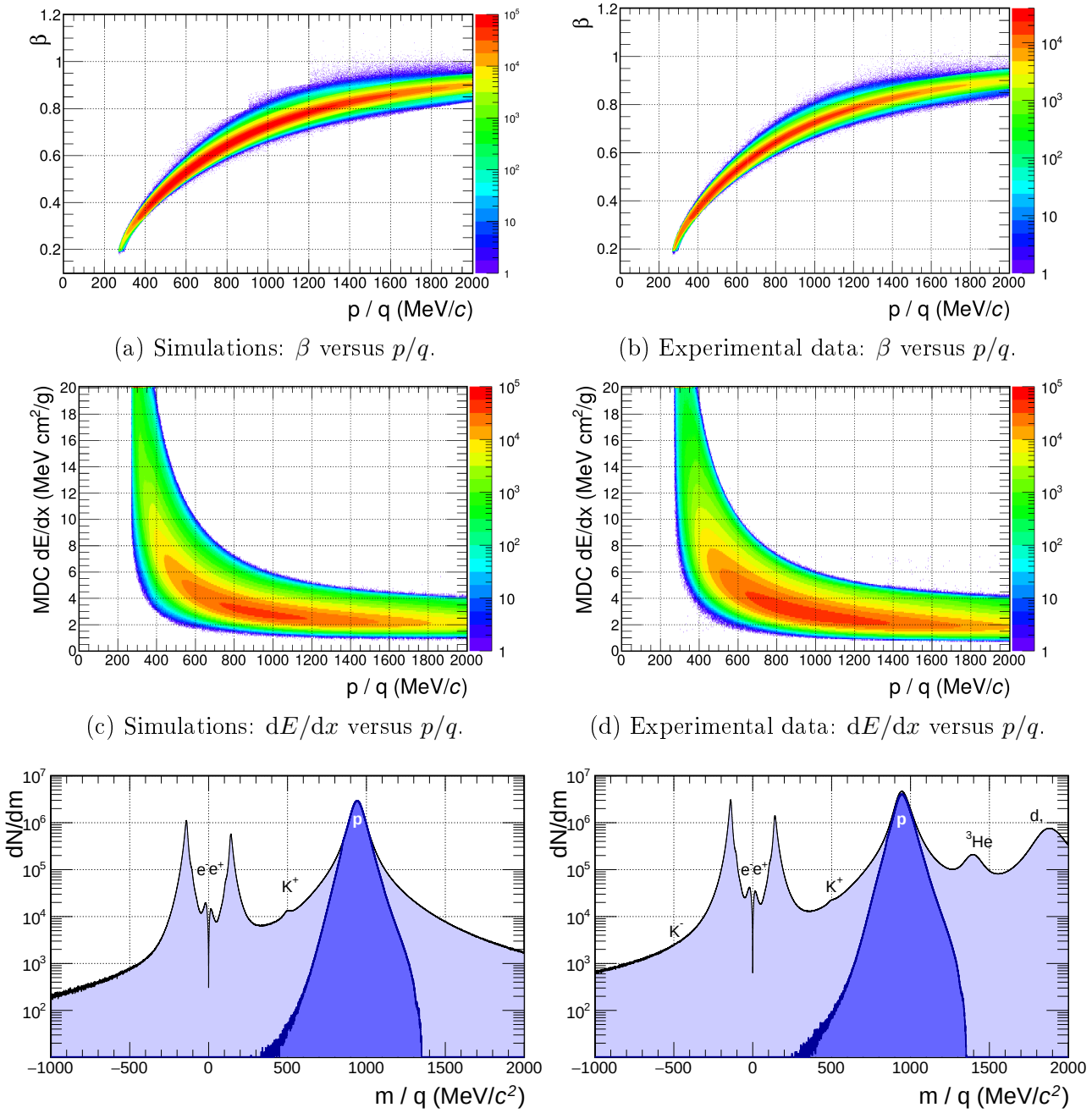

(a) Simulations: β versus p/q.

(b) Experimental data: β versus p/q.

(c) Simulations: $\mathrm{d}E/\mathrm{d}x$ versus p/q.

(d) Experimental data: $\mathrm{d}E/\mathrm{d}x$ versus p/q.

(e) Simulations: mass spectrum.

(f) Experimental data: mass spectrum.

Figure 3.4: Sample of selected protons after the event and track selection and particle identification of simulated (left column) and experimental data (right column). The measurements of the momentum or rather the mass with the time-of-flight detectors TOF and RPC are shown together in each panel. In the first row the β versus momentum distribution, in the second row the specific-energy loss versus momentum is depicted. The mass spectra are shown in the last row, highlighted is the mass distribution of selected protons.

After the event and track selection, this sample of protons is provided for the following analysis. The acceptance and the reconstruction of the HADES setup limits the observable phase space of protons in transverse momentum (p_t) and rapidity (y) as shown in figure 3.5. The rapidity y is specified relative to the centre of mass ($y_{cm} = 0.741$).

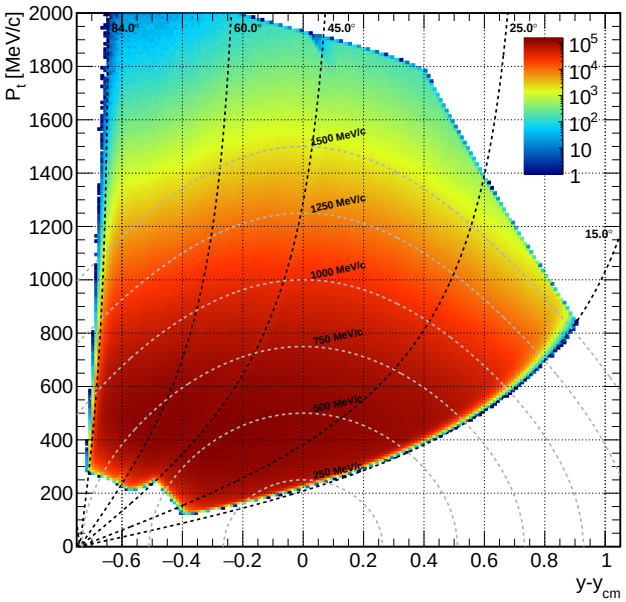

Figure 3.5: Phase space distribution of protons, measured with HADES [74]. The black dashed lines represent polar angles, grey lines represent the transverse momentum.

3.2. Relative efficiency correction

As the track reconstruction is affected by high track densities, a three dimensional reconstruction correction was applied to experimental data [86]. Phase spaces with high track multiplicities, see figure 3.6 below, have to be corrected for inefficiency. Hence, a relative correction factor is calculated depending on the polar angle θ, the azimuthal angle relative to the event plane angle ($\Phi = \phi - \Psi_{EP}$) and the centrality class, shown in following figure 3.7. The axis, the chosen ranges and sizes of the bins of the quantities can be found in table 2.

Coordinate	θ [°]	Φ [rad]	Centrality
Number of bins	80	90	10
Minimum	10	0	0
Maximum	90	2π	50

Table 2: Bin setting of the efficiency correction.

Setting Φ to a fixed value, $\Phi = 0°$ for instance, the re-weighting matrix shows a dependence on θ. Since the track reconstruction efficiency is decreasing for an increasing track multiplicity, the following parametrisation can be used, with $\mathcal{C}$ for centrality:

$$\varepsilon\left(\theta, \Delta\Psi, \mathcal{C}\right) = \varepsilon_0 \left(1 - k \cdot N_{track}\left(\theta, \Delta\Psi, \mathcal{C}\right)\right) \tag{3.6}$$

The parameter $\varepsilon_0 = 0.98$ was determined by simulations, whereas the value of the factor k has to be set such that the directed flow of protons crosses zero for mid rapidity. This correction was applied to experimental data and caused an improvement of the directed flow values calculated by both methods. No efficiency correction is applied to MC simulations. Since the particle reconstruction of MC events has a smaller influence on the calculated flow coefficients compared to the effect of the EP reconstruction, see section 3.7.1, a correction of track loss is assumed to be of minor importance.

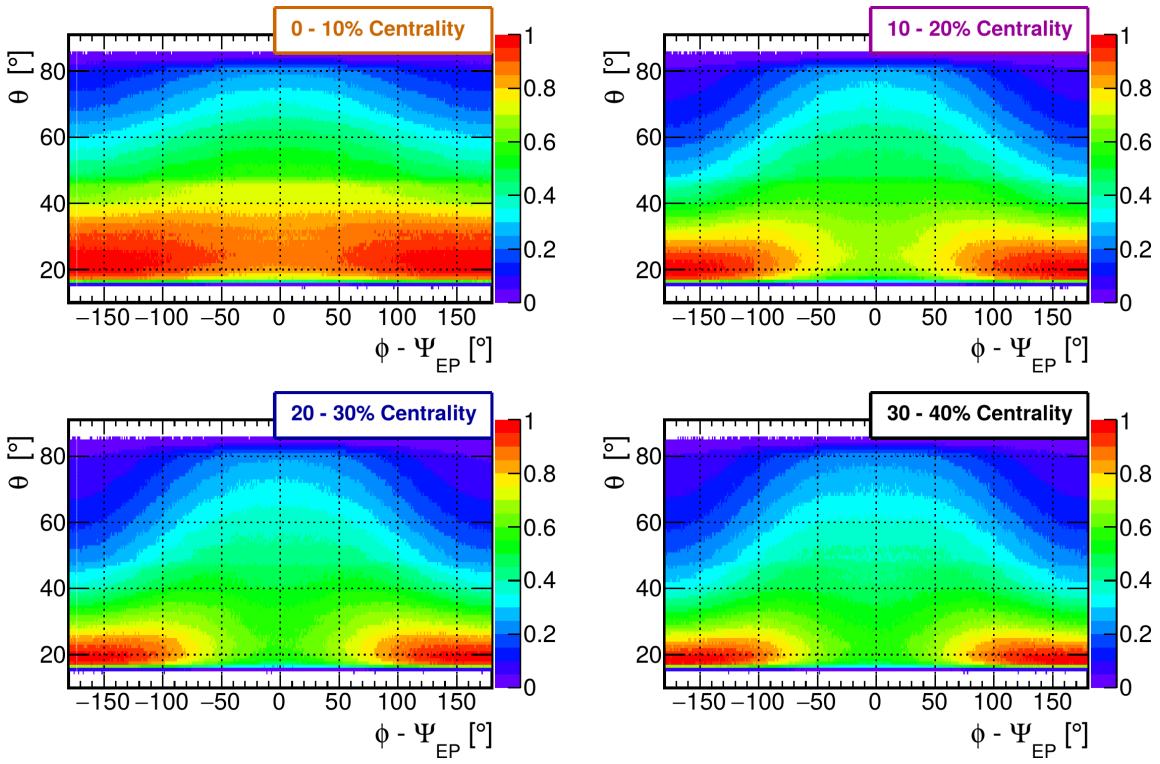

Figure 3.6: Track multiplicity of experimental data as a function of Φ and θ of each centrality class. Each distribution of selected tracks is normalized to the value of its highest multiplicity.

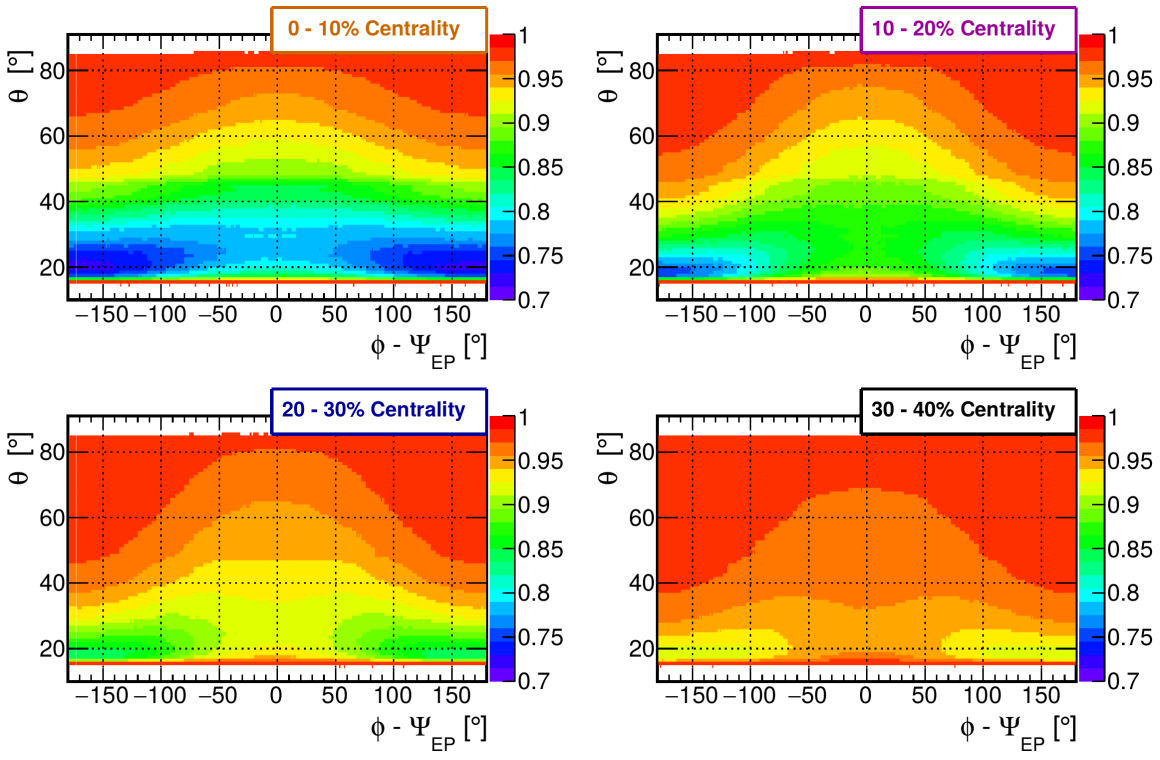

Figure 3.7: Relative efficiency matrices of experimental data in dependence of Φ and θ of each centrality class.

3.3. Estimation of the event plane

Anisotropic flow can be defined relative to the Reaction Plane (RP), which is spanned by the impact parameter b and the beam direction [28]. Since a direct measurement of the RP of a heavy-ion collision is not feasible, it has to be reconstructed and its estimation is called Event Plane (EP). To obtain the event plane angle (Ψ_{EP}) the FW was installed to measure incoming projectile spectators (hereinafter referred to as spectators). The spatial distribution of hits from spectators is used to determine the EP, or rather the $\boldsymbol{Q}$-vector, see figure 3.8.

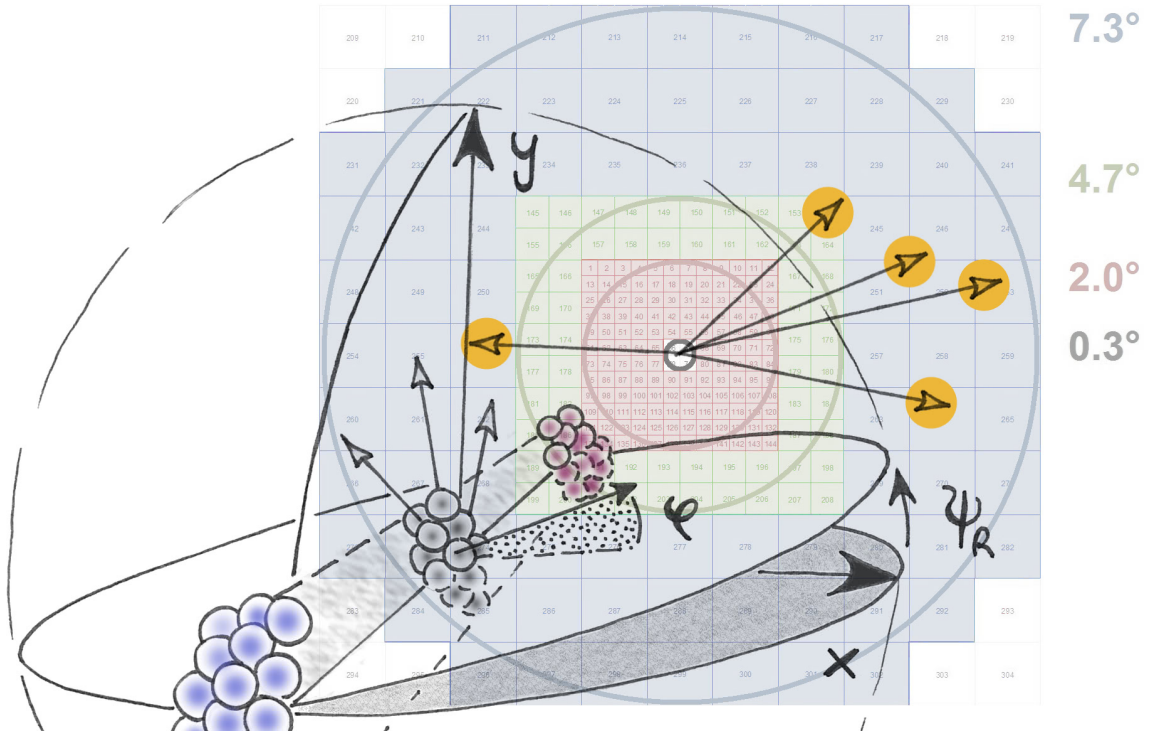

Figure 3.8: Drawing of a heavy-ion collision in the laboratory frame. Spectators produced by the collision (shown in red) move towards the FW in direction of the beam line. Their straight trajectories as well as their projection onto the FW are represented by solid arrows. Impact points, the end of the trajectories, are depicted as yellow circles.

Following equation (3) of [87] the $\boldsymbol{Q}$-vector can be found via summing up all hit positions $\vec{r}_i$[1]:

$$\boldsymbol{Q} = \sum_{i=1}^{N_{sp}} \frac{\vec{r}_i}{|\vec{r}_i|} \quad . \tag{3.7}$$

The x and y components of the n-th harmonic event $\boldsymbol{Q}$-vector are given by

$$Q_{n,x} = \sum\nolimits_i \cos(n\,\phi_i) \qquad \text{and} \tag{3.8}$$

$$Q_{n,y} = \sum\nolimits_i \sin(n\,\phi_i) \quad . \tag{3.9}$$

[1]Frequently a weight w_i is used, see equation (4) of [24] or rather equation (5) of [88], which may depend on the type of particle, its rapidity and transverse momentum. Hereinafter weights will not be mentioned as all calculations of this work are done without weighting.

However, n is to set 1 since the $\boldsymbol{Q}$-vector is generated using spectators that are located within the EP. The event plane angle Ψ_{EP} is given by:

$$\Psi_n = \frac{1}{n} \cdot \arctan \frac{\sum_i \sin(n\,\phi_i)}{\sum_i \cos(n\,\phi_i)} \quad . \tag{3.10}$$

As the sums run over the hits in the FW, the precision of the event plane estimation depends on the number of measured spectators and their "dispersion". Dispersion means the event-by-event discrepancy between the estimated EP from the RP ($|\Psi_{EP} - \Psi_{RP}|$). The discrepancies over all events are assumed to be Gaussian distributed.

3.4. Re-centring procedure of the event plane angle

Since the hit point of the beam is not located in the centre of the FW, see figure 3.9, a *re-centering procedure* has to be applied [24] in order to flatten the event plane angle distribution and to remove *acceptance correlations*, see figure 3.10. Acceptance correlations are biases due to the finite acceptance of the detector and cause the particles to be azimuthally anisotropic in the laboratory system [28]. Uneven event plane angle distributions affect the value of the calculated flow coefficients.

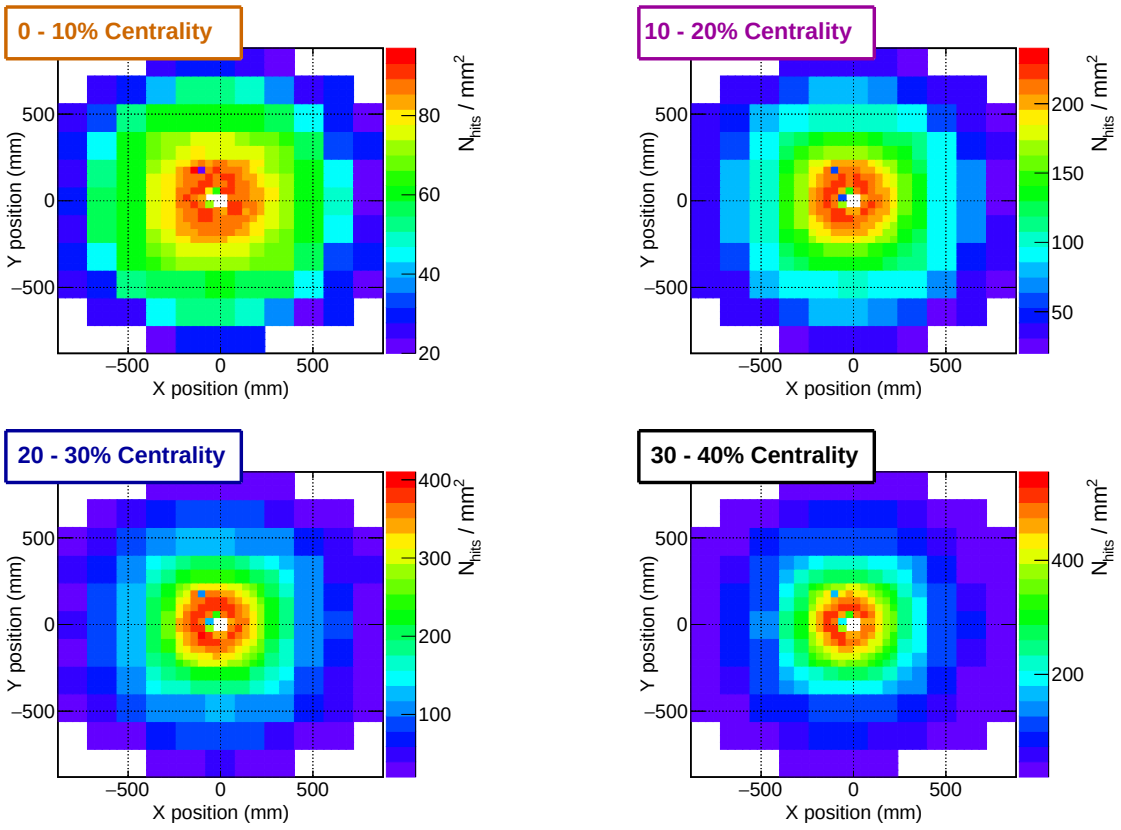

Figure 3.9: Hit density: recorded hits on the FW divided by the scintillator surface within the respective centrality class. A displacement of the hit point of the beam to the top left can be noted. The innermost cells measure $4 \times 4\,\mathrm{cm}^2$, the cells in the middle $8 \times 8\,\mathrm{cm}^2$ and the outer ones $16 \times 16\,\mathrm{cm}^2$. Darker squares indicate incorrect working scintillators.

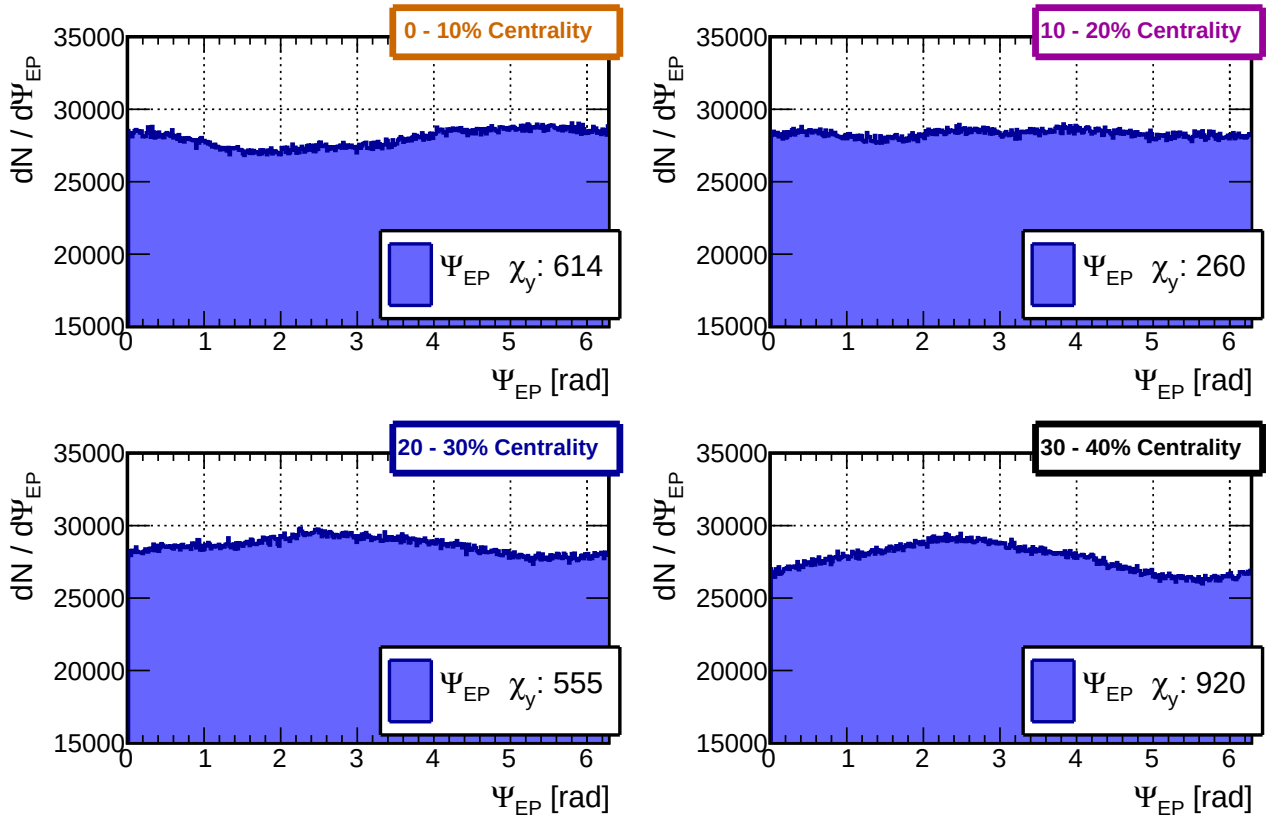

Figure 3.10: Ψ_{EP} distribution of each centrality class before re-centering. χ_y is a measure of the degree of the deviation of the angular distribution from a flat distribution. The χ_y of an absolutely flat distribution is zero.

One method to re-centre the $\boldsymbol{Q}$-vector is to subtract the mean of all measured x and y positions from the individual $\boldsymbol{Q}$-vector of each event as described in [28].

$$\boldsymbol{Q}^{corr} = \boldsymbol{Q}_i - \langle \boldsymbol{Q} \rangle \qquad = \tag{3.11}$$

$$\begin{pmatrix} Q_x^{corr} \\ Q_y^{corr} \end{pmatrix} = \begin{pmatrix} Q_{x,i} - \langle Q_x \rangle \\ Q_{y,i} - \langle Q_y \rangle \end{pmatrix} \tag{3.12}$$

An alternative procedure of re-centering is the following: in order to find the beam position where the angular distribution is almost flat, millimetre-sized values are subtracted from the beam position in x and y direction to scan the area. For each of the generated beam positions the event plane angle distribution is generated ($\mathrm{d}N/\mathrm{d}\Psi_{EP}$) and the χ_y of each distribution is calculated using

$$\chi_y = \sum_{\Psi_{EP}=0}^{n=2\pi} \sqrt{\frac{1}{n}\left(\frac{\mathrm{d}N(\Psi_{EP})}{\mathrm{d}\Psi_{EP}} - \mu\right)^2} \quad \text{with the mean} \quad \mu = \sum_{\Psi_{EP}=0}^{n=2\pi} \frac{1}{n}\frac{\mathrm{d}N(\Psi_{EP})}{\mathrm{d}\Psi_{EP}} \quad . \tag{3.13}$$

The smaller χ_y, the more equally distributed are the event plane angles. An exemplary event plane angle distribution is shown in figure 3.11. Red lines represent exemplary differences between the individual values and the mean of the distribution ($(\mathrm{d}N/\mathrm{d}\Psi_{EP}) - \mu$). The mean μ is depicted as orange line.

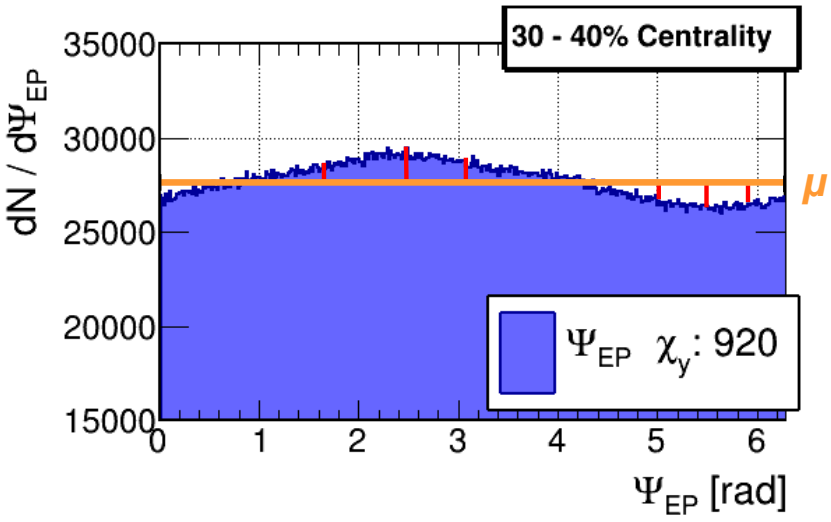

Figure 3.11: Exemplary event plane angle distribution with exemplary differences, see text.

The χ_y values, calculated for each generated beam position, are shown as colour code in figure 3.12. In order to find the beam position with the smallest χ_y value a two dimensional gauss fit is applied: its height profile is represented as red circle lines.

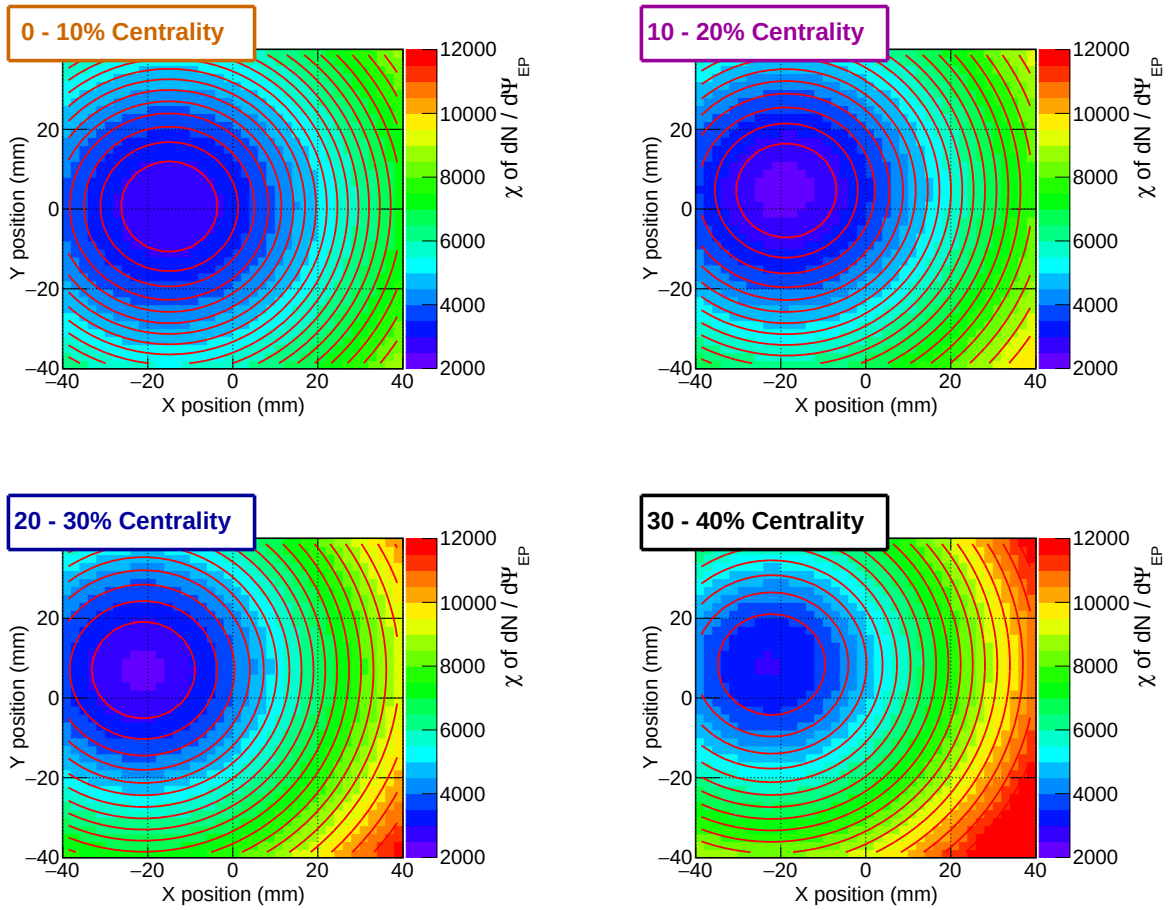

Figure 3.12: Area of the artificially shifted beam position, see text. The values of χ are represented as colour code, the two dimensional gauss fit is represented as red height profile lines.

The x and y position of the determined minimum of each centrality class is used to re-centre the $\boldsymbol{Q}$-vectors. The obtained event plane angle distributions are shown in the following figures.

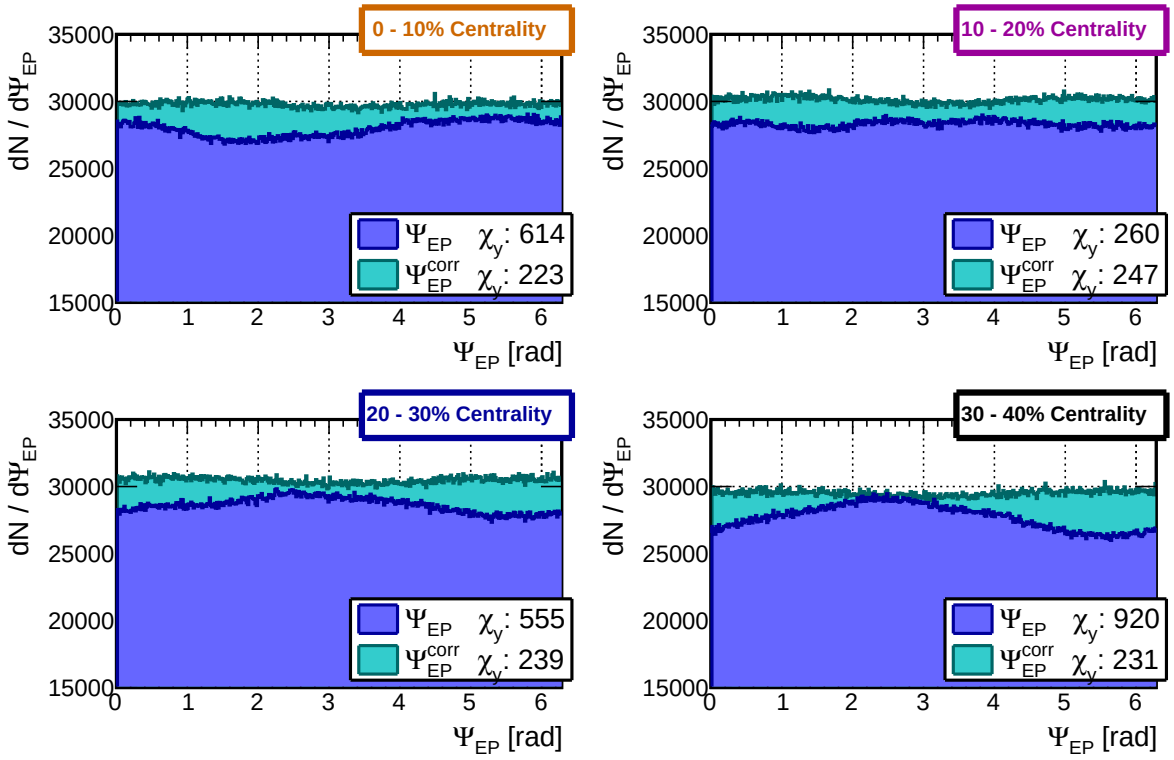

Figure 3.13: Re-centred Ψ_{EP} distribution of each centrality class using the method of [28].

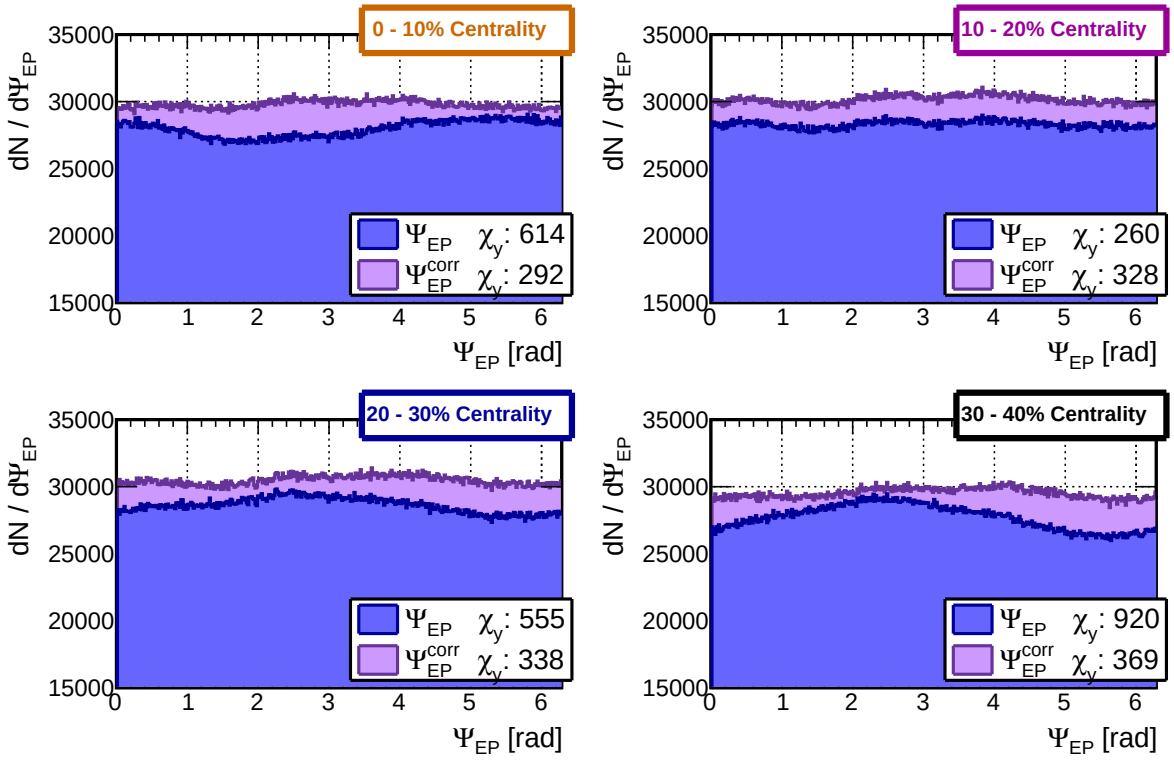

Figure 3.14: Re-centred Ψ_{EP} distribution of each centrality class using the alternative method.

The Ψ_{EP} distributions of all centrality classes are improved using the re-centring procedure of [28], see figure 3.13. As the difference of the χ_y values between the uncorrected and the corrected Ψ_{EP} distributions for 30 – 40 % most central events is the largest

$$\Delta\chi_y = \chi_y - \chi_y^{corr} = 920 - 231 = 689 \tag{3.14}$$

it may be assumed that the effect of the re-centering procedure is most pronounced for this centrality class. The alternative procedure improved three of the four distributions, see figure 3.14.

This and the higher χ_y values in total of the alternative method can be explained by the non-infinitesimal size of the scanning steps, whereas the mean of the x and y position is calculated continuously and is representing one precise value instead of an area.

3.5. The Event Plane Method

The standard Event Plane Method (EPM) and is based on the correlation of particles to an estimated event plane angle Ψ_n. The observed flow coefficient ${v_n}^{obs}\{\mathrm{EPM}\}$ of the *n-th* order is the average of the azimuthal angle ϕ_i of the selected particles with respect to Ψ_n in a given rapidity (y) and transverse momentum (p_t) bin and centrality class ($\mathcal{C}$).

The term $\langle\langle \ldots \rangle_p\rangle_e$ denotes the average over all selected particles, index p, and over all selected events, index e. In the following, the parentheses are replaced by the shorter version $\langle \ldots \rangle$.

$${v_n}^{obs}\{\mathrm{EPM}\} = \langle \cos\left[\, n\ (\phi_i - \Psi_n)\right]\rangle \tag{3.15}$$

Considering the relation of ϕ_i and Ψ_n to the reaction plane angle Ψ_{RP} one finds

$${v_n}^{obs}\{\mathrm{EPM}\} = \langle \cos\left[\, n\ ((\phi_i - \Psi_{RP}) - (\Psi_n - \Psi_{RP}))\right]\rangle \quad . \tag{3.16}$$

The first term of equation (3.16) represents the anisotropic flow coefficient $v_n\{\mathrm{EPM}\}$ and the second the EP resolution $R_n\{\mathrm{EPM}\}$. Since the particle production is symmetric with respect to the RP and the emission probability of particles is the same for $-\phi$ as for $+\phi$ the reformulation of equation (3.16) is feasible as the results in the average sine are zero. Therefore, with the angle difference identity $\cos(a-b) = \cos(a)\cos(b) - \sin(a)\sin(b)$ and the symmetry relation $\cos(-a) = \cos(a)$ equation (3.16) can be expressed as

$${v_n}^{obs}\{\mathrm{EPM}\} = \langle \cos\left[\, n\ (\phi_i - \Psi_{RP})\right]\rangle \cdot \langle \cos\left[\, n\ (\Psi_n - \Psi_{RP})\right]\rangle \tag{3.17}$$

Dividing by the second factor leads to

$$v_n\{\mathrm{EPM}\} = \frac{{v_n}^{obs}\{\mathrm{EPM}\}}{\langle \cos\left[\, n\ (\Psi_n - \Psi_{RP})\right]\rangle} \tag{3.18}$$

$$= \frac{\langle \cos\left[\, n\ (\phi_i - \Psi_n)\right]\rangle}{\langle \cos\left[\, n\ (\Psi_n - \Psi_{RP})\right]\rangle} \tag{3.19}$$

where the denominator is always smaller than one. The observed flow value ${v_n}^{obs}\{\mathrm{EPM}\}$ underestimates continuously the flow coefficient $v_n\{\mathrm{EPM}\}$ due to the finite precision of the EP determination and can be corrected by

$$R_n\{\mathrm{EPM}\} = \langle \cos\left[\, n\ (\Psi_n - \Psi_{RP})\right]\rangle \quad . \tag{3.20}$$

There are different approaches to estimate the EP resolution $R_n\{\mathrm{EPM}\}$. Generally the EP allows an estimate of all higher $v_k\{\mathrm{EPM}\}$, if the first order Ψ_n is determined, using equation (3.21)

$$v_k\{\mathrm{EPM}\} = \frac{{v_k}^{obs}\{\mathrm{EPM}\}}{\langle \cos\left[\, mn\ (\Psi_n - \Psi_{RP})\right]\rangle} \tag{3.21}$$

with $k = m \cdot n$, although the precision of $v_k\{\mathrm{EPM}\}$ decreases for growing values of m.
As a direct access to Ψ_{RP} is not feasible, the resolution can be estimated using the following procedure: the M spectators of the full event are randomly divided into two subsets, the *subevents* A and B. If A and B are of same size/multiplicity ($M_A = M_B = M/2$), an estimation of the resolution correction for the full event can be obtained, using the definition of [89]:

$$R_n\{\mathrm{EPM}\} \quad \equiv \mathcal{R}_n\left(\chi\right) \quad = \mathcal{R}_n\left(\chi_s \sqrt{M/M_s}\right) \tag{3.22}$$

with the function $\mathcal{R}_n$ of the resolution parameter χ for the full event or rather χ_s for the subevent. $\mathcal{R}_n$ for the subevent is defined by

$$\mathcal{R}_n\left(\chi_s\right) = \frac{\sqrt{\pi}}{2}\,\chi_s \cdot \mathrm{e}^{-\frac{\chi_s^2}{2}} \left(I_{\frac{n-1}{2}}\left(\frac{\chi_s^2}{2}\right) + I_{\frac{n+1}{2}}\left(\frac{\chi_s^2}{2}\right)\right) \quad , \tag{3.23}$$

with the modified Bessel function I_ν of *ν-th* order [88].
The value of the subevent resolution parameter χ_s can be calculated via $\chi_s = \sqrt{-2\,\ln\left(2\,r\right)}$, using the ratio r:

$$r = \frac{\int_{-\pi}^{-\pi/2} \mathrm{d}\Psi_{AB} + \int_{+\pi/2}^{+\pi} \mathrm{d}\Psi_{AB}}{\int_{-\pi}^{+\pi} \mathrm{d}\Psi_{AB}} \quad . \tag{3.24}$$

To obtain r, the angular distribution of Ψ_{AB} ($\Psi_{AB} = \Psi_A - \Psi_B$) is used. The Ψ_{AB} distribution and r are determined for each centrality class to calculate the resolution correction factor.
Using the ratio r to find χ_s substitutes the procedure of solving numerically the equation [24]

$$\mathcal{R}_n\left(\chi_s\right) = \sqrt{\langle \cos\left[\, n\ (\Psi_{n,A} - \Psi_{n,B})\right]\rangle} \tag{3.25}$$

With regard to addition theorems, equation (3.25) is equal to

$$\mathcal{R}_n\left(\chi_s\right) = \sqrt{\langle \cos\left(\, n\,\Psi_{n,A}\right) \cdot \cos\left(\, n\,\Psi_{n,B}\right) + \sin\left(\, n\,\Psi_{n,A}\right) \cdot \sin\left(\, n\,\Psi_{n,B}\right)\rangle} \tag{3.26}$$

$$= \sqrt{\left\langle \frac{\boldsymbol{Q}_{n,A}}{|\boldsymbol{Q}_{n,A}|} \cdot \frac{\boldsymbol{Q}_{n,B}}{|\boldsymbol{Q}_{n,B}|} \right\rangle} \quad . \tag{3.27}$$

An angular distribution with less pronounced amplitude, see figure 3.15, causes $r \to 1/2$, $\chi_s \to 0$ and a smaller resolution ($R_n \to 0$). For experimental data, the 0 – 10 % centrality bin has the lowest resolution value due to the small number of spectators at most central events. The value of the resolution for the 30 – 40 % class is slightly smaller than that of the 20 – 30 % class.

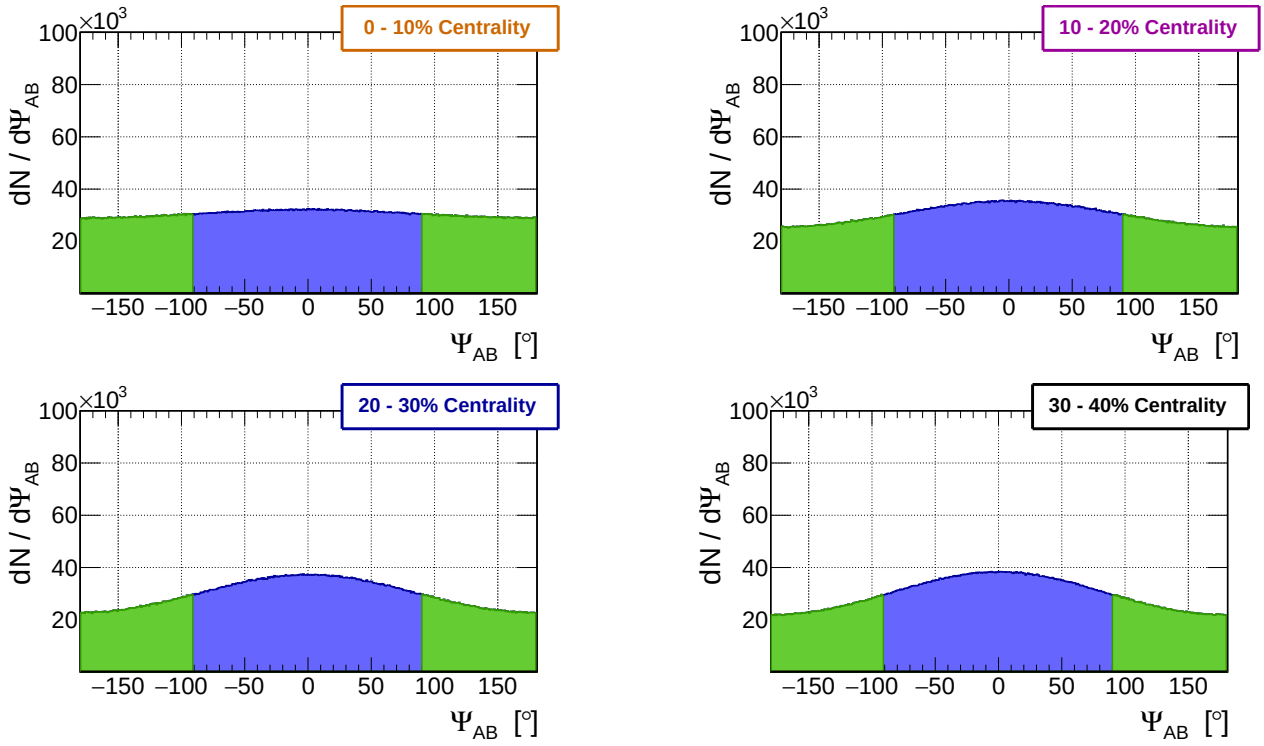

Figure 3.15: $\Psi_{\mathrm{AB}} = \Psi_A - \Psi_B$ distribution of simulated UrQMD events of each centrality bin, most central events $0-10\,\%$ in the upper left corner, most peripheral $30-40\,\%$ in the lower right corner of each group of four panels. The ratio r of the green area and the full spectrum leads to the resolution $\mathcal{R}_{\mathrm{n}}$ of the event plane, see figure 3.17.

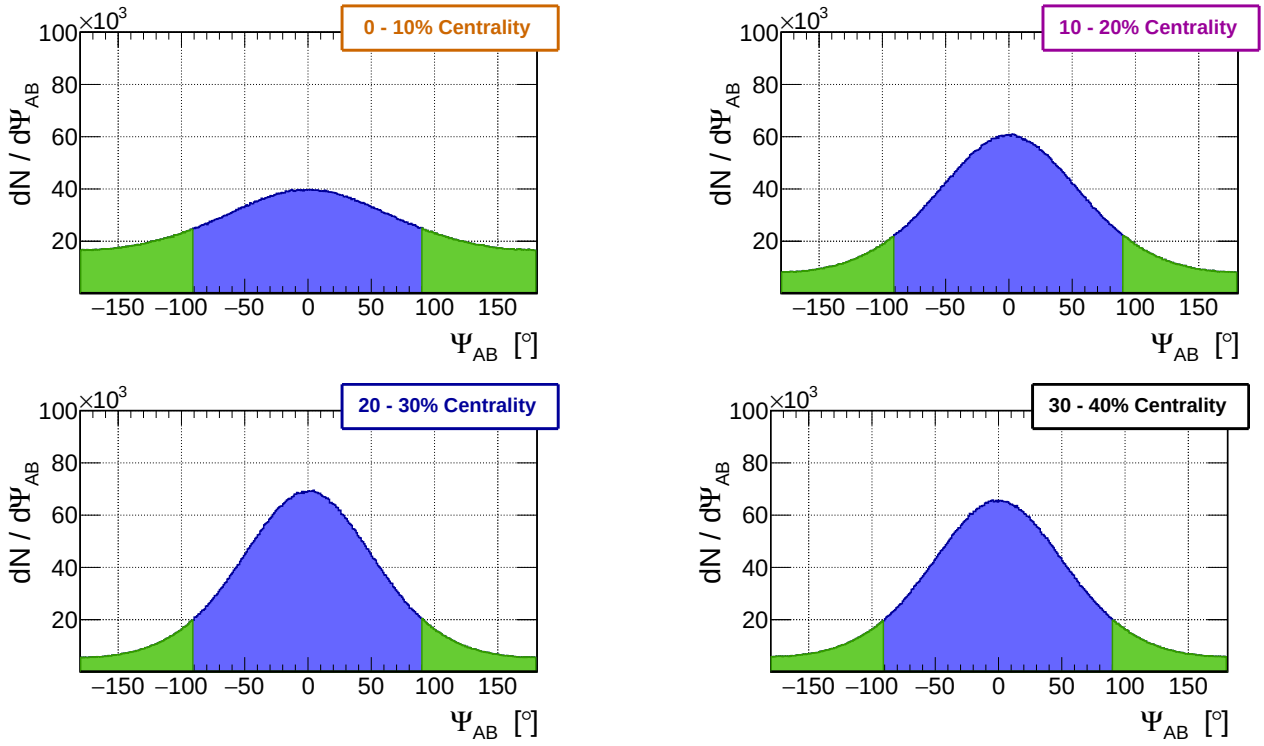

Figure 3.16: $\Psi_{\mathrm{AB}} = \Psi_A - \Psi_B$ distributions of experimental Au+Au data.

3.6. The Scalar Product Method

The method is based on the scalar product of the normalised momentum vector defined for each particle $\boldsymbol{u}_i$ with the $\boldsymbol{Q}_n$-vector of the *n-th* harmonic. Depending on the type of $\boldsymbol{Q}$-vector and how the subevents are generated, the multiplicities M of the full event and those of the subevents (M_A and M_B) have to be included or not.

The $\boldsymbol{Q}_{FW}$-vector is made up of spectators ($n = 1$). A random division of the M spectators leads to two equally sized subevents. Hence, an estimate of the flow coefficient is given by [24]:

$$v_n\{SPM\} = \frac{\left\langle \langle \boldsymbol{u}_i\,(p_t, y) \cdot \boldsymbol{Q}_{FW} \rangle_p \right\rangle_e}{2 \cdot \sqrt{\langle \boldsymbol{Q}_{n,A} \cdot \boldsymbol{Q}_{n,B} \rangle_e}} \tag{3.28}$$

with the *i-th* particle momentum vector $\boldsymbol{u}_i$ ($i \in 1, p$), the average over all selected events $\langle \ldots \rangle_e$ and the average over all selected particles $\langle \ldots \rangle_p$. If the particle momentum vectors $\boldsymbol{u}_i$ and the $\boldsymbol{Q}_n$-vector are replaced by their respective unit vectors, equation (3.28) simplifies to the EPM and the resolutions are identical: $R_n\{SPM\} = R_n\{EPM\} = R_n$, referring to the subevent resolution $R_n(\chi_s)$ of equation (3.27).

If participants from two separated rapidity intervals are used to create the $\boldsymbol{Q}$-vector and the subevents, the subevent multiplicities are not necessarily of the same size ($M_{n,A} \neq M_{n,B}$). Since this inequality introduces a variation, even for events of same total multiplicity M_n, it is necessary to normalise the vectors by their multiplicity. Referring to [30] an estimate of the flow coefficient is given by

$$v_n\{SPM\} = \frac{\left\langle \left\langle \boldsymbol{u}_i\,(p_t, y) \cdot \dfrac{\boldsymbol{Q}_n}{M_n} \right\rangle_p \right\rangle_e}{\sqrt{\left\langle \dfrac{\boldsymbol{Q}_{n,A}}{M_{n,A}} \cdot \dfrac{\boldsymbol{Q}_{n,B}}{M_{n,B}} \right\rangle_e}} \quad . \tag{3.29}$$

The nominators of equation (3.28) and equation (3.29) are the observable flow coefficients ${v_n}^{obs}\{\mathrm{SPM}\}$ and the denominators are the EP resolution $R_n\{\mathrm{SPM}\}$ according to equation (3.19). The results of both presented methods (EPM and SPM) are affected by non-flow and flow fluctuations. Non-flow is a contribution due to azimuthal correlations between particles from other sources like the HBT effect, resonance decays and momentum conservation. Flow fluctuations are resulting for instance from the variation in the initial geometry configuration of the overlapping region of colliding nuclei [24].

3.7. Analysis of Monte Carlo simulations

Before addressing the calculations of the flow coefficients $v_n\{EPM\}$ and $v_n\{SPM\}$ the resolution values for directed and elliptic flow (R_1 and R_2) are shown.

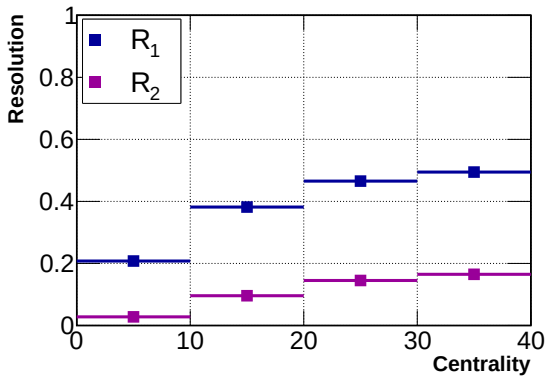

Figure 3.17: Event plane resolution of order 1 and 2 as a function of the centrality.

3.7.1. Validation using Monte Carlo simulations

Initially, both methods are validated via MC generated events of heavy-ion collisions using the UrQMD model. Three analysis approaches are realised with both methods in order to prove the accuracy of the calculated flow coefficients $v_1\{EPM\}$ and $v_1\{SPM\}$. First, the analysis methods receive protons directly from the simulation and the true RP angle Ψ_{RP} to obtain the reference values. Hereinafter, this set of protons, which does not include effects of the reconstruction is referred to as "MC set". Then, protons which passed the reconstruction procedure (MC reco) are used. Last, both methods use the estimated EP angle Ψ_{EP} and reconstructed protons for the calculation of the flow coefficients. Therefore a distinction between the influence of particle reconstruction or Event Plane estimation on the calculated flow values is possible.

The proton rapidity coverage ($-0.75 < y - y_{cm} < 1.05$) of HADES is represented by three exemplary rapidity bins, $-0.35 < y - y_{cm} < -0.25$, $-0.05 < y - y_{cm} < -0.05$ and $+0.25 < y - y_{cm} < +0.35$ in figure 3.18 and 3.19. The results for each rapidity bin are shown for both methods separately. The results of the EPM are represented by squares (left column) and those of the SPM by diamonds (right column).

Both methods are not influenced by the effects of the particle reconstruction, since the results for directed and elliptic flow are only differing slightly over a wide p_t range compared to the results using the MC set. However, the EP reconstruction has a significant influence on both methods. The discrepancies are different for the analysis of directed or elliptic flow.

As shown in the first row of figure 3.18, both methods overestimate the directed flow coefficients at backward rapidity in comparison to the results using the MC set. The results of both methods are slightly negative at mid rapidity.

The absolute difference between the obtained values ($\Delta v_n = v_n\{EPM\} - v_n\{MC\}$), one including, one excluding effects of the reconstruction procedure, is displayed for directed flow in figure 3.20 and for elliptic flow in figure 3.21. It is sufficient to show exclusively the absolute difference between the results of the EPM, since the SPM yields identical values.

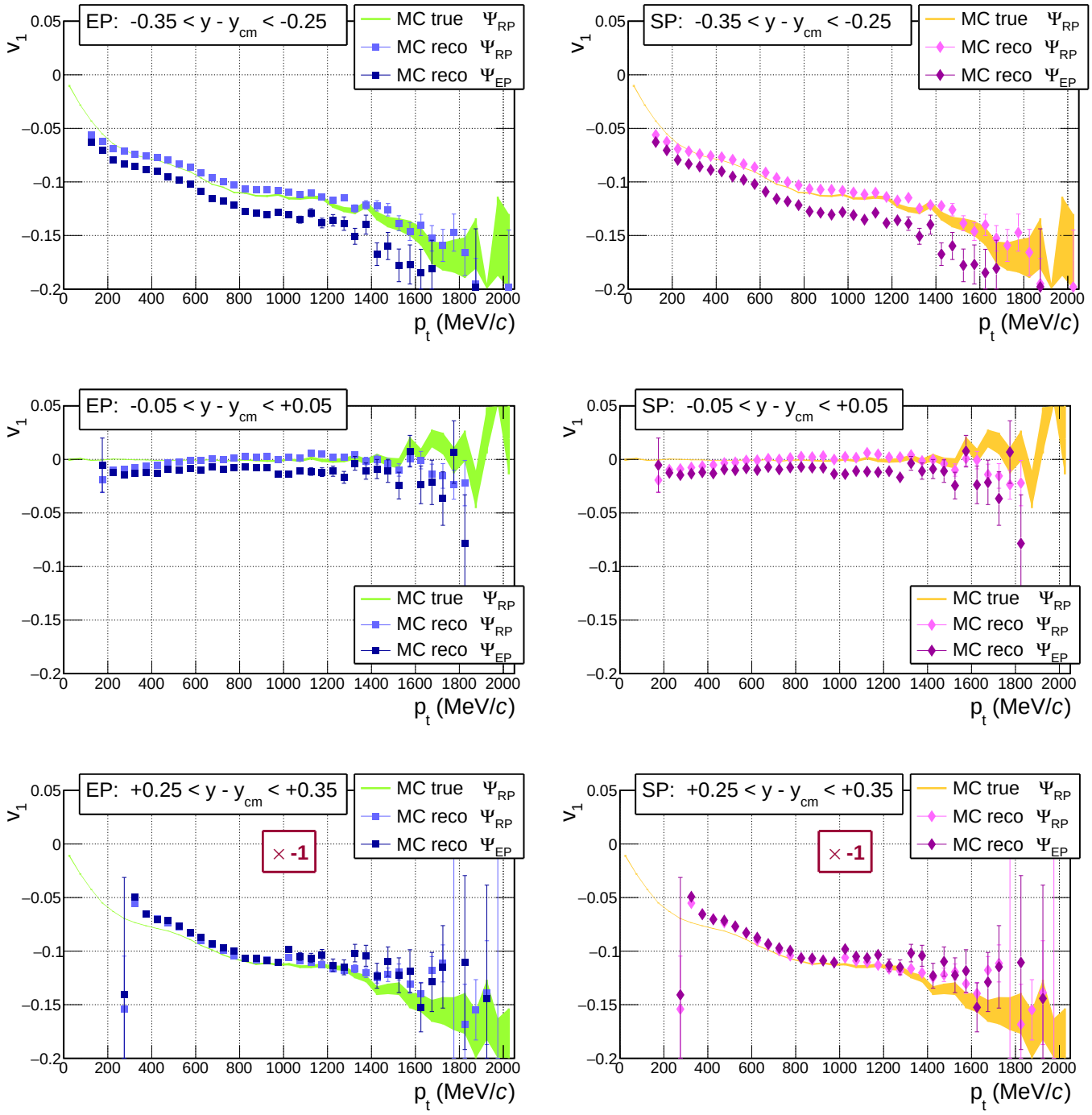

Figure 3.18: MC simulations: directed flow (v_1) versus p_t in MeV/c for 20 – 30 % most central events in three rapidity bins. A factor of -1 is applied to the results in forward rapidities to allow for a comparison to backward rapidities. The resolution is $R_1 = 0.4655$. Both methods show differing results across the three analysis variants, see text.

The results of the reconstructed set for elliptic flow at backward rapidity fluctuate around the flow values originating from the MC set but show no significant deviation, see first row of figure 3.19. At forward rapidity the flow coefficients are are overestimated (bottom row). At mid rapidity, where the elliptic flow has its highest value, both methods result in slightly higher values compared to the results using the MC set. These fluctuations resulting from the Ψ_{EP} estimation are more pronounced for elliptic flow than for directed flow.

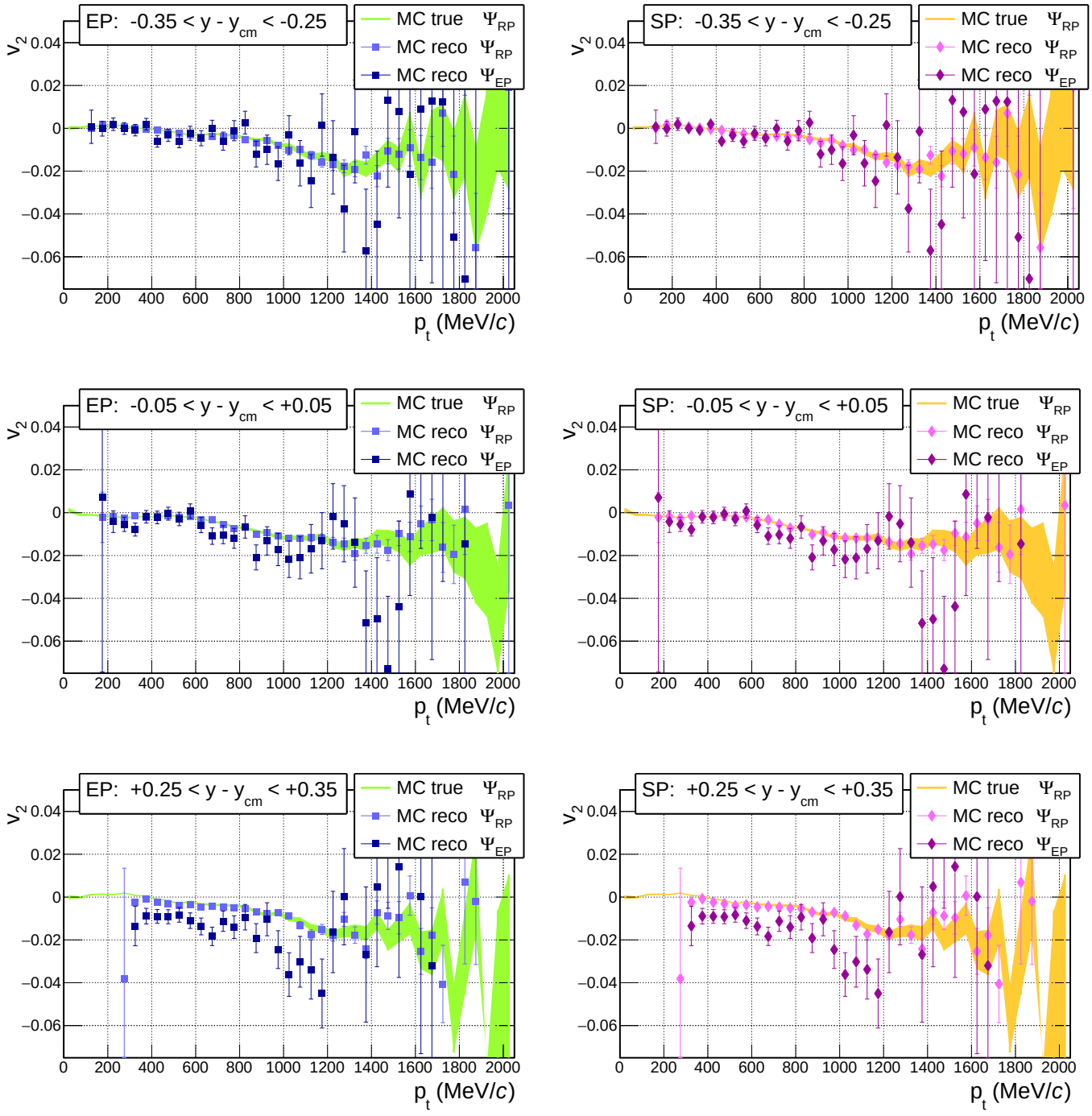

Figure 3.19: MC simulations: v_2 versus p_t in a centrality range of 20 – 30 % in three rapidity bins. R_2 is 0.145.

Due to statistical effects, the calculated values of v_2 are fluctuating slightly compared to the values of v_1. Therefore, the calculated values of the absolute difference (Δv_2) for elliptic flow are rebinned by a factor of 4, whereas Δv_1 is rebinned by a factor of 2, see figure 3.20 and 3.21.

The methods, using the reconstructed EP, overestimate v_1 compared to the values using the MC set, since Δv_1 is almost always negative along p_t. At forward rapidity the absolute value of Δv_1 is smaller than 0.02 and almost constant across the centrality classes and p_t, whereas Δv_1 in the backward rapidity hemisphere shows a centrality and rapidity dependence.

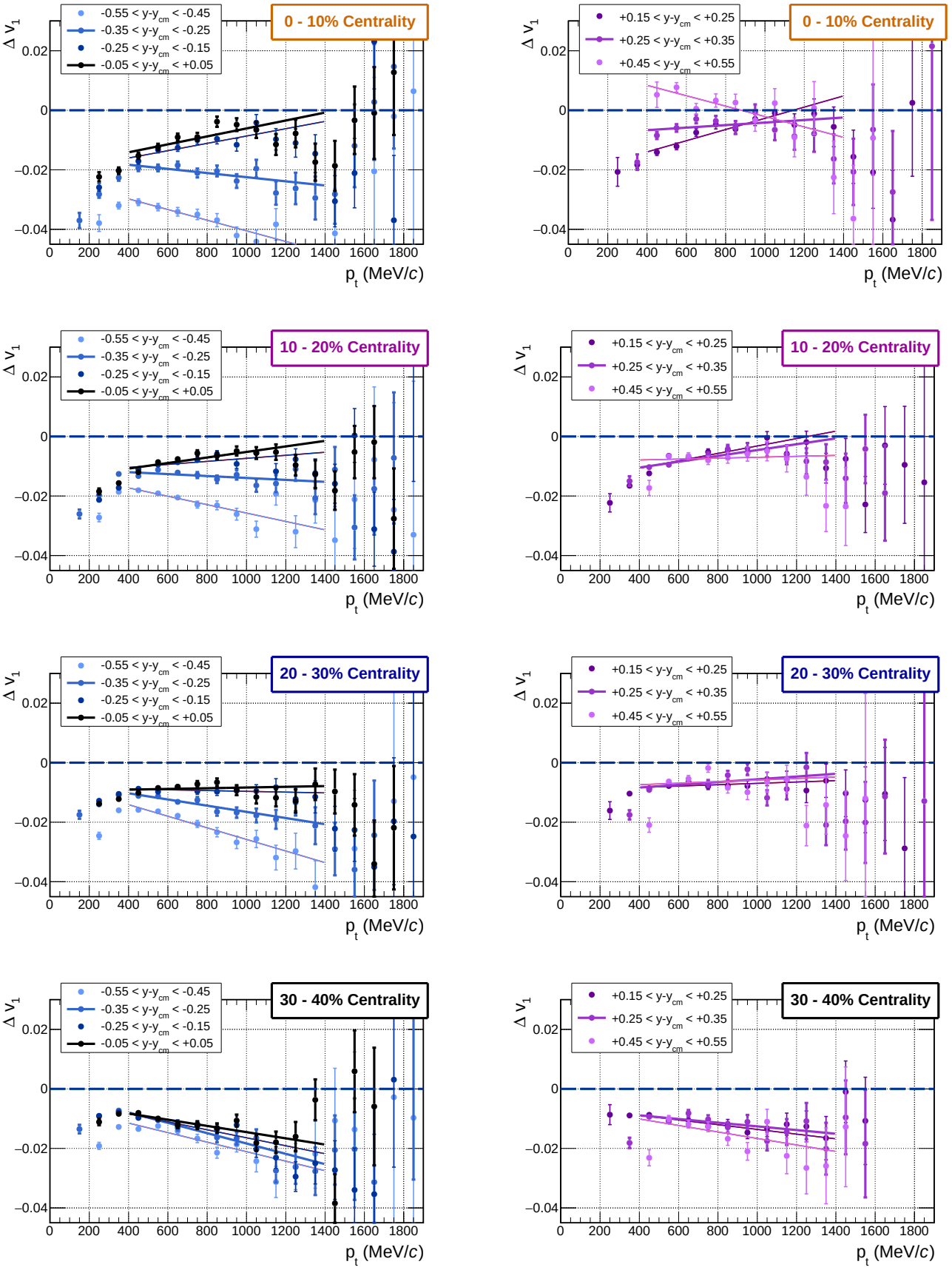

Figure 3.20: Δv_1 versus p_t: absolute difference between the calculated directed flow coefficients using the reconstructed and the MC set for seven representative rapidity bins for each centrality class. Linear fit functions are applied to each rapidity data series including values within a p_t range from 400 to 1400 MeV/c. Emphasised are the functions of the presented y bins in table 6, see section 4.

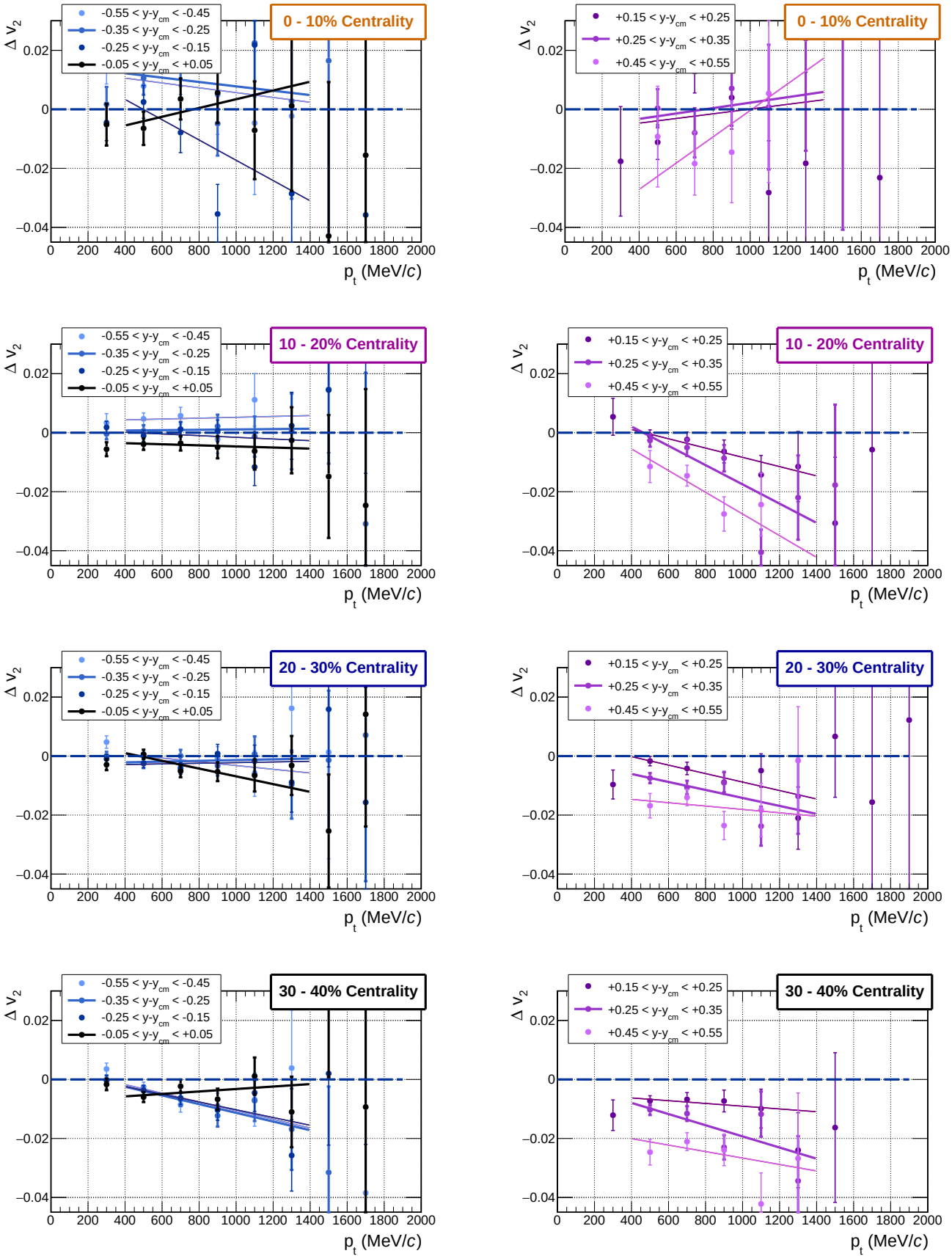

Figure 3.21: Δv_2 versus p_t of both rapidity hemispheres with linear fit functions.

Excluding the first centrality class (0 – 10 %), no explicit centrality dependence of Δv_2 can be observed for both rapidity hemispheres. Δv_2 is almost constant along the p_t-range of the applied fit functions and does not exceed an absolute value of 0.02. The trend of the fit functions at forward rapidity indicates a p_t dependence of Δv_2.

In sum, both methods receive the same results and are affected in the same way by the particle and Event Plane reconstruction for directed and for elliptic flow.

3.7.2. Spectra of directed and elliptic flow

Now the results of both methods using the reconstructed set are shown together with the results using the MC set drawn as solid line, see figures 3.22 and 3.23. The direct comparison in centrality bins reveals the equality of the calculated flow coefficients of the EPM and the SPM using the reconstructed protons and Ψ_{EP} for directed and elliptic flow. In the upper left corner the results of the 0 – 10 % centrality class is shown, comprising most central events. The 30 – 40 % centrality class is located in the lower right corner. The flow value of each method, rapidity bin and centrality class is calculated.

The rapidity space is represented by exemplary rapidity bins: the mid rapidity bin and two backward rapidity bins are chosen for v_1 as directed flow is symmetric to zero at mid rapidity. As elliptic flow is less pronounced, only one backward rapidity bin is chosen for v_2. These bin selections for directed and elliptic flow are used in the following.

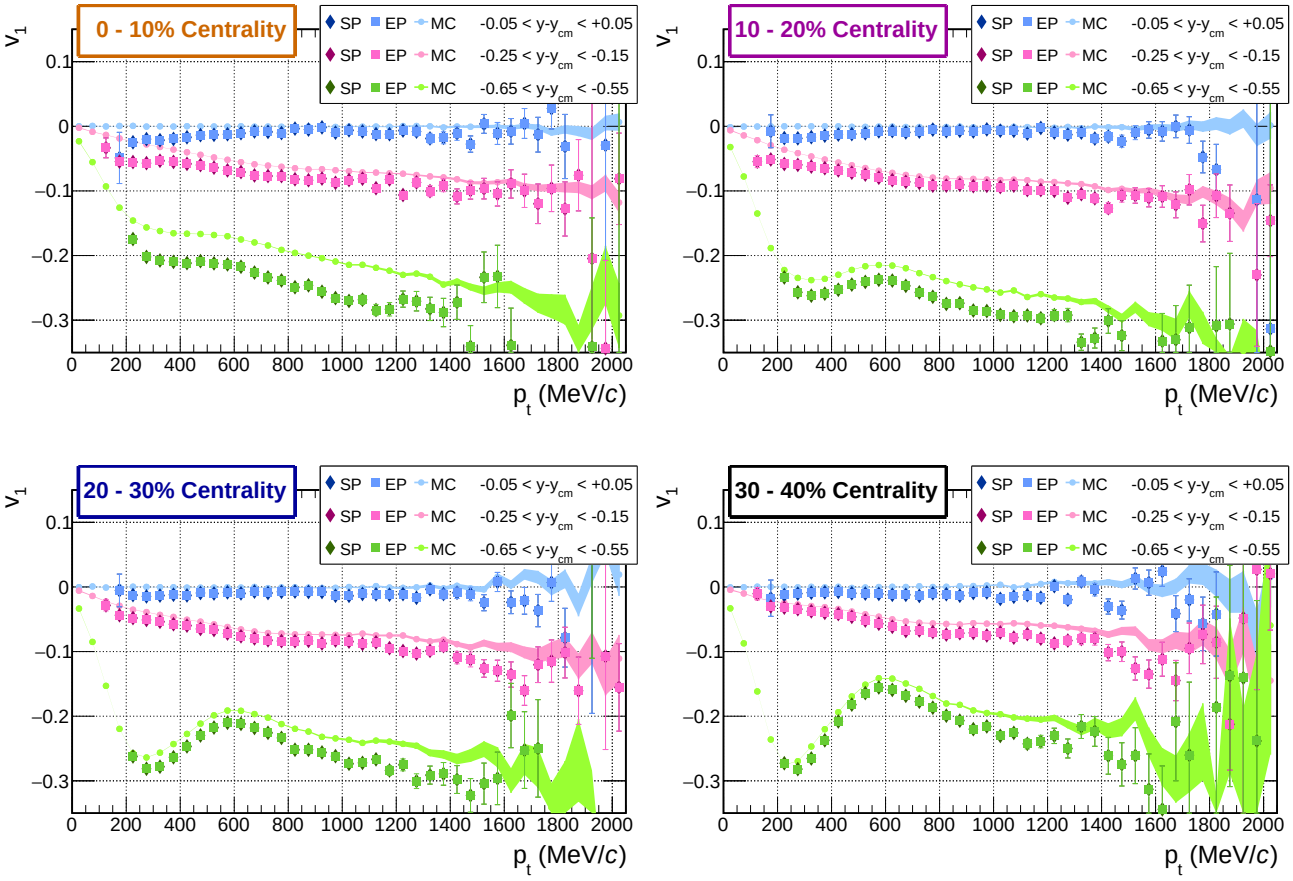

Figure 3.22: $v_1\{EP\}$ and $v_1\{SP\}$ versus p_t of MC simulated Au+Au events. Each colour represents a rapidity bin: blue corresponds to mid rapidity, red and green to backward rapidity bins.

Both methods receive the same results for directed flow, but overestimate the MC true values nearly continuously. The deviation seems to be centrality dependent, but as figure 3.20 indicates, no clear dependence on centrality or transverse momentum can be identified. However, one trend can be observed: the deviation, higher at backward rapidity than at forward rapidity, decreases for increasing centralities until the calculated results of all rapidity bins display similar differences.

The results of both methods for elliptic flow for the $0-10\,\%$ centrality class are rebinned by a factor of 2 to increase the significance. For more central events ($\mathcal{C} > 10\,\%$) the fluctuations decrease and come closer to the MC true values but are still higher, as can be seen in the bottom right figure of 3.23.

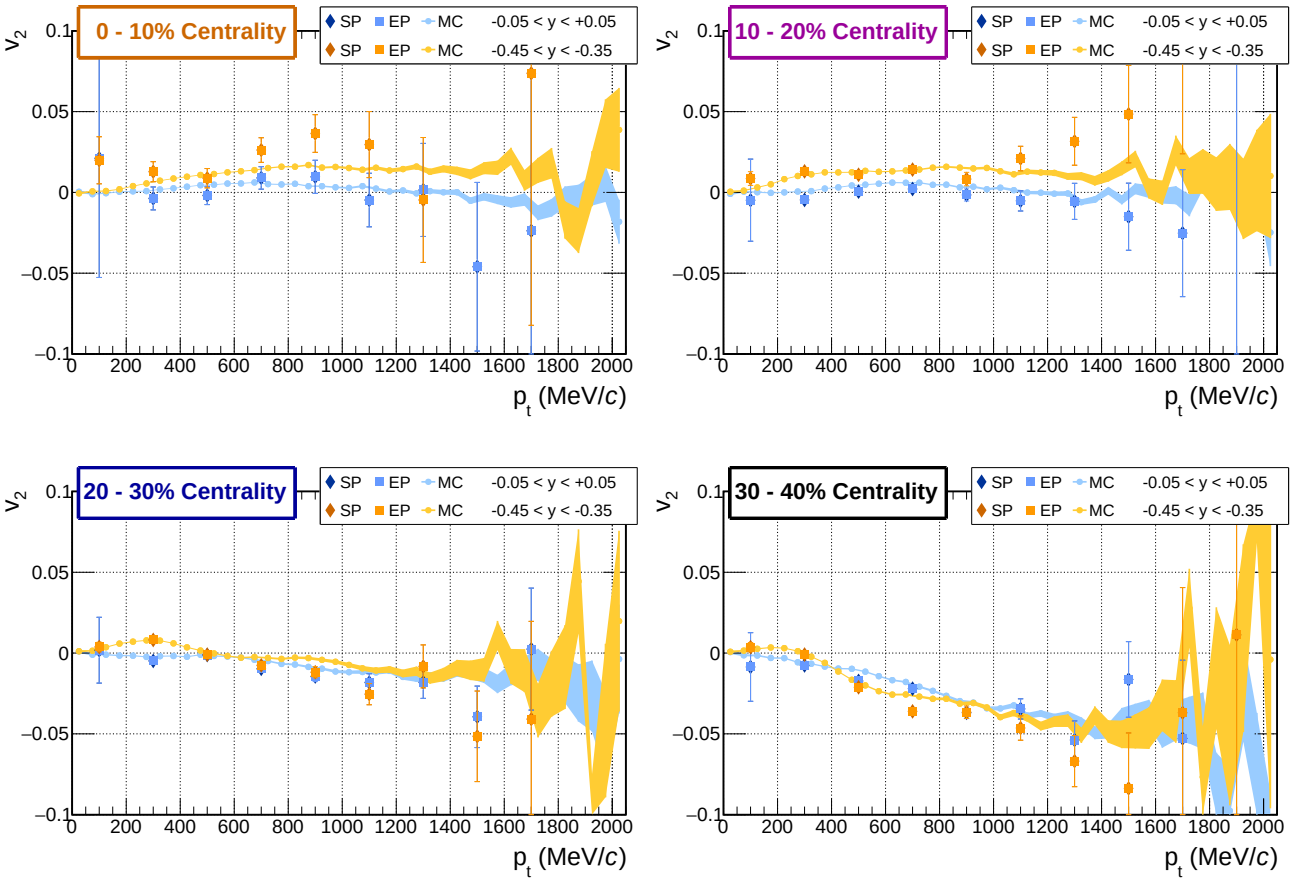

Figure 3.23: $v_2\{EPM\}$ and $v_2\{SPM\}$ versus p_t of MC simulated Au+Au events.

A systematic error has to be taken into account for the analysis of experimental data, as the calculated flow values using particles that passed the reconstruction procedure and the reconstructed EP differs from the flow values calculated with the MC set.

3.8. Analysis of experimental data

After comparing both methods by means of simulations, now experimental data is taken: Au+Au events at 1.23 AGeV measured in April 2012. The resolution values (R_1 and R_2) of experimental data are significantly higher than for simulations and decrease towards peripheral events. Also the efficiency correction is applied.

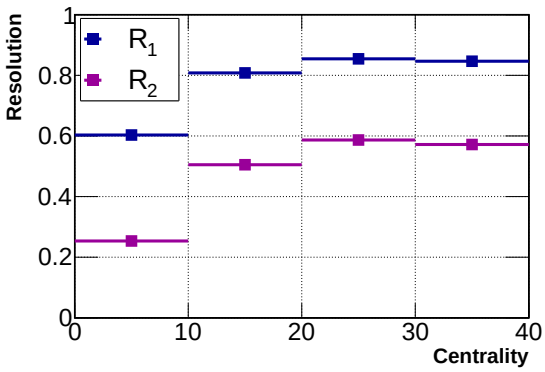

Figure 3.24: R_1 and R_2 of the analysis methods of the four analysed centrality classes.

3.8.1. Directed flow

The results for experimental data are presented in a similar manner as realised in figure 3.22.

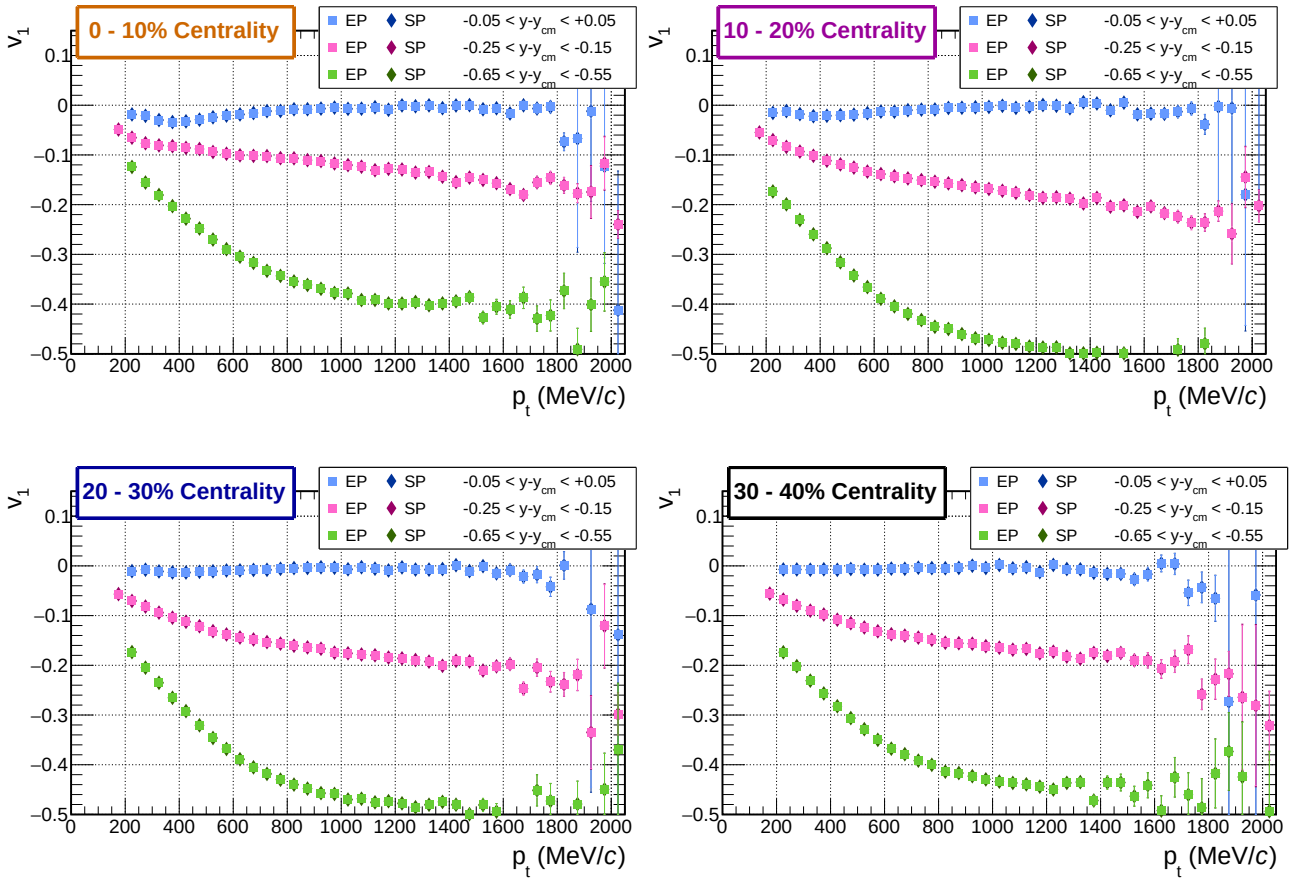

Figure 3.25: Experimental data: $v_1\{EPM\}$ and $v_1\{SPM\}$ versus p_t in three y bins.

Both methods result in the same flow coefficients as the squares – representing results of the EPM – are lying exactly on the diamonds, representing findings of the SPM. The flow coefficients at mid rapidity are represented by blue symbols in figure 3.25. Across all centrality classes, the slightly negative values are located very close to the zero line. Directed flow crosses zero at mid rapidity. Hence, the calculated values seem to be appropriate within the systematic error.
In figure 3.26 three exemplary bins of 50 MeV/c p_t width are chosen. The ending of the $(250 - 300)$ MeV/c data points (turquoise) at $y_{cm} = 0.2$ is explained by the finite phase space coverage of the HADES detector system, see figure 3.5. Just as in figure 3.25, no deviations between EPM and SPM are apparent.

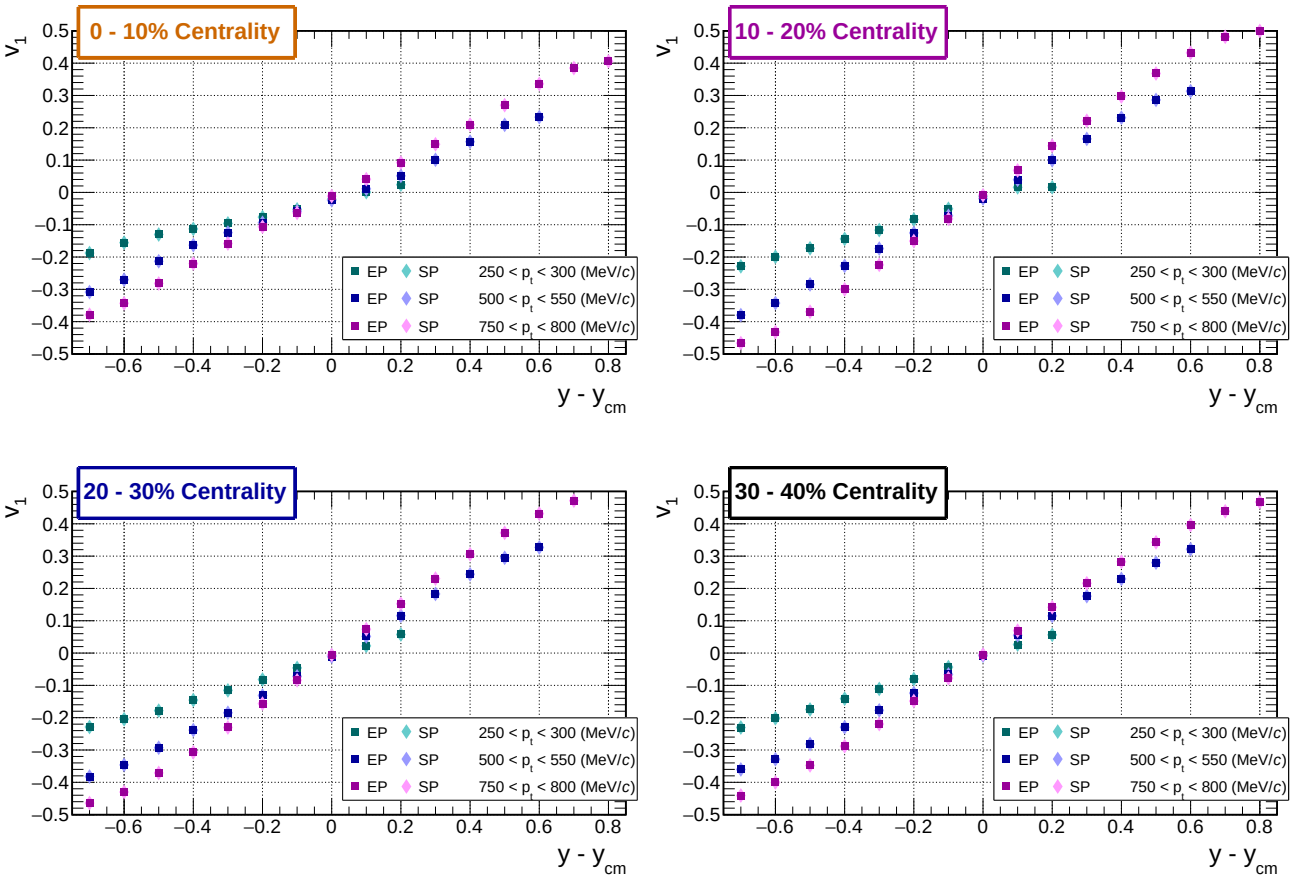

Figure 3.26: Experimental data: $v_1\{EPM\}$ and $v_1\{SPM\}$ versus y in three p_t bins.

The positive slope of the p_t bins near mid rapidity of about 0.5 is reasonable since $\mathrm{d}v_1/\mathrm{d}y$ of protons is positive until $\sqrt{s_{AuAu}} \approx 15$ GeV is reached and the experimental data taken in April 2012 (Au+Au collision at 1.23 AGeV) corresponds to $\sqrt{s_{AuAu}} = 2.4$ GeV [90][1] [91].
Considering the two figures, both methods are leading to the same directed flow results over the entire phase space.

[1]It should be mentioned that a p_t range of $(400-2000)$ MeV/c and centrality range of $10-40$ % is used there.

3.8.2. Elliptic flow

As elliptic flow is less pronounced compared to directed flow a narrower y-axis range is used in figure 3.27. Just like directed flow, $v_2\{EPM\}$ and $v_2\{SPM\}$ are equal in the two shown rapidity bins.

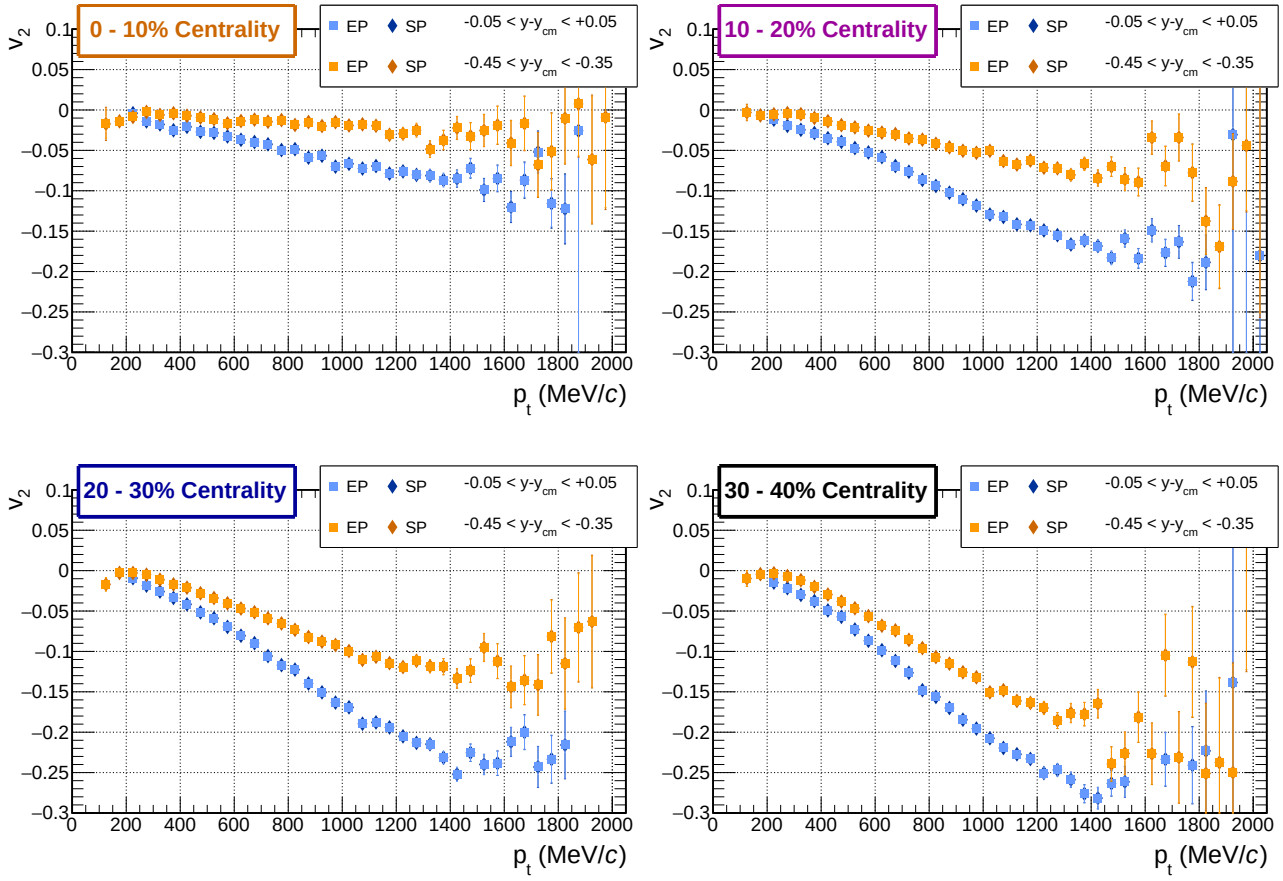

Figure 3.27: Experimental data: $v_2\{EPM\}$ and $v_2\{SPM\}$ versus p_t in two y bins.

An increasing maximum value of the flow coefficients of each y-bin can be observed for decreasing centrality. This trend is based on the fact that elliptic flow has its maximum at mid-central events, see section 1.3.

No differences between the calculated flow values appear in figure 3.28, where three exemplary p_t bins of $v_2\{EP\}$ and $v_2\{SP\}$ versus rapidity are shown.

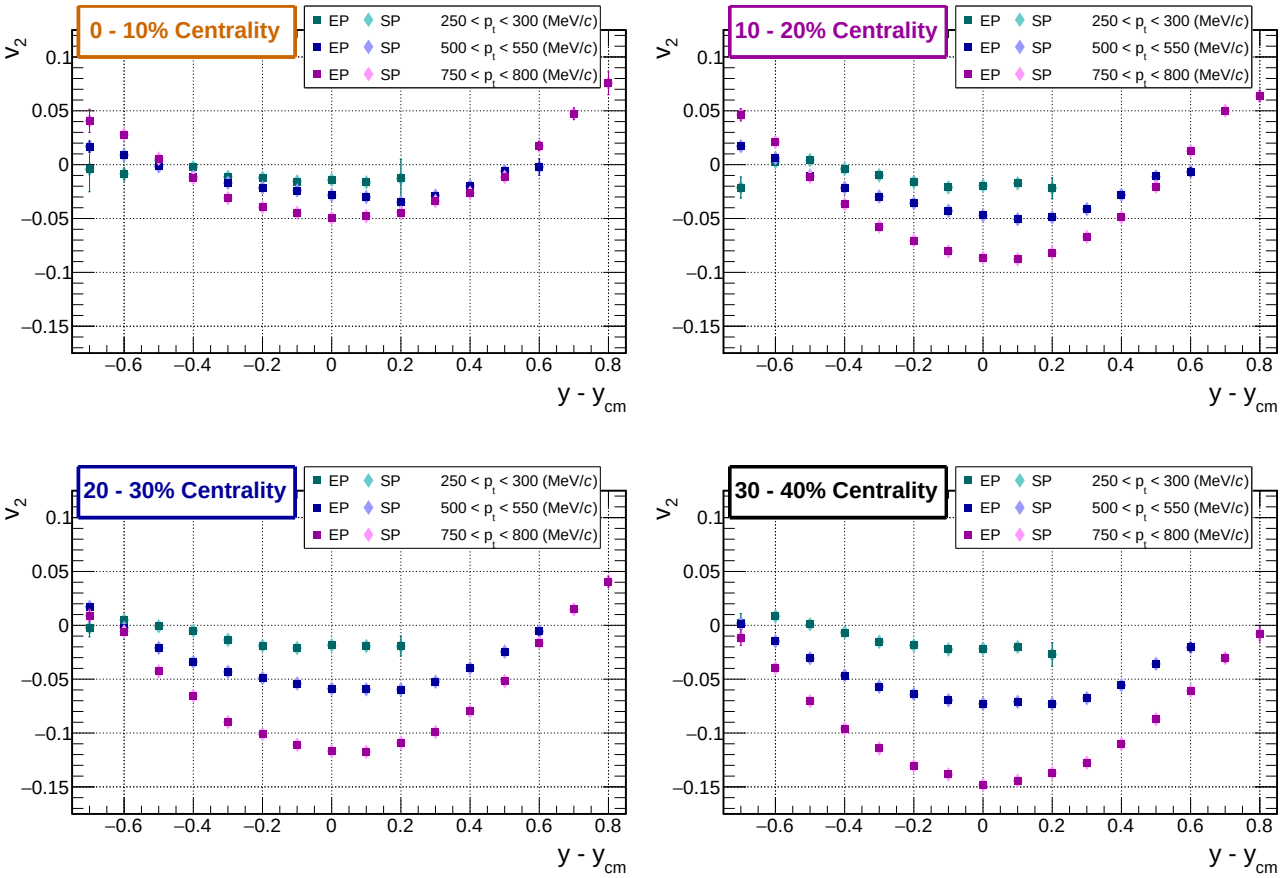

Figure 3.28: Experimental data: $v_2\{EPM\}$ and $v_2\{SPM\}$ versus y in three p_t bins.

The methods result in equal flow values for elliptic flow inside the accessible transverse momentum and rapidity phase space of the HADES setup.

4. Conclusion and outlook

The two analysis algorithms, the standard Event Plane method and the Scalar Product method, have been validated using Monte Carlo simulations of anisotropic flow of protons. Both methods yield identical coefficients of directed and elliptic flow but are affected by the Event Plane (EP) reconstruction.

The absolute differences Δv_1 and Δv_2 between the results calculated using the MC Reaction Plane angle and the reconstructed Event Plane angle show a rapidity dependence, see table 3.

Flow coefficient	$\mathcal{C}$[%]	$(y - y_{cm}) < 0$	$(y - y_{cm}) > 0$
v_1	$0 - 40$	$0.02 < \lvert\Delta v_1(y, p_t)\rvert < 0.05$ (y, p_t)-dependent	$\lvert\Delta v_1\rvert \leq 0.02$ almost constant
v_2	$10 - 40$	$\lvert\Delta v_2\rvert \leq 0.02$ almost constant	$0.02 < \lvert\Delta v_2(y, p_t)\rvert < 0.04$ (y, p_t)-dependent

Table 3: Comparison of the values of Δv_1 and Δv_2 within the rapidity hemispheres.

Additionally, Δv_1 seems to be centrality dependent whereas no significant trend can be observed for Δv_2. Moreover, the slope of the applied linear fit functions, as discussed in section 3.7.1, can give an indication of a transverse momentum dependence for different rapidity bins of several centrality classes.

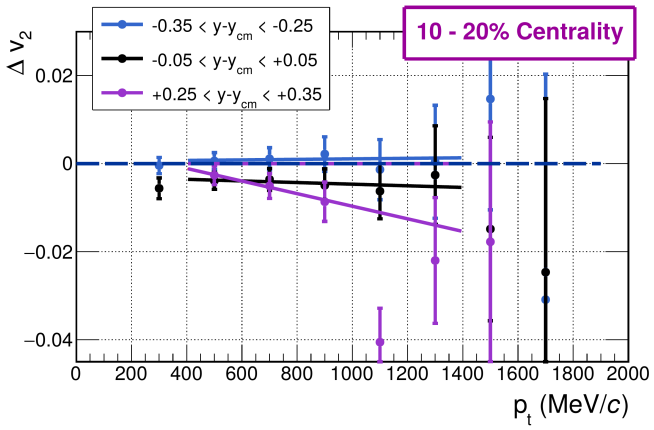

Figure 4.1: Δv_2 of 10–20 % most central events of three exemplary rapidity bins with linear fit functions covering a p_t-range of $(400-1400)\,\mathrm{MeV}/c$ (backward and mid rapidity). At mid rapidity, Δv_2 is almost constant (≈ 0.005). The fit function of the forward rapidity bin covers a p_t-range of $(400-1000)\,\mathrm{MeV}/c$ as the Δv_2-value at $1100\,\mathrm{MeV}/c$ is assumed to be a statistical outlier. The Δv_2-value at $1300\,\mathrm{MeV}/c$ (under consideration of its statistical error) can be described by the linear fit function as well.

Assuming the reconstruction procedure influences the analysis of data in the same manner, the respective Δv_n is included hereinafter as a systematic uncertainty.

Following the validation procedure with MC simulations, experimental data of Au+Au collisions at 1.23 AGeV recorded with HADES have been analysed. An application of the efficiency

correction improved the results of the calculated flow coefficients. The uncorrected values of $v_1\{SPM\}$ versus p_t are shown on the left side of figure 4.2, on the right side the corrected ones.

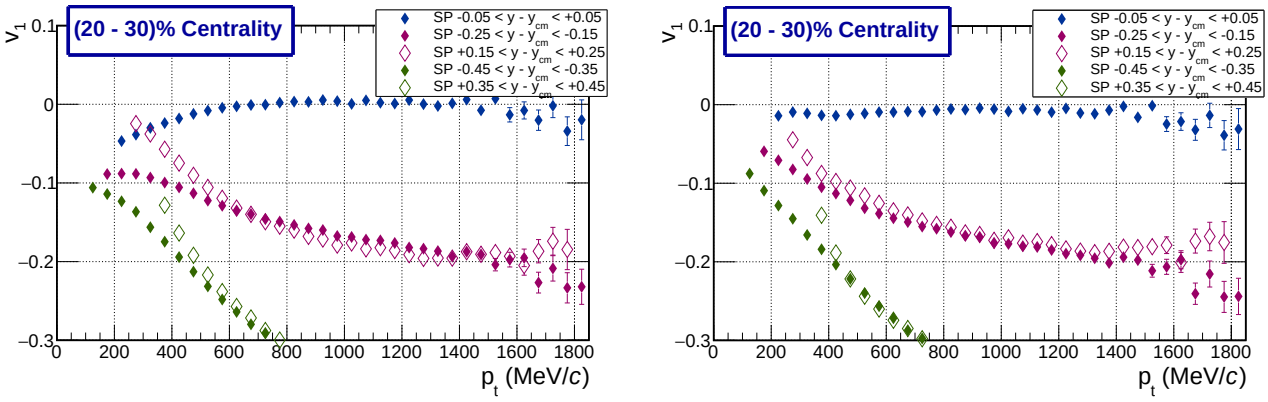

Figure 4.2: $v_1\{SPM\}$ versus p_t for 20 – 30 % most central events. Flow coefficients in forward rapidity bins (open symbols) are multiplied with -1 to enable a comparison. Left side: before applying the efficiency correction. Right side: with applied efficiency correction.

As the collision system (Au+Au) is symmetric, the particle distribution in the backward hemisphere of the centre-of-mass should be equal to the distribution in the forward hemisphere. Thus, the absolute value of v_1 at forward rapidity should be of the same size as the value at backward rapidity. After applying the efficiency correction, the magnitude of the backward rapidity v_1 (full symbols) is more alike the ones of the forward rapidity (open symbols, multiplied with -1). An improvement of v_1 at mid rapidity can also be observed as the corrected ones are located closer to zero and the directed flow should be zero at mid rapidity.

The re-centering procedure was applied in order to reduce acceptance correlations of an imperfect detector or the influence of malfunctioning detector elements by making the event plane angle distribution isotropic in the laboratory system [24]. Using the re-centering procedure of [28] led to an improvement of the event plane angle distributions of all centrality classes. The calculated flow values with and without re-centering correction differ only slightly (less than 0.05) across a wide range of the covered phase space of protons.

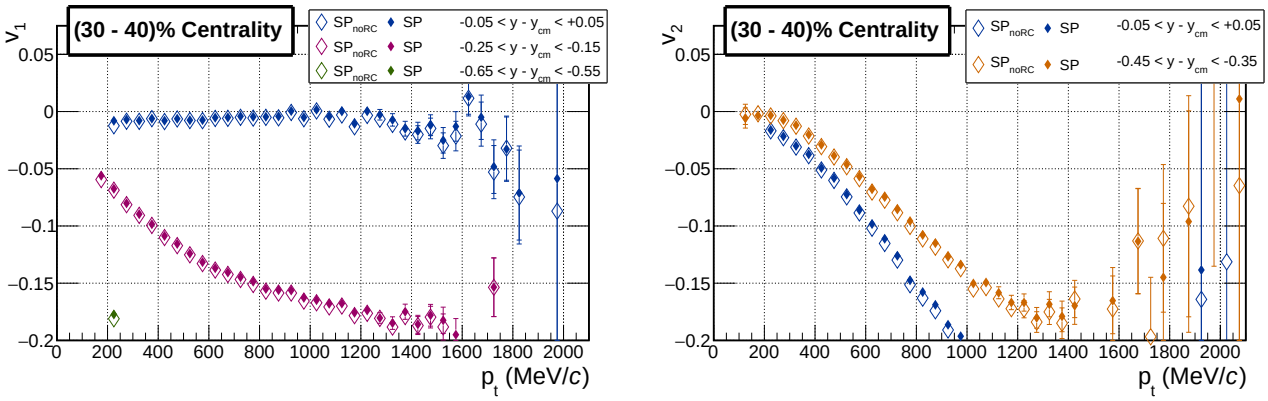

Figure 4.3: $v_1\{SPM\}$ (left panel) and $v_2\{SPM\}$ (right panel) versus p_t for 30 – 40 % most central events. The difference between the corrected (open symbols) and uncorrected (full symbols) flow coefficients is small even though the degree of the re-centering correction is at its maximum for this centrality class as described in section 3.4.

The results of both analysis methods for experimental data are in agreement with [92] (analysing Au+Au at 1.2 AGeV) as the positive slope of $\mathrm{d}v_1/\mathrm{d}y$ of protons near mid rapidity is of comparable size. Furthermore, the elliptic flow coefficients of this thesis are in good agreement with world data (also under consideration of systematics) [46, 49, 93], see table 4 and figure 4.4.

$\mathcal{C}$ [%]	v_2	σ_{stat}	σ_{sys}
$0-10$	-0.04	0.002	0.009
$10-20$	-0.06	0.001	0.005
$20-30$	-0.07	0.001	0.003
$30-40$	-0.08	0.001	0.006

Table 4: v_2 of all centrality classes with σ_{stat} and σ_{sys} (using equation (4.1) and equation (4.2)) at mid rapidity integrated over the transverse momentum range between 300 MeV and 1400 MeV.

Figure 4.4 shows world data and the v_2 value (green point) of the analysed HADES data.

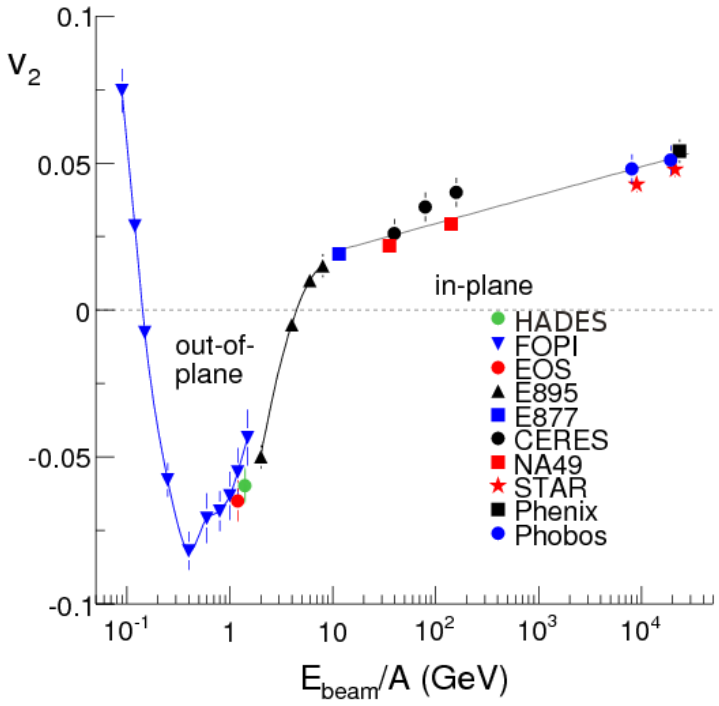

Figure 4.4: Beam energy dependence of elliptic flow measurements at mid rapidity for $20-30\,\%$ most central events covering five orders of magnitude [49]. Both analysis methods result in a value of $v_2 = -0.060 \pm 0.001\,(\sigma_{stat}) \pm 0.005\,(\sigma_{sys})$ for elliptic flow at mid rapidity for $10-20\,\%$ most central events in a p_t range of $300\,\mathrm{MeV}/c \leq p_t \leq 1400\,\mathrm{MeV}/c$ (green point).

The flow coefficient v_2 and the statistical error σ_{stat} are the weighted sums of the individual values of each p_t bin at mid rapidity across the defined p_t range, using the measured proton multiplicity N of each bin as a weight.

$$v_2(y) = \frac{\sum_{p_t=300\,\mathrm{MeV}/c}^{1400\,\mathrm{MeV}/c} v_2(y)\cdot N(y)}{\sum_{p_t=300\,\mathrm{MeV}/c}^{1400\,\mathrm{MeV}/c} N(y)} \qquad \sigma_{stat}(y) = \frac{\sum_{p_t=300\,\mathrm{MeV}/c}^{1400\,\mathrm{MeV}/c} \sigma(y)\cdot N(y)}{\sum_{p_t=300\,\mathrm{MeV}/c}^{1400\,\mathrm{MeV}/c} N(y)} \tag{4.1}$$

The systematic error σ_{sys} is the weighted sum of the absolute difference Δv_2, using the multiplicity of MC generated protons N_{MC} of each p_t-bin at Cumulant.

$$\sigma_{sys}(y) = \frac{\sum_{p_t=300\,\mathrm{MeV}/c}^{1400\,\mathrm{MeV}/c} \Delta v_2(y) \cdot N_{MC}(y)}{\sum_{p_t=300\,\mathrm{MeV}/c}^{1400\,\mathrm{MeV}/c} N_{MC}(y)} \tag{4.2}$$

A further implementation of the Scalar Product Method based on equation (4.3) is of interest for various reasons.

$$v_n\{SPM\} = \frac{\left\langle \left\langle \boldsymbol{u}_i\,(p_t, y) \cdot \dfrac{\boldsymbol{Q}_n}{M_n} \right\rangle_p \right\rangle_e}{\sqrt{\left\langle \dfrac{\boldsymbol{Q}_{n,A}}{M_{n,A}} \cdot \dfrac{\boldsymbol{Q}_{n,B}}{M_{n,B}} \right\rangle_e}} \quad . \tag{4.3}$$

Previously, it should be mentioned that the presented SPM flow values are obviously identical to the flow values calculated with the EPM as the used particle momentum vectors ($\boldsymbol{u}_i$) and the event $\boldsymbol{Q}$-vectors are normalised. Since the rapidity gap between the participating protons ($\boldsymbol{u}_i$, measured with the MDCs) and the spectators ($\boldsymbol{Q}$, measured at small θ with the FW) is large, short range correlations (*non-flow*) are implicitly avoided.

Initially, participating protons are used in equation (3.29) to create the $\boldsymbol{Q}$-vectors of the SPM. As the number of the measured protons is higher compared to the number of spectators measured with the FW, the statistical error of the resulting flow coefficients is assumed to be slightly smaller than the results of the EPM [24]. Also an explicit EP estimation and the calculation of the EP resolution (R_n) using the Ollitraut procedure becomes redundant. The SPM correlates the POI ($\boldsymbol{u}_i$) with all other participating particles of an event and is therefore independent from an EP and its resolution. This makes the SPM more independent from the detector and enables a comparison between experiments [94, 95].

However, using participants to create the $\boldsymbol{Q}$-vectors introduces non-flow effects and autocorrelations. Non-flow effects are assumed to occur between particles of almost the same rapidity. Therefore, rapidity gaps between the POI and the remaining protons as well as gaps between the set of protons creating the $\boldsymbol{Q}$-vectors have to be realised.

Autocorrelations that distort the calculation of the flow coefficients significantly can be prevented by subtracting the POI from all measured protons of the event.

As the SPM correlates participants to each other, the flow values are measured in the the Participant Plane (PP) coordinate system. Therefore, the SPM is less sensitive to *flow fluctuations* compared to the EPM and corresponds to the root-mean-square $\langle v_n^2 \rangle^{1/2}$, whereas the EPM complies with $\langle v_n^\alpha \rangle^{1/\alpha}$ with $\alpha \in [1, 2[$ [89]. Besides this, the calculated flow coefficients are supposed to be higher compared to the results of the EPM as the particle momentum vectors are correlated to the PP instead of the RP or rather EP (p.p.8). The PP describes the initial orientation of the overlap almond more precisely, thus, the angle between u_i and the PP is always smaller compared to the angular difference between $\boldsymbol{u}_i$ and the RP [24, 89].

As the SPM estimates the flow coefficients by correlating two vectors, $\boldsymbol{u}_i$ and the $\boldsymbol{Q}$-vector, the results are more alike the results of a two-particle method. Therefore, the received results of the SPM ought to be compared to a two-particle correlation method as such as Q-Cumulant Method [96, 97] or a all-particle correlation method as like the Lee-Yang Zeroes [98, 99].

Appendices

A. Track multiplicity of MC simulations

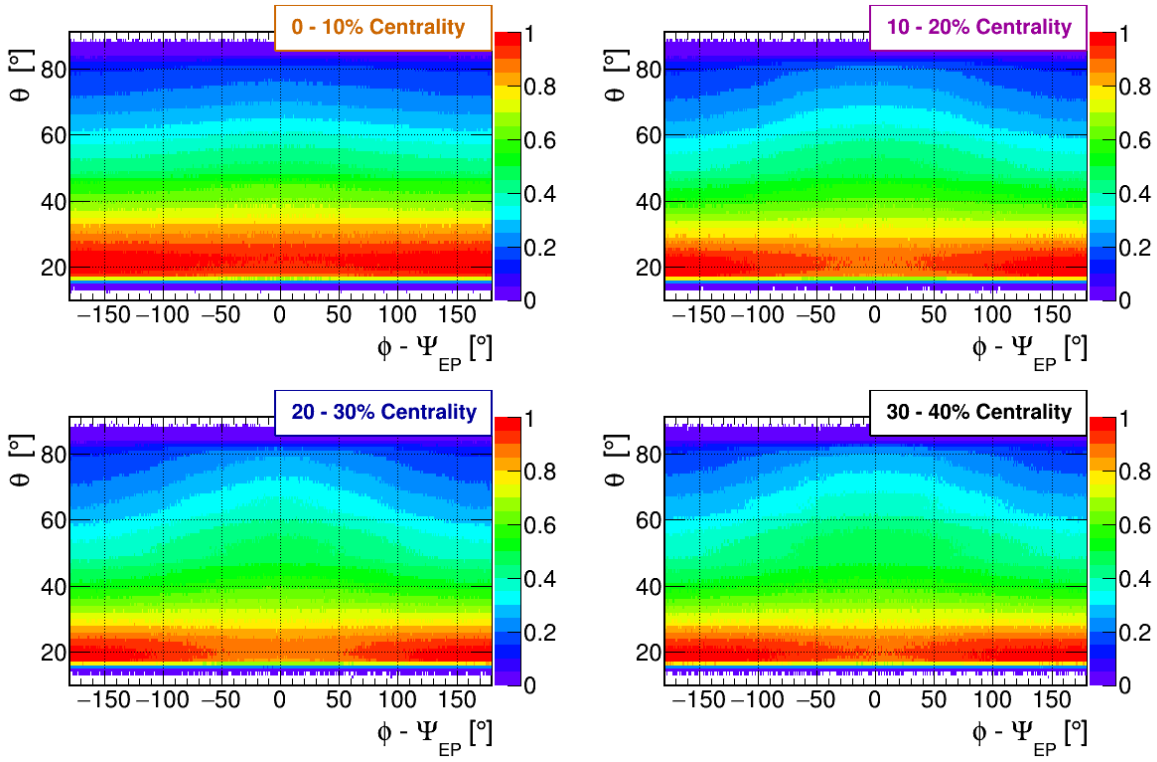

Figure .5: Track multiplicity of MC simulations as a function of Φ and θ of each centrality class. Each distribution of selected tracks is normalized to the value of its highest multiplicity.

As the track multiplicity of MC simulations differs drom the track multiplicity of experimental data, another efficiency matrix must be calculated. The analysed harmonics, directed and elliptic flow, are less pronounced in UrQMD based MC simulations as in experimental data. Therefore, the protons are distributed differently.

B. Exact values of the event plane resolutions

MC simulations

Centrality [%]	R_1 [%]	R_2 [%]
0 – 10	20.76	2.77
10 – 20	38.18	9.59
20 – 30	46.55	14.50
30 – 40	49.46	16.49

Experimental data

Centrality [%]	R_1 [%]	R_2 [%]
0 – 10	60.34	25.38
10 – 20	80.82	50.55
20 – 30	85.46	58.58
30 – 40	84.67	57.21

Table 5: Exact values of the resolutions R_1 and R_2 of the four centrality classes of MC simulations, shown in figure 3.17 and of experimental data, shown in figure 3.24.

C. Two dimensional representation of Δv_n

Following figures show the absolute differences Δv_1 and Δv_2 of the accessible p_t and y phase space of protons. The one dimensional representations of the figures 3.20 and 3.21 of section 3.7.1 are realised via extracting individual rapidity bins.

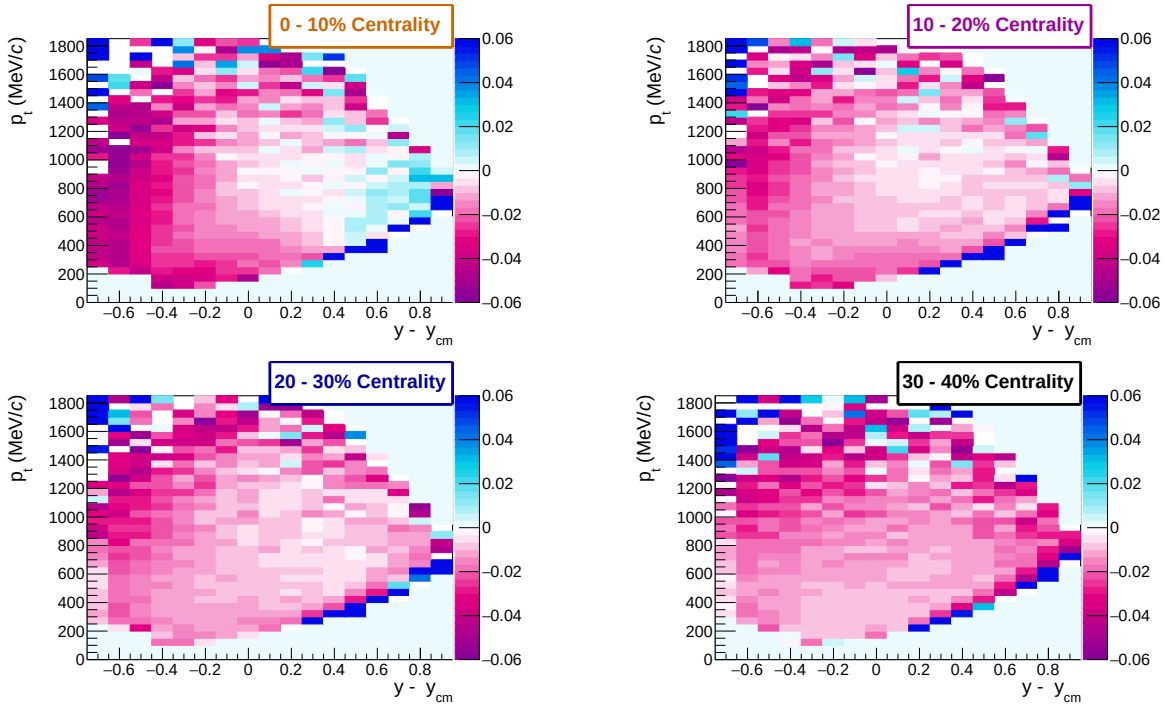

Figure .6: Δv_1 between the calculated flow coefficients using the reconstructed and the MC set.

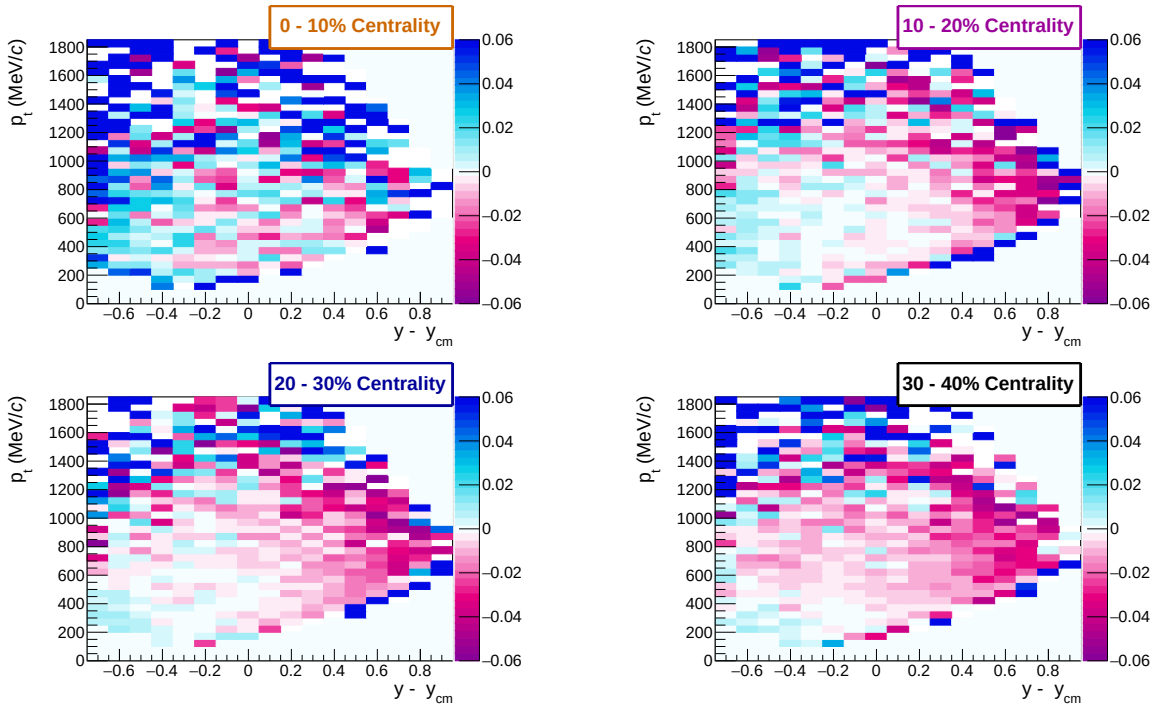

Figure .7: Δv_2 between the calculated flow coefficients using the reconstructed and the MC set.

p_t in MeV/c		400 – 500		1300 – 1400	
Rapidity	$\mathcal{C}$ [%]	$v_1\{EPM\}$	Δv_1	$v_1\{EPM\}$	Δv_1
$-0.35 <$	0 – 10	-0.082	-0.019 ± 0.002	-0.146	-0.025 ± 0.004
	10 – 20	-0.098	-0.012 ± 0.002	-0.159	-0.015 ± 0.003
$y - y_{cm}$	20 – 30	-0.089	-0.011 ± 0.002	-0.146	-0.02 ± 0.003
< -0.25	30 – 40	-0.063	-0.01 ± 0.002	-0.127	-0.024 ± 0.004
$-0.05 <$	0 – 10	-0.018	-0.013 ± 0.002	-0.018	-0.002 ± 0.004
	10 – 20	-0.014	-0.01 ± 0.002	-0.014	-0.002 ± 0.003
$y - y_{cm}$	20 – 30	-0.013	-0.009 ± 0.002	-0.007	-0.008 ± 0.003
$< +0.05$	30 – 40	-0.008	-0.009 ± 0.002	-0.003	-0.018 ± 0.003
$+0.25 <$	0 – 10	0.051	-0.006 ± 0.003	0.1	-0.003 ± 0.005
	10 – 20	0.074	-0.01 ± 0.002	0.133	-0.002 ± 0.003
$y - y_{cm}$	20 – 30	0.068	-0.008 ± 0.002	0.103	-0.004 ± 0.003
$< +0.35$	30 – 40	0.045	-0.01 ± 0.002	0.093	-0.015 ± 0.004

p_t in MeV/c		400 – 600		1200 – 1400	
Rapidity	$\mathcal{C}$ [%]	$v_2\{EPM\}$	Δv_2	$v_2\{EPM\}$	Δv_2
$-0.35 <$	0 – 10	0.002	0.012 ± 0.018	0.009	0.006 ± 0.031
	10 – 20	0.000	0.001 ± 0.006	0.004	0.001 ± 0.011
$y - y_{cm}$	20 – 30	-0.023	-0.002 ± 0.005	-0.027	-0.001 ± 0.009
< -0.25	30 – 40	-0.050	-0.004 ± 0.006	-0.06	-0.016 ± 0.010
$-0.05 <$	0 – 10	0.008	-0.004 ± 0.017	0.002	0.008 ± 0.029
	10 – 20	-0.009	-0.004 ± 0.006	-0.006	-0.005 ± 0.011
$y - y_{cm}$	20 – 30	-0.011	-0.000 ± 0.005	-0.018	-0.011 ± 0.009
$< +0.05$	30 – 40	-0.047	-0.005 ± 0.006	-0.054	-0.002 ± 0.010
$+0.25 <$	0 – 10	0.054	-0.002 ± 0.021	0.032	0.005 ± 0.036
	10 – 20	-0.011	-0.001 ± 0.007	-0.018	-0.027 ± 0.013
$y - y_{cm}$	20 – 30	-0.026	-0.007 ± 0.006	-0.030	-0.018 ± 0.010
$< +0.35$	30 – 40	-0.075	-0.01 ± 0.007	-0.076	-0.025 ± 0.012

Table 6: Selected values of v_1 and v_2 with absolute differences Δv_n in three rapidity bins. The corresponding Δv_n values are calculated using the parameters of the linear fit functions applied to the absolute difference, covering a transverse momentum range between 400 MeV and 1400 MeV. The values of v_1 and v_2 are sums along the momentum range, weighted with the track multiplicity of each bin.

List of Figures

List of Tables

References

[1] Adam G. Riess, Alexei V. Filippenko, Peter Challis, Alejandro Clocchiatti, Alan Diercks, Peter M. Garnavich, Ron L. Gilliland, Craig J. Hogan, Saurabh Jha, Robert P. Kirshner, et al. Observational evidence from supernovae for an accelerating universe and a cosmological constant. *The Astronomical Journal*, 116(3):1009, 1998.

[2] Valery A. Rubakov. Introduction to cosmology. *Proceedings of Science*, page 004, 2005.

[3] D.S. Gorbunov and V.A. Rubakov. *Introduction to the Theory of the Early Universe – Hot Big Bang Therory*. World Scientific, New Jersey, 2011.

[4] J. Richard Gott III, Mario Jurić, David Schlegel, Fiona Hoyle, Michael Vogeley, Max Tegmark, Neta Bahcall, and Jon Brinkmann. A map of the universe. *The Astrophysical Journal*, 624(2):463, 2005.

[5] Ruth Durrer. The cosmic microwave background: the history of its experimental investigation and its significance for cosmology. *Classical and Quantum Gravity*, 32(12):124007, 2015.

[6] David N. Schramm and Michael S. Turner. Big-Bang Nucleosynthesis enters the precision era. *Reviews of Modern Physics*, 70(1):303, 1998.

[7] David W. Hogg. Distance measures in cosmology. *arXiv preprint astro-ph/9905116*, 1999.

[8] Thibaut Josset, Alejandro Perez, and Daniel Sudarsky. Dark energy from violation of energy conservation. *Physical Review Letters*, 118(2):021102, 2017.

[9] Eric V. Linder. Exploring the expansion history of the universe. *Physical Review Letters*, 90(9):091301, 2003.

[10] Julien Lesgourgues, Gianpiero Mangano, Gennaro Miele, and Sergio Pastor. *Neutrino cosmology*. Cambridge University Press, 2013.

[11] Julien Lesgourgues and Sergio Pastor. Massive neutrinos and cosmology. *Physics Reports*, 429(6):307–379, 2006.

[12] P. Peter and J.P. Uzan. Cosmologie primordiale (Berlin, Paris, 2005), 2009.

[13] `https://en.wikipedia.org/wiki/Standard_Model`, Jul 2017.

[14] Roel Aaij, B. Adeva, M. Adinolfi, A. Affolder, Z. Ajaltouni, S. Akar, J. Albrecht, F. Alessio, M. Alexander, S. Ali, et al. Observation of $j/\psi\, p$ resonances consistent with pentaquark states in $\lambda_b^0 \to j/\psi\, k^-\, p$ decays. *Physical review letters*, 115(7):072001, 2015.

[15] P.W. Higgs. Broken symmetries and the masses of gauge bosons. *Physical Review Letters*, 13(16):508, 1964.

[16] G. Aad, B. Abbott, J. Abdallah, O. Abdinov, R. Aben, M. Abolins, O.S. AbouZeid, H. Abramowicz, H. Abreu, R. Abreu, et al. Combined measurement of the higgs boson mass in pp collisions at $\sqrt{s} = 7$ and 8 TeV with the ATLAS and CMS experiments. *Physical review letters*, 114(19):191803, 2015.

[17] R. Brent Tully, Helene Courtois, Yehuda Hoffman, and Daniel Pomarède. The Laniakea supercluster of galaxies. *arXiv preprint arXiv:1409.0880*, 2014.

[18] Dale A. Ostlie and Bradley W. Carroll. *An introduction to modern astrophysics*. Addison-Wesley, 2007.

[19] J. Cleymans, H. Oeschler, K. Redlich, and S. Wheaton. Comparison of chemical freeze-out criteria in heavy-ion collisions. *Physical Review C*, 73(3):034905, 2006.

[20] B. Friman, F. Karsch, K. Redlich, and V. Skokov. Fluctuations as probe of the QCD phase transition and freeze-out in heavy ion collisions at LHC and RHIC. *The European Physical Journal C-Particles and Fields*, 71(7):1–11, 2011.

[21] `https://madai-public.cs.unc.edu/visualization/heavy-ion-collisions/low-energy/`, Aug 2017.

[22] S.A. Bass, M. Belkacem, M. Bleicher, M. Brandstetter, L. Bravina, C. Ernst, L. Gerland, M. Hofmann, S. Hofmann, J. Konopka, et al. Microscopic models for ultrarelativistic heavy ion collisions. *Progress in Particle and Nuclear Physics*, 41:255–369, 1998.

[23] `http://urqmd.org/`, Aug 2014.

[24] Sergei A. Voloshin. Collective phenomena in non-central nuclear collisions. In *Relativistic Heavy Ion Physics*, pages 293–333. 2002.

[25] S.A. Voloshin, A.M. Poskanzer, and R. Snellings. Anisotropic flow from AGS to RHIC. *arXiv preprint nucl-th/0202072*, 2010.

[26] `https://cds.cern.ch/record/1695331/plots`, Jul 2017.

[27] M.L. Miller, K. Reygers, S.J. Sanders, and P. Steinberg. Glauber modeling in high-energy nuclear collisions. *Annu. Rev. Nucl. Part. Sci.*, 57:205–243, 2007.

[28] Arthur M. Poskanzer and Sergei A. Voloshin. Methods for analyzing anisotropic flow in relativistic nuclear collisions. *Physical Review C*, 58(3):1671, 1998.

[29] Henning Heiselberg and Anne-Marie Levy. Elliptic flow and hanbury-brown–twiss correlations in noncentral nuclear collisions. *Physical Review C*, 59(5):2716, 1999.

[30] N. van der Kolk. *To flow or not to flow: A study of elliptic flow and nonflow in proton-proton collisions in ALICE*. Utrecht University, 2012.

[31] G. Buchwald, G. Graebner, J. Theis, J. Maruhn, W. Greiner, et al. Kinetic energy flow in Nb (400 MeV/A) + Nb: evidence for hydrodynamic compression of nuclear matter. *Phys.Rev.Lett.*, 52:1594–1596, 1984.

[32] J.-Y. Ollitrault. Anisotropy as a signature of transverse collective flow. *Physical Review D*, 46(1):229, 1992.

[33] A. Andronic, W. Reisdorf, N. Herrmann, P. Crochet, J.P. Alard, V. Barret, Z. Basrak, N. Bastid, G. Berek, R. Čaplar, et al. Directed flow in Au + Au, Xe^+ CsI, and Ni + Ni collisions and the nuclear equation of state. *Physical Review C*, 67(3):034907, 2003.

[34] C. Fuchs, A. Faessler, S. El-Basaouny, K. Shekhter, E.E. Zabrodin, and Y.M. Zheng. The nuclear equation of state probed by K+ production in heavy ion collisions. *Journal of Physics G: Nuclear and Particle Physics*, 28(7):1615, 2002.

[35] C. Fuchs, A. Faessler, E. Zabrodin, and Y.M. Zheng. Probing the nuclear equation of state by K+ production in heavy-ion collisions. *Physical Review Letters*, 86(10):1974, 2001.

[36] Paul Demorest, Tim Pennucci, Scott Ransom, Mallory Roberts, and Jason Hessels. Shapiro delay measurement of a two solar mass neutron star. *arXiv preprint arXiv:1010.5788*, 2010.

[37] M. Hempel, T. Fischer, J. Schaffner-Bielich, and M. Liebendörfer. New equations of state in simulations of core-collapse supernovae. *The Astrophysical Journal*, 748(1):70, 2012.

[38] A.W. Steiner, J.M. Lattimer, and E.F. Brown. The equation of state from observed masses and radii of neutron stars. *The Astrophysical Journal*, 722(1):33, 2010.

[39] J.M Lattimer and M. Prakash. Neutron star observations: Prognosis for equation of state constraints. *Physics reports*, 442(1):109–165, 2007.

[40] C. Pinkenburg, N.N. Ajitanand, J.M. Alexander, M. Anderson, D. Best, F.P. Brady, T. Case, W. Caskey, D. Cebra, J.L. Chance, et al. Elliptic flow: Transition from out-of-plane to in-plane emission in Au+Au collisions. *Physical Review Letters*, 83(7):1295.

[41] P. Danielewicz, E895 Collaboration, et al. Differential Elliptic Flow in $2-6$ AGeV Au+Au Collisions: A New Constraint for the Nuclear Equation of State. *arXiv preprint nucl-ex/0112002*, 2001.

[42] John Adams, M.M. Aggarwal, Z. Ahammed, J. Amonett, B.D. Anderson, D. Arkhipkin, G.S. Averichev, S.K. Badyal, Y. Bai, J. Balewski, et al. Azimuthal anisotropy in Au+Au collisions at $\sqrt{s_{NN}} = 200$ gev. *Physical Review C*, 72(1):014904, 2005.

[43] Steven Manly, B.B. Back, M.D. Baker, D.S. Barton, R.R. Betts, R. Bindel, A. Budzanowski, W. Busza, A. Carroll, M.P. Decowski, et al. Flow and bose-einstein correlations in Au-Au collisions at RHIC. *Nuclear Physics A*, 715:611c–614c, 2003.

[44] J. Slívová, CERES/NA45 Collaboration, et al. Flow and non-flow event anisotropies at the SPS. *Nuclear Physics A*, 715:615c–618c, 2003.

[45] C. Alt, T. Anticic, B. Baatar, D. Barna, J. Bartke, M. Behler, L. Betev, H. Białkowska, A. Billmeier, C. Blume, et al. Directed and elliptic flow of charged pions and protons in Pb+Pb collisions at 40 and 158 AGeV. *Physical Review C*, 68(3):034903, 2003.

[46] A. Andronic, V. Barret, Z. Basrak, N. Bastid, L. Benabderrahmane, G. Berek, Roman Čaplar, E. Cordier, P. Crochet, P. Dupieux, et al. Excitation function of elliptic flow in Au+Au collisions and the nuclear matter equation of state. *Physics Letters B*, 612(3): 173–180, 2005.

[47] J. Barrette, R. Bellwied, S. Bennett, P. Braun-Munzinger, W.E. Cleland, M. Clemen, J. Cole, T.M. Cormier, G. David, J. Dee, et al. Observation of anisotropic event shapes and transverse flow in ultrarelativistic Au+Au collisions. *Physical Review Letters*, 73(19): 2532, 1994.

[48] J. Barrette, R. Bellwied, S. Bennett, P. Braun-Munzinger, W.C. Chang, W.E. Cleland, M. Clemen, J. Cole, T.M. Cormier, G. David, et al. Energy and charged particle flow in 10.8 AGeV/c Au+Au collisions. *Physical Review C*, 55(3):1420, 1997.

[49] Paul Sorensen. Elliptic flow: a study of space-momentum correlations in relativistic nuclear collisions. *Quark-Gluon Plasma 4. Edited by HWA RUDOLPH C & WANG XIN-NIAN. Published by World Scientific Publishing Co. Pte. Ltd., 2010. ISBN# 9789814293297, pp. 323-374*, pages 323–374, 2010.

[50] M.B. Tsang, W.G. Lynch, C.B. Chitwood, D.J. Fields, D.R. Klesch, C.K. Gelbke, G.R. Young, T.C. Awes, R.L. Ferguson, F.E. Obenshain, et al. Azimuthal correlations between light particles emitted in 12o induced reactions on 12c and 197au at 400 mev. *Physics Letters B*, 148(4-5):265–269, 1984.

[51] `https://www.hzdr.de/db/Cms?pNid=no&pOid=29675`, Aug 2017.

[52] G. Agakishiev, C. Agodi, H. Alvarez-Pol, E. Atkin, E. Badura, A. Balanda, A. Bassi, R. Bassini, G. Bellia, D. Belver, et al. The high-acceptance dielectron spectrometer hades. *The European Physical Journal A-Hadrons and Nuclei*, 41(2):243–277, 2009.

[53] D. Schüll, W. König, and U. Kopf. Specification of the HADES superconducting torus system. 1995.

[54] M. Lorenz. Geladene Kaonen Produktion in Ar+KCl Reaktionen bei 1.756 AGeV. Diploma thesis, Goethe-Universität Frankfurt, 2008.

[55] T. Scheib. Rekonstruktion des Hypertritons in Ar+KCl bei 1.76 AGeV mit HADES. Master thesis, Goethe-Universität Frankfurt, 2014. `https://www-hades.gsi.de/?q=node/126`.

[56] A. Schmah. *Produktion von Seltsamkeit in Ar+KCl Reaktionen bei 1.756 AGeV mit HADES*. PhD thesis, Technische-Universität Darmstadt, 2008. `https://www-hades.gsi.de/?q=node/126`.

[57] B. Kindler, B. Lommel, A. Hübner, W. Hartmann, J. Steiner, Hades Collaboration, et al. Targets for the electron–positron pair spectrometer hades. *Nuclear Instruments and Methods in Physics Research Section A: Accelerators, Spectrometers, Detectors and Associated Equipment*, 655(1):95–99, 2011.

[58] `https://www.gsi.de/forschungbeschleuniger/forschung_ein_ueberblick/hades_experiment/aufbau_des_hades_experiments.htm`, Aug 2017.

[59] J. Pietraszkoa, W. König, and S. Spataro. Beam detectors in Au+Au run and future developments. HADES Collaboration Meeting in Prague, Talk, 2013.

[60] P. Sellheim. Dielektronenrekonstruktion in Au+Au Kollisionen bei 1.236 AGeV mit HADES. Master thesis, Goethe-Universität Frankfurt, 2013. `https://www-hades.gsi.de/?q=node/126`.

[61] J. Pietraszko, L. Fabbietti, W. König, M. Weber, HADES Collaboration, et al. Diamonds as timing detectors for minimum-ionizing particles: The hades proton-beam monitor and start signal detectors for time of flight measurements. *Nuclear Instruments and Methods in Physics Research Section A: Accelerators, Spectrometers, Detectors and Associated Equipment*, 618(1):121–123, 2010.

[62] A. Rustamov. *New advances and developments on the RPC TOF wall of the HADES experiment at GSI*. PhD thesis, Technische-Universität Darmstadt, 2006.

[63] T. Bretz. Magnetfeldeigenschaften des spektrometers HADES. Diploma thesis, 2004.

[64] J. Markert. *Untersuchung zum Ansprechverhalten der Vieldraht-Driftkammern niedriger Massenbelegung des HADES Experimentes*. PhD thesis, Technische-Universität Darmstadt, 2005. `https://www-hades.gsi.de/?q=node/126`.

[65] J. Michel, M. Böhmer, M. Kajetanowicz, G. Korcyl, L. Maier, M. Palka, J. Stroth, A. Tarantola, M. Traxler, C. Ugur, et al. The upgraded hades trigger and data acquisition system. *Journal of Instrumentation*, 6(12):C12056, 2011.

[66] C. Agodi, A. Bassi, R. Bassini, G. Bellia, M. Benovic, C. Boiano, S. Brambilla, R. Coniglione, L. Cosentino, P. Finocchiaro, et al. The hades time-of-flight wall. *Nuclear Instruments and Methods in Physics Research Section A: Accelerators, Spectrometers, Detectors and Associated Equipment*, 492(1):14–25, 2002.

[67] `http://www.phys.ufl.edu/courses/phy4803L/group_I/muon/bicron_bc400-416.pdf`, Aug 2017.

[68] `https://www-hades.gsi.de/?q=node/14`, Aug 2017.

[69] `https://www-hades.gsi.de/node/65`, Aug 2017.

[70] G. Kornakov. *Exclusive η Meson Reconstruction in Proton-Proton Collisions at 2.2 GeV with the HADES Spectrometer and High Resolution Tracking*. PhD thesis, Universidade de Santiago de Compostela, 2012. `https://www-hades.gsi.de/?q=node/126`.

[71] D. Belver, A. Blanco, P. Cabanelas, N. Carolino, E. Castro, J. Diaz, P. Fonte, J.A. Garzón, D. Gonzalez-Diaz, A. Gil, et al. The hades rpc inner tof wall. *Nuclear Instruments and Methods in Physics Research Section A: Accelerators, Spectrometers, Detectors and Associated Equipment*, 602(3):687–690, 2009.

[72] `https://www-hades.gsi.de/?q=node/13`, Aug 2017.

[73] P. Cabanelas, M. Morales, J.A. Garzon, A. Gil, D. Gonzalez-Diaz, A. Blanco, D. Belver, E. Casarejos, P. Fonte, W König, et al. Performances of 4-gap timing rpcs for relativistic ions in the range z= 1–6. *Journal of Instrumentation*, 4(11):P11007, 2009.

[74] HADES internal reports, Aug 2017.

[75] `https://www-hades.gsi.de/?q=node/15`, Aug 2017.

[76] A. Tarantola, I. Fröhlich, B.W. Kolb, J. Michel, C. Müntz, M. Palka, H. Ströbele, J. Stroth, M. Traxler, and J Wüstenfeld. The upgrade of the multiwire drift chamber readout of the hades experiment at gsi. In *Nuclear Science Symposium Conference Record, 2008. NSS'08. IEEE*, pages 2146–2149. IEEE, 2008.

[77] A. Rustamov. *Exclusive η Meson Reconstruction in Proton-Proton Collisions at 2.2 GeV with the HADES Spectrometer and High Resolution Tracking*. PhD thesis, Technische Universität, 2006.

[78] H. Schuldes. *Charged Kaon and ϕ reconstruction in Au+Au collisions at 1.23 AGeV*. PhD thesis, Goethe-Universität Frankfurt, 2016. `https://www-hades.gsi.de/?q=node/126`.

[79] `https://www-hades.gsi.de/?q=computing`, Aug 2014.

[80] M. Alvioli, H.J. Drescher, and M. Strikman. A monte carlo generator of nucleon configurations in complex nuclei including nucleon–nucleon correlations. *Physics Letters B*, 680 (3):225–230, 2009.

[81] B. Kardan. Centrality determination at 1.23 AGeV Gold-Gold collisionsand readout- electronics for the HADES electromagnetic calorimeter. Diploma thesis, Goethe-Universität Frankfurt, 2015.

[82] K.A. Olive, Particle Data Group, et al. Review of particle physics. *Chinese physics C*, 38 (9):090001, 2014.

[83] F. Sauli. Principles of operation of Multiwire Proportional and Drift Chamber, 1977.

[84] J. Beringer et al. *Particle Physics Booklet*. APS physics CERN, 2012.

[85] G. Kornakov. private communictaion, 2017.

[86] P. Tlusty and M. Gumberidze. `https://indico.gsi.de/getFile.py/acces?contribId=1&resId=0&materialId=slides&confId=5389`, Aug 2017.

[87] C. Adler, Z. Ahammed, C. Allgower, J. Amonett, B.D. Anderson, M. Anderson, G.S. Averichev, J. Balewski, O. Barannikova, L.S. Barnby, et al. Elliptic flow from two-and four-particle correlations in au+ au collisions at s nn= 130 gev. *Physical Review C*, 66(3): 034904, 2002.

[88] Jean-Yves Ollitrault. Reconstructing azimuthal distributions in nucleus-nucleus collisions. *arXiv preprint nucl-ex/9711003*, 1997.

[89] Jean-Yves Ollitrault, Arthur M Poskanzer, and Sergei A Voloshin. Effect of flow fluctuations and nonflow on elliptic flow methods. *Physical Review C*, 80(1):014904, 2009.

[90] P. Shanmuganathan, STAR Collaboration, et al. Beam-energy and centrality dependence of directed flow of identified particles. *Nuclear Physics A*, 956:260–263, 2016.

[91] A.M. Poskanzer, S.A. Voloshin, J. Bächler, D. Barna, L.S. Barnby, J. Bartke, R.A. Barton, L. Betev, H. Białkowska, A. Billmeier, et al. Centrality dependence of directed and elliptic flow at the SPS. *Nuclear Physics A*, 661(1-4):341–344, 1999.

[92] W. Reisdorf, Y. Leifels, A. Andronic, R. Averbeck, V. Barret, Z. Basrak, N. Bastid, M.L. Benabderrahmane, R. Čaplar, P. Crochet, et al. Systematics of azimuthal asymmetries in heavy ion collisions in the 1a gev regime. *Nuclear Physics A*, 876:1–60, 2012.

[93] A. Andronic, G. Stoicea, M. Petrovici, V. Simion, P. Crochet, J.P. Alard, R. Averbeck, V. Barret, Z. Basrak, N. Bastid, et al. Transition from in-plane to out-of-plane azimuthal enhancement in au+ au collisions. *Nuclear Physics A*, 679(3-4):765–792, 2001.

[94] I. Selyuzhenkov and Sergei A. Voloshin. Effects of nonuniform acceptance in anisotropic flow measurements. *Physical Review C*, 77(3):034904, 2008.

[95] Y. Zhou. *Anisotropic Flow and flow fluctuations at the Large Hadron Collider*. Utrecht University, 2016.

[96] A. Bilandžić, R. Snellings, and S. Voloshin. Flow analysis with cumulants: Direct calculations. *Physical Review C*, 83(4):044913, 2011.

[97] N. Borghini, P.M. Dinh, and J.-Y. Ollitrault. Flow analysis from multiparticle azimuthal correlations. *Physical Review C*, 64(5):054901, 2001.

[98] R. S. Bhalerao, N. Borghini, and J.-Y. Ollitrault. Genuine collective flow from Lee–Yang zeroes. *Physics Letters B*, 580(3):157–162, 2004.

[99] R. S. Bhalerao, N. Borghini, and J.-Y. Ollitrault. Analysis of anisotropic flow with Lee–Yang zeroes. *Nuclear Physics A*, 727(3-4):373–426, 2003.

Eidesstattliche Erklärung

Ich versichere hiermit, dass ich die vorliegende Arbeit selbständig verfasst, keine anderen als die angegebenen Hilfsmittel verwendet und sämtliche Stellen, die benutzten Werken im Wortlaut oder dem Sinne nach entnommen sind, mit Quellen- beziehungsweise Herkunftsangaben kenntlich gemacht habe.

Frankfurt am Main, den September 24, 2017

Mathilde Himmelreich

Danksagung

Bei Professor Christoph Blume möchte ich mich an erster Stelle bedanken, dass er mir diese interessante Masterarbeit ermöglichte und ich Teil seiner Arbeitgruppe werden konnte, obwohl ich meine Bachelorarbeit in einem anderen Institut geschrieben habe. Er und Professor Joachim Stroth haben mich entscheidend beeinflusst, mein Fach zu wechseln, von der Chemie in die Physik. Dafür bin ich sehr dankbar, denn so konnte ich viele wirklich nette, interessante und interessierte Menschen kennen lernen. In Erinnerung bleiben wird mir insbesonders Professor Blumes besonnene und freundliche Art.

Behruz Kardan möchte ich danken, dass er als frisch gebackener Papa immer noch Zeit fand, mit mir anregende Diskussionen zu führen und meine Texte gründlich auseinander zu nehmen.

Doktor Heidi Schuldes möchte ich für ihr stets gut gelauntes Wesen danken und für die sehr förderliche inhaltliche Kritik. Von ihr habe ich viel lernen können und freue mich sehr, dass sie Christophs Postdoc geworden ist: Team Flower-Power! ❀

Insgesamt möchte ich allen Mitgliedern der HADES-Gruppe danken, für die nette Zusammenarbeit, Diskussionen und vielen Anregungen und natürlich für die Freundschaft (M und M und M). Es hat einfach viel Spaß gemacht!

Insbesondere danken möchte ich auch Jochen Markert, denn neben seiner eigentlichen Tätigkeit findet er wirklich immer Zeit bei allen möglichen Fragestellungen zu helfen. Der Austausch mit Malgorzata Gumberidze, Georgy Kornakov und Szymon Harabasz hat mich ebenfalls sehr bereichert und ich bin froh, so interessante Gesprächspartner an der GSI getroffen zu haben. Nicht zu vergessen: Vielen Dank an Markus Mayer für die Donnerstage als auch für die Nachtschicht! Zu zweit macht es einfach mehr Spaß!

Dem organisatorischen Herzstück des IKFs, Marianne Frey, gilt mein besonderer und herzlicher Dank: ohne sie wäre mein Studium sehr wahrscheinlich etwas anders verlaufen. Denn sie denkt um Jahre voraus, fertigt Kopien von Dingen an, die man (frau) vielleicht später nochmal gebrauchen kann. Tausend Dank an dieser Stelle!

Meiner Familie möchte für *Forelle im Jackett* und für ihre Unterstützung meines Studiums danken und ich hoffe sehr, dass mich alle vier noch lange in meinem Leben begleiten werden: Henriette und Martin, Christoph und Anja.

Und Richard, der seit mehr als drei Jahren alle Höhen und Tiefen mit mir teilen mag :).

Men do not stumble over mountains,
but over mole hills.
– Confucius –